Copyright
by
Nicholas John Joseph
2013

The Thesis committee for Nicholas John Joseph

Certifies that this is the approved version of the following thesis:

A Comparison of Models for a Piezoelectric 31-Mode Segmented Cylindrical Transducer

APPROVED BY

SUPERVISING COMMITTEE:

Preston S. Wilson, Supervisor

Michael R. Haberman, Co-supervisor

A Comparison of Models for a Piezoelectric 31-Mode Segmented Cylindrical Transducer

by

Nicholas John Joseph, BA Physics

THESIS

Presented to the Faculty of the Graduate School of

The University of Texas at Austin

in Partial Fulfillment

of the Requirements

for the Degree of

Master of Science in Engineering

THE UNIVERSITY OF TEXAS AT AUSTIN

December 2013

To my family.

Acknowledgments

I would like to humbly thank everyone who has supported me during my graduate studies, without whom this thesis would not be possible. In particular, I would like to thank Dr. Michael R. Haberman for taking me on as a graduate research assistant and for providing me with invaluable insight, guidance, and encouragement during the research process and the writing of this thesis. I would also like to thank Dr. Preston S. Wilson for reviewing this thesis and providing helpful comments and feedback. I also want to thank Dr. Mark F. Hamilton for the foundational knowledge that he has imparted to me as a professor and the guidance that he has provided as an academic advisor. Additionally, I want to express my gratitude to the Office of Naval Research, Code 32 for supporting the research work done for this thesis.

I would also like to thank The University of Texas at Austin Cockrell School of Engineering for accepting me as a graduate student and providing me with an excellent graduate education. The *Sam Y. Zamrik Endowed Graduate Fellowship in Engineering* has been extremely helpful in making it possible for me to take advantage of this opportunity and I would like to thank Sam Y. Zamrik for his support. I would also like to thank my fellow graduate students and friends including Kyle Spratt, Ben Copenhaver, Mustafa Abbasi, Matt Guild, Scott Schoen, Tim Klatt, Bryant Tran, Craig Dolder, Caleb Sieck

and Dan Tengelsen for many hours of fruitful conversation both inside and outside of the lab. Finally, I want to thank friends and family outside of the UT community who have supported me and helped me to remain grounded during my time as a graduate student.

NICHOLAS JOHN JOSEPH

The University of Texas at Austin

August 2013

A Comparison of Models for a Piezoelectric 31-Mode Segmented Cylindrical Transducer

Nicholas John Joseph, MSE
The University of Texas at Austin, 2013

Supervisors: Preston S. Wilson
Michael R. Haberman

Piezoelectric transducers with cylindrical geometry are often designed to operate in a radial breathing mode. In order to tune their performance in a cost effective way, cylinders can be constructed of alternating active (piezoelectric) and inactive (non-piezoelectric) staves. Existing lumped parameter models for such a ring are based on effective piezoelectric properties of the composite ring which reduce the system to a single degree of freedom corresponding to the breathing motion. Unfortunately, if the length of the staves is a sufficiently large percentage of the circumference, the transducer may demonstrate a detrimental higher frequency resonance within the desired bandwidth of operation even when all staves are uniformly excited by an electrical field. This parasitic resonance results from bending motion of the staves associated with stiffness and mass discontinuities of the constituent material properties and can significantly decrease the radiated acoustic pressure and generate distortion of the radiated acoustic waveform. This work presents a

multiple-degree-of-freedom lumped parameter model that captures both the breathing and bending resonances of the transducer and provides a more accurate prediction of its effective coupling coefficient. Results are compared with a one-degree-of-freedom model, finite element models, and experimental data. Modifications to account for internal volumes, nonlinearities, and other effects are also presented and discussed.

Table of Contents

Chapter 1

Introduction

1.1 Motivation

The performance of a piezoelectric transducer can be evaluated on its transduction sensitivity, resonance frequencies, and the efficiency at which it converts energy from one domain to another. In designing a transducer, material properties and dimensions are chosen to optimize these criteria for its intended purpose. Since the construction of a working transducer can be time-intensive and costly, mathematical models are sought to capture key aspects of the transducer's performance without having to physically build it. Two types of models are commonly used: (*i*) lumped parameter models, typically presented in equivalent circuit form for linking to the electrical domain, and (*ii*) finite element models, where a high-resolution three-dimensional representation of the transducer is possible. Finite element method simulations often require significant time and computational power and thus are difficult to use as a primary design tool. The lumped parameter models, by contrast, are relatively simple, typically having one degree of freedom representing the intended mode of the transducer. The cost of such simplicity is that a number of approximations are made in the creation of the model that can make it an inaccurate or incomplete representation of the transducer.

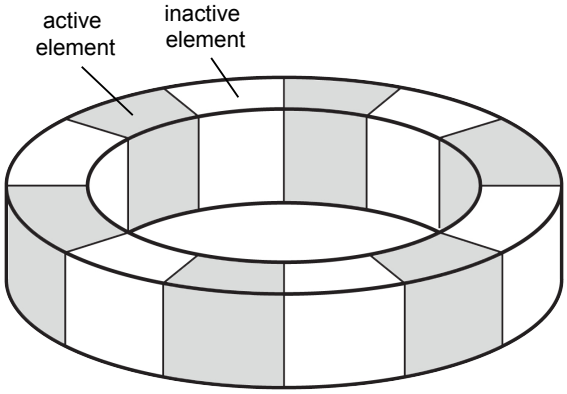

Figure 1.1: Segmented ring piezoelectric transducer with alternating active and inactive element staves.

This thesis examines various models for a segmented ring piezoelectric transducer composed of alternating active and inactive element staves, similar to that shown in Fig. 1.1. One model is a lumped parameter representation with a single degree of freedom, designed to capture only the primary breathing mode of the transducer at which it is intended to operate. The breathing mode is shown schematically in Fig. 1.2(a). Because the active elements in the ring are identically electroded with the same voltage (magnitude and phase) excitation, the ring is restricted to vibrate only in symmetric modes like the breathing mode that can be represented in a slice of the ring consisting of half of an adjacent active and inactive element pair. One other such mode, at the upper end of the operating frequency band, appears in finite element models of the transducer. This mode results from bending effects in the element staves and is shown in Fig. 1.2(b). The normalized[1] input electrical admittance of the

[1]See Appendix A for a description of the normalization scheme.

transducer as given by the one-degree-of-freedom model ("Model 1") and the finite element model ("FEM") is shown in Fig. 1.3. The breathing mode resonance appears as a peak in the admittance of both models around $f/f_0 = 1$. The bending resonance is necessarily absent from the one-degree-of-freedom model but readily apparent in the finite element model near $f/f_0 = 5$. Additionally, the difference in the frequency of anti-resonance and the overall level of the admittance magnitude at higher frequencies suggests further discrepancies between the models. The bending resonance is considered parasitic

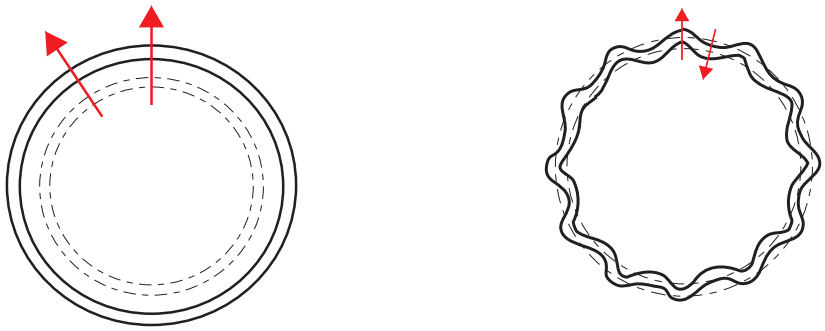

(a) Breathing mode of ring.

(b) Bending mode of ring.

Figure 1.2: Relevant modes for segmented transducer ring. Dotted lines indicate equilibrium position of ring. Red arrows indicate relative displacement from equilibrium of adjacent areas of ring in each mode.

because it corresponds to a mode in which a flexural wave occurs along the perimeter of the ring, causing the transducer to radiate sound less effectively. A multi-degree-of-freedom model was sought to capture this mode because it is found to have a significant effect on the performance of the transducer. The model may be used as a design tool to push the parasitic resonance out of the

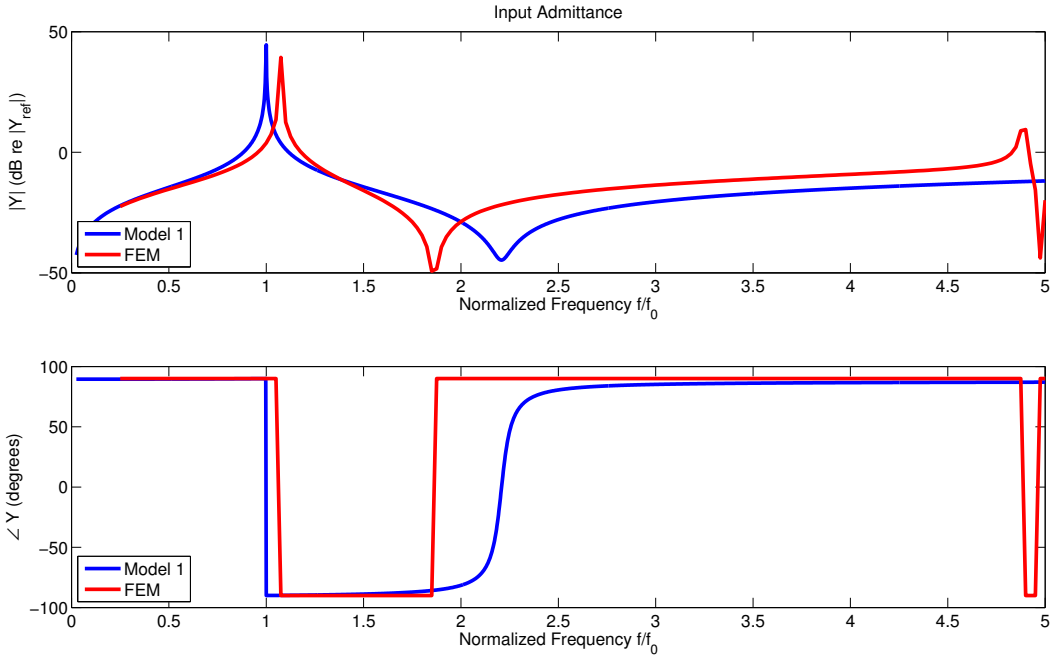

Figure 1.3: Comparison of the input electrical admittance of transducer (in air) as given by a finite element method COMSOL model, compared with results of the one-degree-of-freedom Model 1.

desired operating band or to determine if such a resonance will occur for a given geometry and set of material parameters.

1.2 Previous Work

Piezoelectric ring transducers operating in a radial expansion mode are commonly used in underwater sound applications and have previously been the subject of analysis. The modes of thin-walled, isotropic cylindrical tubes were determined by Love [1]. This analysis was later expanded upon by Haskins and Walsh to determine the mechanical resonance frequencies and electrical

admittance of anisotropic cylindrical tubes of radially polarized piezoelectric ceramic [2]. Following this, Berlincourt made a number of simplifying assumptions to develop an equivalent circuit for a piezoelectric ring operating in 31-mode [3]. Greater mechanical coupling is possible through a ring operating with poled direction along the ring's circumference, though the ring must then be broken into segments to allow for the placement of electrodes. A model for an all-piezoelectric segmented ring was presented by Camp [4] and later modified by Butler to allow for inactive segments [5]. Much of the basis for the lumped parameter piezoelectric transducer modeling done here is adapted from Wilson [6] and Sherman and Butler [7]. In their work, these authors use the constitutive equations of the piezoelectric material and the geometries of various transducers to develop one-degree-of-freedom models. Chapter 3 adapts some of this work, along with the segmented ring model given by Butler, to produce a one-degree-of-freedom model for the segmented ring transducer being considered here.

1.3 Objectives

The principal objective of this thesis is the development of a multi-degree-of-freedom lumped element model for a segmented ring transducer that captures the bending mode of the ring and more accurately represent its performance in general. This model is to be extended to allow for various effects related to the conditions encountered in the construction and deployment of the built transducer. Additionally, a comparison of results with earlier models

and experimental data from a built transducer is presented.

1.4 Approach

This thesis begins with a brief summary of piezoelectric theory in **Chapter 2**, in which key mechanisms of piezoelectric material and the constitutive equations governing its behavior are discussed. Piezocrystal elements are compared with piezoceramics regarding their fine structure and design advantages. Additionally, a brief discussion of transducer theory is presented and relevant performance criteria are defined and discussed. **Chapter 3** presents a one-degree-freedom model of the segmented ring transducer with modifications and gives performance criteria results for various cases. **Chapter 4** presents finite element models (both a custom-made model and one made using the COMSOL Multiphysics package) and compares them to the one-degree-of-freedom model. The discrepancies between the two types of models, particularly around the parasitic bending resonance, motivates the development of a multi-degree-of-freedom lumped element model that is more consistent with the finite element models. This development is presented in **Chapter 5**, where the ring transducer system is represented using mechanical models, equivalent circuits, and bond graphs. The results of all models are compared with experimental data in **Chapter 6**. The thesis concludes in **Chapter 7** with a summary of goals achieved and recommendation of future work to be conducted.

Chapter 2

Piezoelectric Transducer Theory

A basic understanding of piezoelectric materials and transducer theory is necessary to the understanding of the performance of a piezoelectric transducer. This chapter therefore provides concise summary of both the fundamental physical behavior associated with piezolectric materials and basic transduction theory. Section 2.1 discusses the piezoelectric effect and compares piezoceramics with piezocrystals. This is followed by a development of constitutive equations for piezoelectric material in Section 2.2. A brief discussion of transducer theory as it relates to piezoelectric transducers is presented in Section 2.3. Finally, relevant metrics and performance criteria for piezoelectric transducers are discussed in Section 2.4.

2.1 Piezoelectric Materials

Certain crystalline materials become electrically charged when subject to an applied stress, and conversely undergo an elastic strain when exposed to an applied electric field. These effects are referred to as the piezoelectric and inverse piezoelectric effect, respectively, and such materials are labeled piezoelectric [8]. Piezoelectric materials allow energy to be transduced from

the electrical to the mechanical domain, and vice versa.

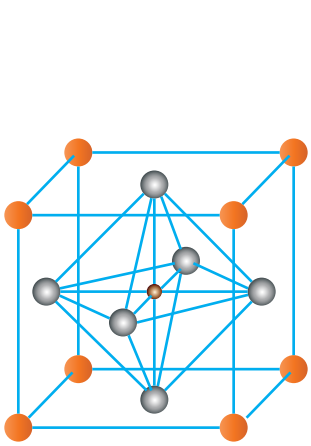

(a) Symmetrical crystal structure above Curie temperature.

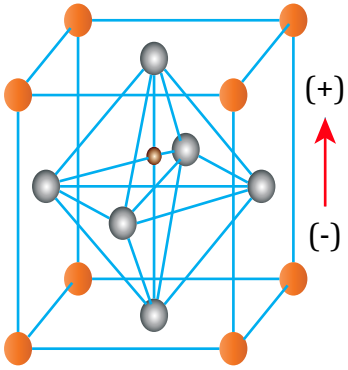

(b) Asymmetrical crystal structure below Curie temperature. Plus and minus signs indicate region of positive and negative charge, respectively. Red arrow indicates direction of dipole.

Figure 2.1: Crystal structure of piezoelectric ceramic, adapted from APC International [8].

Since the 1960s, piezoelectric ceramics have been made that surpass many of the properties of naturally occurring piezoelectric quartz minerals. These ceramics can be formed into an arbitrary geometry and are made by heating a mixture of metallic oxide powder and binding material. The metallic oxides form crystals that, above a critical temperature know as the Curie point, exhibit symmetry with respect to positive and negative charge arrangement, as shown in Fig. 2.1(a). Below the Curie temperature, the crystal structure becomes asymmetrical and therefore carries a dipole moment, as shown in Fig. 2.1(b). Within a piezoceramic, these crystals form crystallite structures called grains, each of which, below the Curie temperature, contain ferroelec-

tric domains with a net dipole moment [8]. However, because these domains are randomly oriented, the total ceramic has no polarization. The ceramic becomes polarized by exposing it to a strong DC electric field at a temperature just below the Curie temperature. This lengthens the dipole domains within each grain that are nearly aligned with the electric field at the expense of those that are not. The lengthened dipole domains remain so when the field is removed, giving the material a permanent polarization as well as a permanent elongation [8]. Figure 2.2(a) depicts the alignment of ferroelectric domains in a piezoceramic material before and after poling. Piezoceramics are typically very robust materials with properties that remain stable under a wide range of physical, electrical and thermal conditions. Additionally, the randomly aligned grain boundaries provide resistance to cracking and crack propagation [8].

More recently, significantly large man-made piezoelectric elements have been developed that are composed of a single crystal rather than a ceramic mixture of crystal and binding material [9]. The uniform structure of these piezocrystals causes them to have identically oriented grains. Once poled with an electric field, almost all of the dipole domains align. Figure 2.2(b) depicts the alignment of domains in a piezocrystal material before and after poling. Note the near uniform alignment in the piezocrystal in comparison with that of the piezoceramic. Because of this, the piezoelectric coupling properties of such elements are greater than their ceramic counterparts. Specifically, piezocrystals have exhibited much higher values for the piezoelectric strain

constant and electromechanical coupling coefficient (defined in Sections 2.2 through 2.4) than piezoceramics [9]. Additionally, the properties of piezocrystals can be easier to tune (by changing crystal phase, orientation, or symmetry) than those of piezoceramics. For example, the direction in which a raw single crystal elements is cut will alter its performance and can be done to maximize its thickness or shear deformation for different applications [8].

Though single crystal piezoelectrics offer many advantages over piezoceramics, they do present some challenges as well. They have a relatively low Curie temperature and ferroelectric phase transition temperature [9], making their properties unstable under certain conditions. Additionally, current fabrication techniques are costly and limit the size of homogenous crystals [9].

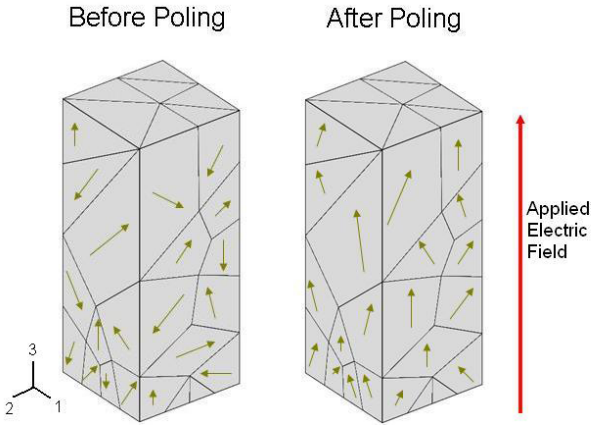

(a) Piezoceramic.

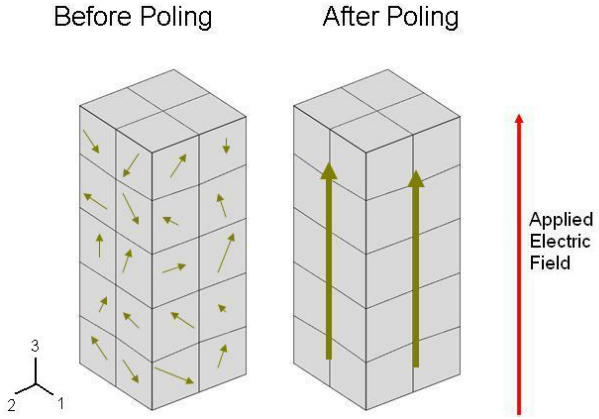

(b) Piezocrystal.

Figure 2.2: Ferroelectric domains before and after polarization for (a) piezoceramics and (b) piezocrystals. From Nguyen citekN10.

2.2 Piezoelectric Effects

The most general characterization of the behavior of a material that couples excitations in electromagnetic domain to mechanical deformation (and vice versa) is well-described by the following quantities: internal energy U, strain and stress S and T, electric field and electric displacement E and D,

magnetic induction and magnetic field strength H and B, and entropy and temperature σ and θ. Wilson relates all of these quantities through the Gibbs free energy G of the system and derives a relatively simple set of coupled equations approximating the response of piezoelectric materials to a field of interest [6]. The Gibbs free energy is a measure of the maximum energy obtainable from a closed system and is given by:

$$G = U - S_j T_j - E_n D_n - H_n B_n - \sigma\theta, \tag{2.1}$$

where the repeated index represents a summation, and the values of j and n range from 1 to 6 and 1 to 3 respectively. The first and second laws of thermodynamics may be used to write the differential of Eq. (2.2) as

$$dG = -S_j dT_j - D_n dE_n - H_n dB_n - \sigma d\theta. \tag{2.2}$$

In order to simplify these relations, the work presented here assumes that both the magnetic field and the temperature of the material remain constant. These are reasonable assumptions for a piezoelectric material driven at a low duty cycle. Invoking these assumptions, the magnetic field and temperature differentials go to zero and Eq. (2.2) becomes

$$dG = -S_j dT_j - D_n dE_n. \tag{2.3}$$

The strain and electric field may then be related to derivatives of the Gibbs function as follows:

$$S_i = -\left.\frac{\partial G}{\partial T_i}\right|_E \tag{2.4}$$

and

$$D_m = -\left.\frac{\partial G}{\partial E_m}\right|_T, \tag{2.5}$$

where the values of i and m range from 1 to 6 and 1 to 3 respectively. It can be seen from Eqs (2.4) and (2.5) that the strain S and electric displacement D are both functions of the stress T and electric field E. The total differentials for strain and electric displacement can be written as

$$dS_i = \left.\frac{\partial S_i}{\partial T_j}\right|_E dT_j + \left.\frac{\partial S_i}{\partial E_n}\right|_T dE_n \tag{2.6}$$

and

$$dD_m = \left.\frac{\partial D_m}{\partial T_j}\right|_E dT_j + \left.\frac{\partial D_m}{\partial E_n}\right|_T dE_n \tag{2.7}$$

respectively. As dG is a perfect differential, the partial derivatives in Eqs. (2.6) and (2.7) can be defined as constants of the material. Using superscripts to indicate the value of a coefficient when the superscript quantity is held constant, the material constants can be defined as follows:

- The short-circuit elastic compliance constant is the change in strain due to an applied mechanical stress with electric field held constant:

$$s_{ij}^E = \left.\frac{\partial S_i}{\partial T_j}\right|_E. \tag{2.8}$$

- The stress-free dielectric permittivity constant is the change in electric displacement due to an applied electric field with stress held constant:

$$\epsilon_{mn}^T = \left.\frac{\partial D_m}{\partial E_n}\right|_T \tag{2.9}$$

- The piezoelectric strain constant is the change in electric displacement due to an applied mechanical stress at constant electric field, or the change in strain due to an applied electric field at constant stress:

$$d_{mi} = \left.\frac{\partial D_m}{\partial T_i}\right|_E = \left.\frac{\partial S_i}{\partial E_m}\right|_T . \tag{2.10}$$

Choosing the equilibrium values of the field variables as zero and assuming only small deviations, Eqs. (2.6) and (2.7) may be integrated to yield the strain-charge form of the piezoelectric constitutive equations:

$$S_i = s_{ij}^E T_j + d_{ni}^E E_n \tag{2.11}$$

and

$$D_m = d_{mj}^E T_j + \epsilon_{mn}^T E_n. \tag{2.12}$$

These may be written in matrix form as

$$\mathbf{S} = \mathbf{s}^E \cdot \mathbf{T} + \mathbf{d}^{\mathrm{T}} \cdot \mathbf{E} \tag{2.13}$$

and

$$\mathbf{D} = \mathbf{d} \cdot \mathbf{T} + \epsilon^T \cdot \mathbf{E}, \tag{2.14}$$

where Voigt notation[1] is employed to write $\mathbf{S}$, $\mathbf{T}$, $\mathbf{D}$ and $\mathbf{E}$ as vectors representing the strain, stress, electric displacement, and electric field respectively. The material constants in these relationships are the elastic compliance at

[1]Voigt notation exploits the symmetry of the matrices to collapse multidimensional tensors into 1-dimensional vectors. For example, the 3×3 strain tensor becomes the 6×1 strain vector $\mathbf{S}$. See Wilson [6], Chapter 3 for a detailed explanation.

constant electric field, $\mathbf{s}^E$, a 6×6 matrix, the piezoelectric strain constant, $\mathbf{d}$, a 6×3 matrix, and the dielectric constant at constant applied stress, ϵ^T, a 3×3 matrix. '$\cdot$' denotes the inner product, and $\mathbf{d}^{\mathrm{T}}$ indicates the transpose of matrix $\mathbf{d}$. Most piezoelectric transducer devices make use of geometries that allow the matrix equations given in Eqs. (2.13) and 2.14 to be approximated as one-dimensional equations.

Equations (2.13) and (2.14) indicate that piezoelectric materials are anisotropic, that is, the material constants describing their mechanical and electrical properties are directionally dependent. By convention the directions are related to a rectangular x-y-z coordinate system with the positive z axis taken to be the direction in which the material is polarized. The the piezoelectric material constants carry two subscripts that reference the x,y, and z axes with the numbers 1, 2, and 3 respectively. The first subscript represents the direction of the applied (electrical or mechanical) field and the second the direction of the resulting reaction.

2.3 Piezoelectric Transducers

A transducer is any device which converts energy from one domain to another. An electromechanical transducer converts electrical energy into mechanical energy and/or vice versa. Piezoelectric transducers use piezoelectric materials as a means of electromechanical transduction.

The piezoelectric transducer presented in this thesis can be modeled as a two-port, four-terminal network like that shown in Fig. 2.3. This network re-

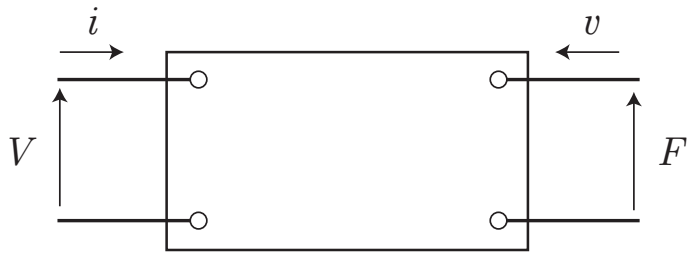

Figure 2.3: Two-port network model of transducer, adapted from Kinsler and Frey [10].

lates the voltage V and current i at the electrical terminals to their analogues, force F and velocity v respectively, at the mechanical terminals. The coupling between the electrical and mechanical domains is characterized by two transduction coefficients T_{em} and T_{me} (electrical to mechanical and mechanical to electrical, respectively) that describe the effect that inputs from one domain have on another. Conditions may be imposed on the system in order to isolate the electrical and mechanical effects and facilitate the writing of constitutive equations. In particular, the blocked electrical impedance Z_{EB} is defined as the voltage to current ratio when the transducer is mechanically blocked such that the velocity $v = 0$. Likewise, the open-circuit mechanical impedance Z_{mo} is the force to velocity ratio when the transducer is in an open circuit ($i = 0$) condition. Using these definitions, Kinsler and Frey [10] give the canonical pair of equations relating the mechanical and electrical quantities as:

$$V = Z_{\mathrm{EB}} i + T_{\mathrm{em}} v \tag{2.15}$$

and

$$F = T_{\text{me}} i + Z_{\text{mo}} v \tag{2.16}$$

Canonical equations may also be written in terms of the free ($F = 0$) electrical impedance Z_{EF} and the short-circuit ($V = 0$) mechanical impedance Z_{ms}. Z_{EF} may be found by setting $F = 0$ in Eq 2.16, solving for v in terms of i, substituting the result in Eq. (2.15), and solving for the impedance ratio V/i. This yields

$$Z_{\text{EF}} = \left(1 - \frac{T_{\text{em}} T_{\text{me}}}{Z_{\text{EB}} Z_{\text{mo}}}\right) Z_{\text{EB}}. \tag{2.17}$$

Z_{ms} may be found by setting $V = 0$ in Eq. (2.15) and performing similar manipulations, resulting in

$$Z_{\text{ms}} = \left(1 - \frac{T_{\text{em}} T_{\text{me}}}{Z_{\text{EB}} Z_{\text{mo}}}\right) Z_{\text{mo}}. \tag{2.18}$$

The factor $T_{\text{em}} T_{\text{me}} / (Z_{\text{EB}} Z_{\text{mo}})$ appearing in both Eqs. (2.17) and (2.18) is a measure of how much energy is transduced from one domain to another and is the square of the piezoelectric coupling coefficient k:

$$k^2 = \frac{T_{\text{em}} T_{\text{me}}}{Z_{\text{EB}} Z_{\text{mo}}}. \tag{2.19}$$

The coupling coefficient will be discussed in greater detail in Section 2.4.1.

Piezoelectric transducers obey the reciprocity principal, that is, the ratio of response to excitation is invariant when their positions are interchanged in the network. In this case the matrix of coefficients relating the electrical and mechanical variables are symmetric and the two transduction coefficients are identical, that is, $T_{\text{em}} = T_{\text{me}} = T$. The two-port network may then be

represented by the equivalent circuits shown in Fig. 2.4, where the electrical and mechanical domains are linked by a transformer with ideal turns ratio $\phi = T/Z_E$.

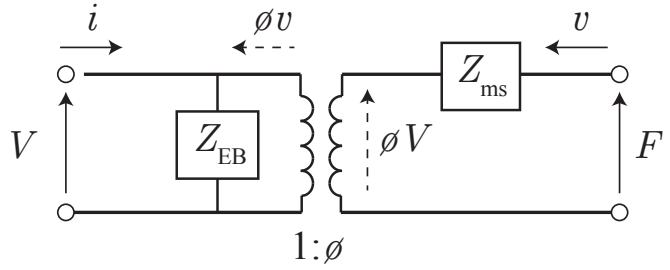

(a) Equivalent circuit with transformer.

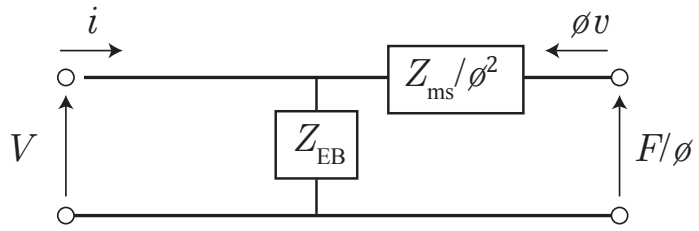

(b) Equivalent circuit with transformer removed.

Figure 2.4: Equivalent circuits for reciprocal transducer, adapted from Kinsler and Frey [10].

The values of the parameters Z_{ms}, Z_{EB}, and ϕ in the equivalent circuit are given by the properties of the piezoelectric material. They may be determined by arranging the constitutive piezoelectric equations (Eqs. (2.13) and (2.14)) in the same form as the two-port transducer equations. A version of this process performed in Section 3.1 where a circuit model, similar to that shown in Fig. 2.4, is developed for a 31-mode piezoelectric ring transducer.

2.4 Relevant Metrics

The response of a piezoelectric transducer at various excitation frequencies can be quantified with metrics that, taken together, provide a complete description of the transducer performance. This thesis makes extensive use of the electromechanical coupling coefficient, input electrical admittance, radial velocity, transmit voltage response, and total harmonic distortion as metrics of performance for a 31-mode piezoelectric cylinder. The following sections provides a concise summary of each.

2.4.1 Electromechanical Coupling Coefficient

The piezoelectric coupling coefficient k mentioned in the previous section is a measure of how much electrical energy is converted to mechanical energy, or vice versa, by a piezoelectric transducer. In this sense it is an indication of the electromechanical efficiency of the transducer. If the transducer receives energy from only one of its ports, the electromechanical coupling coefficient can be defined in squared form as [6]

$$k^2 = \frac{\text{energy transduced}}{\text{total energy input}}. \tag{2.20}$$

For piezoelectric materials of different design and geometries, this value k is subscripted according to piezoelectric convention, where the first subscript indicates the direction along which the electrodes are applied, and the second subscript indicates direction normal to the active mechanical face of interest.

Wilson [6] gives a general definition the piezoelectric coupling factor

as the ratio of the mutual elastic and dielectric energy density, U_{Mut}, to the geometric mean of the elastic strain energy density, U_{Elas}, and the dielectric energy density, U_{Diel},:

$$k = \frac{U_{\mathrm{Mut}}}{\sqrt{U_{\mathrm{Elas}} U_{\mathrm{Diel}}}}. \tag{2.21}$$

For a linear piezoelectric system under quasi-static conditions, the total energy density can be written as

$$U = \frac{S_{\mathrm{i}} T_{\mathrm{i}}}{2} + \frac{D_{\mathrm{m}} E_{\mathrm{m}}}{2}. \tag{2.22}$$

For the 31-mode ring transducer discussed in this document, the total energy density, using the canonical Equations (3.1) and (3.2) from Section 3.1, is

$$U = \frac{T_1^2 s_{11}^E}{2} + T_1 d_{31} E_3 + \frac{E_3^2 \epsilon_{11}^T}{2}. \tag{2.23}$$

From Eq. (2.23) one may identify

$$U_{\mathrm{Elas}} = \frac{T_1^2 s_{11}^E}{2} \tag{2.24}$$

$$U_{\mathrm{Mut}} = \frac{T_1 d_{31} E_3}{2} \tag{2.25}$$

and

$$U_{\mathrm{Diel}} = \frac{E_3^2 \epsilon_{33}^T}{2}. \tag{2.26}$$

Substituting Eqs. (2.24) through (2.26) into Eq. (2.21) and squaring we obtain

$$k_{31}^2 = \frac{d_{31}^2}{s_{11}^E \epsilon_{33}^T}. \tag{2.27}$$

Under certain conditions, the coupling coefficient can also be written in terms of the (series) resonance frequency, f_{s}, and anti-resonance (or parallel resonance) frequency, f_{p}, of the transducer system. The piezoelectric

transducer shown in Fig. 2.4 can be idealized by approximating the blocked electrical impedance as that of a pure capacitor C_0 and the short-circuit mechanical impedance as that of a mechanical compliance C and mass M. These mechanical elements can be related to the electrical domain through appropriate multiplication by the turns ratio ϕ. The equivalent circuit of such a transducer is shown in Fig. 2.5. At low frequencies, the inductive reactance due to mass M is relatively small, and the electrical network effectively consists of capacitors C_0 and C/ϕ^2 in parallel. In this case, for an applied alternating voltage V, the total energy input is given by $(C_0 + \phi^2 C)V^2/2$ and the energy transduced given by $\phi^2 C V^2/2$. Using Eq. (2.20), the electromechanical coupling coefficient is given by

$$k^2 = \frac{\phi^2 C}{C_0 + \phi^2 C}, \tag{2.28}$$

which is consistent with Eq. (2.19) given these conditions. The motional resonance frequency f_s occurs when M resonates with C and is given by

$$f_\mathrm{s}^2 = \frac{1}{(2\pi)^2}\frac{1}{MC}. \tag{2.29}$$

Likewise, the motional anti-resonance frequency occurs when M resonates with C in series with C_0 and is given by

$$f_\mathrm{p}^2 = \frac{1}{(2\pi)^2}\frac{\phi^2 C + C_0}{MCC_0}. \tag{2.30}$$

Dividing Eqs. (2.29) and (2.30) gives

$$\frac{f_\mathrm{s}^2}{f_\mathrm{p}^2} = \frac{C_0}{\phi^2 C + C_0} = 1 - k^2, \tag{2.31}$$

with k^2 given by Eq. (2.28). Rearranging Eq.(2.31) yields [11]

$$k^2 = 1 - \frac{f_{\mathrm{s}}^2}{f_{\mathrm{p}}^2}. \tag{2.32}$$

A higher frequency anti-resonance is thus an indication of a more efficient transducer. Additionally, the motional series resonance and anti-resonance are closely approximated by the frequencies of maximum and minimum admittance, respectively. These frequencies are easier to measure and are used in this work to estimate the efficiency of the transducer.

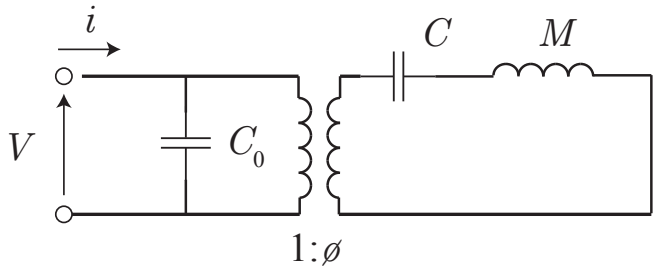

Figure 2.5: Equivalent circuit of idealized piezoelectric transducer.

2.4.2 Input Admittance

The input electrical admittance Y of a piezoelectric transducer is defined as the ratio of the current to the voltage at the electrical input terminals of the transducer, that is, $Y = i/V$. Admittance is typically frequency dependent and complex. It can be presented in terms of its magnitude and phase, $|Y|$ and $\angle Y$ respectively, or written in terms of its real part (conductance G) and imaginary part (susceptance B) as

$$Y = G + jB. \tag{2.33}$$

A representation of admittance in the complex plane is shown in Fig. 2.6.

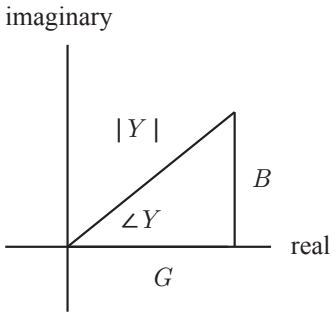

Figure 2.6: Admittance in the complex plane.

Piezoelectric transducers generally have a relatively low admittance, or conversely, a high impedance. Therefore the value of a voltage applied at the transducer can be approximated as independent of the value of the impedance— that is, an applied voltage can be assumed to be a constant voltage source. For a constant voltage source, the power draw, P, of the

transducer, defined as the product of the applied voltage and resulting current, is given by $P = V^2 Y$ [11]. Real, reactive, and apparent powers are found by taking the real part, imaginary part, and absolute value of P respectively. The admittance thus provides direct information on the power draw the transducer will require of an amplifier or associated electrical equipment for a given voltage across all frequencies of interest. As described in Section 2.4.3, the sound pressure produced by the transducer is dependent on the voltage applied, thus the admittance must be known to determine the power needed to produce a desired pressure.

2.4.3 Radial Velocity and Transmit Voltage Response

The transmit voltage response (TVR), or projector sensitivity, of a transducer is the ratio of the on-axis pressure response, p, at 1 meter to the applied voltage, V, when the transducer is deployed underwater. Measurements are typically taken at a distance r in the far field of the transducer and then scaled back to 1 meter assuming spherical spreading and given in decibel form: [11]

$$\text{TVR (dB re 1 } \mu\text{Pa/V at 1 m)} = 20 \log_{10} \left(\frac{pr/V}{M_{\text{ref}}} \right), \tag{2.34}$$

where the reference sensitivity M_{ref} is given by $M_{\text{ref}} = 1\mu\text{Pa} \cdot \text{m/V}$. For this reason it must be kept in mind that the TVR does not represent the pressure response in the near field, and that the near field of the transducer might extend beyond 1 meter.

If the transducer is modeled as a simple source, or point monopole, the pressure p at a distance r from the source may be written in terms of Q, the volume flow of liquid from the source. This relation is given by Blackstock [12] as $p = \rho_0 \dot{Q}/4\pi r$, where ρ_0 is the density of the medium that sound is being radiated into and the dot notation indicates a time derivative. Assuming time-harmonic motion with angular frequency ω, this can be written as

$$p = \frac{j\omega\rho_0 Q}{4\pi r}, \tag{2.35}$$

where j is the imaginary unit. From this equation it can be seen that the strength of the source is directly proportional to the factor $j\omega\rho_0 Q$, which is in essence the apparent mass accelerated by the source.

The volume velocity created by a radiating cylinder of radius a and height h is given by

$$Q = 2\pi a h v_r, \tag{2.36}$$

where $2\pi ah$ represents the lateral surface area of the transducer and v_r is the radial velocity. When calculating the TVR, the cylindrical transducer can be modeled as a spherical source with the volume velocity given by Eq. (2.36), as long as the aspect ratio h/a of the cylinder is close to unity and the wavelength λ of the sound radiated are large compared with the dimensions of the cylinder. This restriction is typically written in terms of the wave number $k = 2\pi/\lambda$ as $ka \ll 1$ and $kh \ll 1$. Combining Eqs. (2.34) through (2.36), the TVR for a cylindrical transducer modeled as a simple source in water is given by

$$\text{TVR (dB re 1 } \mu\text{Pa/V at 1 m)} = 20\log_{10}\left(\frac{j\omega\rho_0 a h v_r}{2VM_{\text{ref}}}\right). \tag{2.37}$$

The factor $j\omega$ in Eq. (2.37) weighs the higher frequencies more heavily than the lows. Nevertheless, the radiated pressure is directly related to the radial velocity v_r, and thus the radial velocity is very useful metric of the transducer behavior. This is especially true when the transducer is tested in air and the TVR metric is not applicable. For these reasons the radial velocity will often be plotted in this thesis as a stand-in for the TVR.

2.4.4 Total Harmonic Distortion

The previous analysis presented in this chapter assumes that fluctuations of field variables about equilibrium are small enough that their governing equations can be taken as linear. However, if the system is driven at sufficiently high amplitudes it may exhibit significant nonlinear effects. Nonlinearities in the electrical and mechanical domains of the transducer can result in an output signal that is not directly proportional to the corresponding input, in which case signal distortion is said to occur. For a steady-state, single frequency input, a distorted output signal is characterized by the presence of multiples of the fundamental input frequency called harmonics. One measure of the amount of distortion in a system is the total harmonic distortion, or THD, defined as follows [13]:

$$\text{THD} = \frac{\sqrt{P_1^2 + P_2^2 + P_3^2 + ...}}{P_0^2 + P_1^2 + P_2^2 + ...} \times 100 \tag{2.38}$$

where P_i is the amplitude of the ith harmonic and P_0 is the amplitude of the signal at the fundamental frequency. The total harmonic distortion will change with frequency and input amplitude as dictated by the nonlinearity in

the system. A high THD is typically undesirable, as it decreases the fidelity of the waveform being transmitted or received by the transducer. Additionally, nonlinear distortion is often an indication that the system is in danger of mechanical failure, electrical breakdown, or overheating [7]. Furthermore, nonlinearites can be difficult to design around, as their physical origin can be difficult to determine and their inclusion in an analytical model of the system can significantly increase its complexity. For these reasons, transducers are often designed in such a way as to minimize nonlinear effects, mostly through the judicious use of damping.

Chapter 3

One-Degree-of-Freedom Lumped Parameter Model of Segmented 31-Mode Ring Transducer

This chapter presents a development of a one-degree-of-freedom model for a piezoelectric 31-mode segmented ring transducer. A pure ring model, similar to that of Sherman and Butler [7], is presented in Section 3.1, followed by a segmented ring model, after Butler [5], in Section 3.2. The model is represented as an equivalent circuit with element values given by material properties of the transducer and surrounding media. Modifications to this model, based on the practical construction and deployment of such devices, are presented in Section 3.3. This type of lumped parameter one-degree-of-freedom model is commonly used and provides a simple means of capturing the basic characteristics of the transducer.

3.1 31-Mode Ring

Consider the cylindrical piezoelectric ring shown in Figure 3.1 with height h, thickness t, and mean radius a (mean value between the inner and outer radii) where $t \ll a$. Let x_1, x_2, and x_3 be the local coordinate axes along

the circumferential, vertical, and radial directions, respectively. As discussed in Section 2.1, the state of the piezoelectric material (in terms of stress, strain, electric field, and electric displacement) will vary with direction and must be described with multi-dimensional matrices, the entries of which are subscripted to indicate the direction along which the property is taken. These values are governed by the constitutive equations given in Eqs. (2.13) and (2.14). The transducer is excited by a voltage applied in the radial direction across the ring, producing an electric field E_3 which in turn creates a strain S_1 along the circumference proportional to the applied voltage. Because a voltage applied along x_3 is used to drive strain along x_1, this ring is designated as a 31-mode ring transducer.[1]

Approximations can be made based on the specific geometry of the piezolelectric ring that allow many effects to be neglected and the matrix constitutive equations to be reduced to a single dimension. For this transducer, the electric field is applied only in the radial direction. If the thickness t is small compared with the ring height h, fringing effects can be ignored and $E_1 = E_2 = 0$ may be approximated. Further, by assuming the circumference of the ring to be much greater than the thickness or height and the ring to be unconstrained along the thickness or height, a uni-axial stress condition where $T_2 = T_3 = 0$ throughout the entire element and at its boundaries may be approximated[2].

[1]It is possible to interchange x_1 and x_2 in the coordinate system described above and have the following analysis hold for a 32-Mode transducer. The analysis here is presented for a 31-Mode transducer to maintain consistency with our references, with the understanding that the 1 and 2 directions are interchangeable.

[2]This assumption becomes less accurate as the ring height increases, or as multiple rings

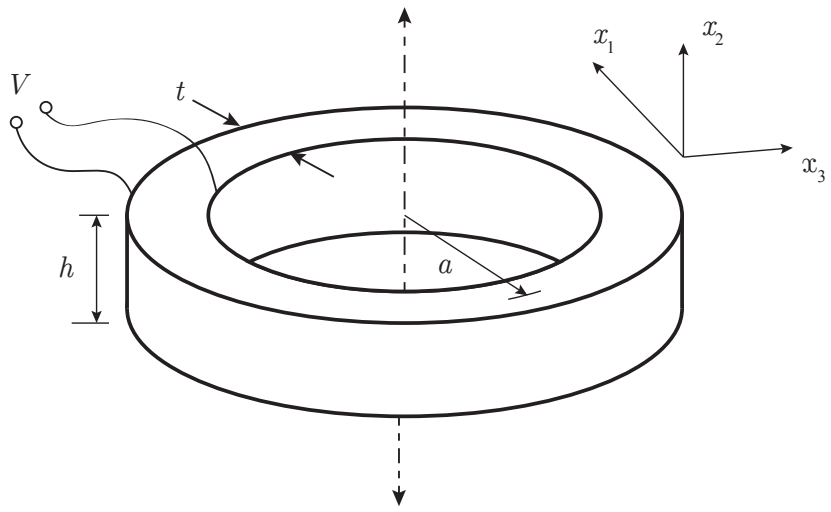

Figure 3.1: Cylindrical piezoelectric ring with height h, thickness t, and mean radius a.

Finally, in this particular configuration, only the circumferential strain, S_1, and electric displacement, D_3, are of concern, as those fields will dominate the dynamic behavior of the ring when its circumference is much larger than its height or thickness. Thus the canonical equations given by Eqs. (2.13) and (2.14) reduce to

$$S_1 = s_{11}^E T_1 + d_{31} E_3 \tag{3.1}$$

$$D_3 = d_{31} T_1 + \epsilon_{33}^T E_3, \tag{3.2}$$

are stacked on one another, in which cases significant stress can be generated along the ring height, which stiffens the ring and produces a higher-frequency resonance.

where s_{11}^E is an elastic compliance at constant electric field, d_{31} is a piezoelectric strain constant, and ϵ_{33}^T is a dielectric constant at constant applied stress. In all cases the constants are subscripted according to piezoelectric convention, representing the effect along the direction of the second subscript arising from an applied force or electric field at the face normal to the direction of the first subscript.

3.1.1 Effect of Applied Voltage

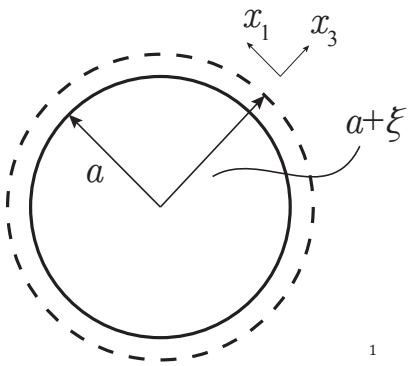

Figure 3.2: Radial displacement of ring.

Equations (3.1) and (3.2) can now be used to model the dynamic behavior of the 31-mode ring. If a time-varying voltage V is applied across the ring thickness an electric field will result that, if fringing effects are ignored, is well approximated by

$$E_3 = V/t. \tag{3.3}$$

This will remain the case as long as the frequency content of the applied

signal is well below the thickness resonance of the ring.[3] As a result of this electric field, the ring will expand or contract (depending on the sign of the electric field) proportionally in the circumferential direction, resulting in a displacement, ξ , in the radial direction, as shown in Figure 3.2. The original circumference is defined as $X_0 = 2\pi a$, and the circumference after the radial displacement is $X = 2\pi(a + \xi) = 2\pi a + 2\pi\xi = X_0 + \delta X$, where $\delta X = 2\pi\xi$. The circumferential strain S_3 due to the applied voltage is thus approximately given by

$$S_3 = \delta X / X_0 = \xi / a. \tag{3.4}$$

The associated stress, T_3, is the force, F, perpendicular to any cross section generated by a planar cut aligned with the radial direction divided by the cross-sectional area, that is,

$$T_3 = F/(th). \tag{3.5}$$

Substituting Eqs. E:E3 through 3.5 in Eq. (3.1) and solving for F yields

$$F = \left(\frac{th}{s_{11}^E a}\right)\xi - \left(\frac{hd_{31}}{s_{11}^E}\right)V. \tag{3.6}$$

This force, perpendicular to a cross section of the ring, is used to derive the radial equation of motion in the following section.

[3]The ring will resonate along the thickness of the ring when standing waves occur along that direction. The first such mode will occur wavelength λ is such that the thickness is $t = \lambda/2 = c/(2f)$, where c is the sound speed in the material along the thickness direction and f is the frequency of applied voltage. Here it is assumed that the frequency content of the signal is such that $t \ll \lambda/2$.

3.1.2 Radial Equation of Motion

To find the dynamic behavior of the entire 31-mode ring, we first consider the dynamic behavior of a differential element subject to time-harmonic electric excitation. The differential element of interest is a small portion of the ring that subtends an angle $\delta\theta$. When this element is cut from the ring, reaction forces of magnitude F acting on either side of the element are exposed. As shown in Figure 3.3(a), the circumferential components of the reaction forces on each cut face cancel, while radial components add to produce a net radial force, F_{r}, given by $F_{\mathrm{r}} = 2F\sin(\delta\theta/2)$. Using a small angle approximation, $\delta\theta \ll 1$, one can take $\sin(\delta\theta/2) \approx \delta\theta/2$ to yield $F_{\mathrm{r}} \approx F\delta\theta$. Placing the further restriction that F remain constant for all θ and letting $\delta\theta$ become infinitesimally small, the total radial force is then given by $F_{\mathrm{r}}^{\mathrm{total}} = \int_0^{2\pi} F\delta\theta = 2\pi F$.

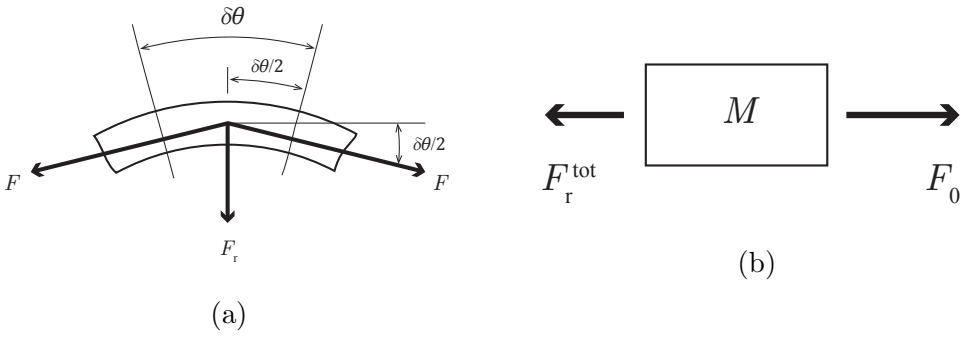

Figure 3.3: Forces on (a) mass of differential element of ring and (b) entire lumped mass of ring.

This total radial force contributes to the acceleration of the mass of the

ring, given by

$$M = \rho 2\pi a t h, \tag{3.7}$$

where ρ is the mass density of the material. This mass is accelerated by the net radial force $F_{\mathrm{r}}^{\mathrm{total}}$ and an additional radial force, F_0, which can be used to account for radiation loads, coupling from other domains, or incoming acoustic waves. The subsequent radial ring motion is governed by Newton's second law as depicted in the free-body diagram in Fig. 3.3(b). The radial equation of motion is thus

$$M\ddot{\xi} = F_0 - F_{\mathrm{r}}^{\mathrm{total}} = F_0 - 2\pi F = F_0 - 2\pi \left[\left(\frac{th}{s_{11}^E a} \right) \xi - \left(\frac{h d_{31}}{s_{11}^E} \right) V \right], \tag{3.8}$$

where the dot convention has been employed to indicate time derivatives and F has been replaced with the expression obtained in Eq.(3.6). Damping can be included as a viscous loss via a damping coefficient R_{m}, which is a function of the material properties of the ring. With this damping term added, Eq. (3.8) can then be re-arranged in the form of a classical inhomogeneous second-order ordinary differential equation for the radial displacement ξ:

$$M\ddot{\xi} + R_{\mathrm{m}}\dot{\xi} + \left(\frac{2\pi t h}{s_{11}^E a} \right) \xi = \left(\frac{2\pi h d_{31}}{s_{11}^E} \right) V + F_0. \tag{3.9}$$

In this sense the vibration of the ring about its equilibrium radius can be viewed as the motion of a damped spring-mass oscillator with mass M and radial stiffness $K^E = \frac{2\pi t h}{s_{11}^E a}$ (or inversely radial compliance $C^E = 1/K^E$), where the superscript E denotes the parameter given for a constant electric field, or short-circuit ($V = 0$), condition. The electromechanical coupling is expressed

via the coefficient

$$\phi = \frac{2\pi h d_{31}}{s_{11}^E}, \tag{3.10}$$

that allows the applied voltage to enter the equation as a force source. In this sense ϕ can be considered a "turns ratio" for an ideal transformer, coupling the electrical and mechanical domains in an equivalent circuit of the transducer as described in Section 3.1.4. With these coefficients defined, Eq. (3.9) may be written as

$$M\ddot{\xi} + R_{\mathrm{m}}\dot{\xi} + K^E\xi = \phi V + F_0. \tag{3.11}$$

3.1.3 Radial Velocity Sensitivity

For time-harmonic motion, the radial displacement can be given by $\xi = \xi_0 e^{j\omega t}$, where ω is the angular frequency and j is the imaginary unit. In this case, the velocity and acceleration are given by $v = \partial\xi/\partial t = j\omega\xi$ and $\partial v/\partial t = \partial^2\xi/\partial^2 t = -\omega^2\xi = j\omega v$, respectively. Thus, writing the equation of motion Eq. (3.11) in terms of the velocity v yields

$$j\omega v M + R_{\mathrm{m}} v + \frac{1}{j\omega C^E} v = \phi V + F_0. \tag{3.12}$$

Note that the mechanical compliance C^E has been used in place of the stiffness K^E in anticipation of an equivalent circuit model.

It is now further assumed that F_0 is due to the effects of acoustic radiation loads, and thus the resolved force on the ring is approximated as $F_0 = -Z_{\mathrm{rad}} v$, where Z_{rad} is the radiation impedance as dictated by ring geometry and frequency and the negative sign accounts for F_0 acting in the direction

opposing motion. Accounting for the above and rearranging Eq. (3.12) yields the following equation relating the radial velocity of the ring v to the applied voltage V:

$$\left(j\omega M + Z_{\text{rad}} + R_{\text{m}} + \frac{1}{j\omega C^E}\right) v = \phi V. \tag{3.13}$$

This equation can be solved for the frequency-dependent ratio v/V, known as the radial velocity sensitivity because it calculates the output radial velocity of the ring resulting from a unit amplitude drive voltage input:

$$H_{V\text{-}v} \equiv v/V = \frac{\phi}{Z_{\text{rad}} + R_{\text{m}} + j\omega M + \frac{1}{j\omega C^E}}. \tag{3.14}$$

If the system is undamped and unloaded, that is, if $R_{\text{m}} = Z_{\text{rad}} = 0$, $H_{V\text{-}v}$ becomes unbounded when

$$\omega^2 = \omega_0^2 \equiv \frac{1}{MC^E}, \tag{3.15}$$

where ω_0 is known as the free mechanical resonance frequency. In terms of this resonance frequency, the radial velocity sensitivity is

$$H_{V\text{-}v} = \frac{\phi}{Z_{\text{rad}} + R_{\text{m}} + j\omega M\left(1 - (\omega_0/\omega)^2\right)}. \tag{3.16}$$

3.1.4 Admittance

Any electroacoustic transducer is coupled to an electrical system and therefore must consider power draw and matching to electrical circuitry. For this reason it is useful to determine the input electrical admittance of the system, as it provides information about its performance in the electrical domain.

To determine the input admittance at the electrodes, the canonical Equations (3.1) and (3.2) can be combined to eliminate stress T_1 for an expression representing electric displacement D_3 in terms of strain S_1 and electric field E_3.:

$$D_3 = d_{31}\left(\frac{1}{s_{11}^E}S_1 - \frac{d_{31}}{s_{11}^E}E_3\right) + \epsilon_{33}^T E_3 \tag{3.17}$$

or

$$D_3 = \frac{d_{31}}{s_{11}^E}S_1 + \left(\epsilon_{33}^T - \frac{d_{31}^2}{s_{11}^E}\right)E_3. \tag{3.18}$$

The clamped (S_1 = constant) dielectric constant can be defined as $\epsilon_{33}^S \equiv \frac{\partial D_3}{\partial E_3}|_{S_1} = \epsilon_{33}^T - d_{31}^2/s_{11}^E$. Using the piezoelectric coupling factor defined in Section 2.4.1, $k_{31}^2 = \frac{d_{31}^2}{s_{11}^E \epsilon_{33}^T}$, the clamped dielectric constant may be written as $\epsilon_{33}^S = \epsilon_{33}^T(1 - k_{31}^2)$. Writing Eq. (3.18) in terms of the clamped dielectric constant yields

$$D_3 = \frac{d_{31}}{s_{11}^E}S_1 + \epsilon_{33}^S E_3. \tag{3.19}$$

With electric displacement D_3 defined as charge, Q, per unit area, and S_1 and E_3 given as ξ/a and V/t respectively, Eq. (3.19) may be written as

$$\frac{Q}{2\pi a H} = \frac{d_{31}}{s_{11}^E}\left(\frac{\xi}{a}\right) + \epsilon_{33}^S\left(\frac{V}{t}\right) \tag{3.20}$$

or

$$Q = \frac{2\pi h d_{31}}{s_{11}^E}\xi + C_0 V \tag{3.21}$$

where the clamped capacitance C_0 is defined by

$$C_0 \equiv \frac{\partial Q}{\partial V}|_{S_1} = \frac{2\pi h \epsilon_{33}^S}{t}. \tag{3.22}$$

Assuming a time-harmonic input voltage, that is, $V = V_0 e^{j\omega t}$, and noting that current $I = \partial Q/\partial t$, one may differentiate both sides of Eq. (3.21) to obtain

$$i = \frac{2\pi h d_{31}}{s_{11}^E} v + C_0 \frac{\partial V}{\partial t}. \tag{3.23}$$

Writing $\frac{\partial V}{\partial t}$ as $j\omega V$ and using Eq. (3.10), Eq. (3.23) may be written as

$$i = \phi v + j\omega C_0 V. \tag{3.24}$$

The input electrical admittance of the system is then given by

$$Y_{\text{in}} = \frac{i}{V} = \phi \left(\frac{v}{V}\right) + j\omega C_0 = \phi H_{V\text{-}v} + j\omega C_0. \tag{3.25}$$

Finally, using the radial velocity sensitivity $H_{V\text{-}v}$ from Eq. (3.16) and accounting for any electrical loss conductance with $G_0 = \omega C_{\text{f}} \tan\delta$ [7], we obtain

$$Y_{\text{in}} = \frac{\phi^2}{Z_{\text{rad}} + R_{\text{m}} + j\omega M \left(1 - (\omega_0/\omega)^2\right)} + j\omega C_0 + G_0. \tag{3.26}$$

This system can be modeled with the equivalent circuit shown in Fig. 3.4.

When deployed in the field, cylinders are often formed by stacking multiple rings in order to provide sufficient source level. Because the values of all elements shown on the circuit model are directly proportional to the ring height h, one can model a stack of such transducers as a single ring using the circuit model shown in Fig. 3.4 simply by multiplication of all values of the elements (including the turns ratio ϕ) by N_{R}, the number of rings. The exception to this is the (short-circuit) mechanical compliance C^E which is inversely proportional to h and is thus divided by N_{R}. It must be noted, however, that

model will lose validity if the cylinder height, given by $N_{\mathrm{R}}H$, becomes too large. The uni-axial stress condition ($T_2 = T_3 = 0$) discussed at the beginning of this chapter is violated when the cylinder height is large enough for significant stresses to build up along the axial direction (x_2). Additionally, the approximation of the cylindrical transducer as a spherical source becomes less valid as the aspect ratio h/a increases, as discussed in Section 2.4.3.

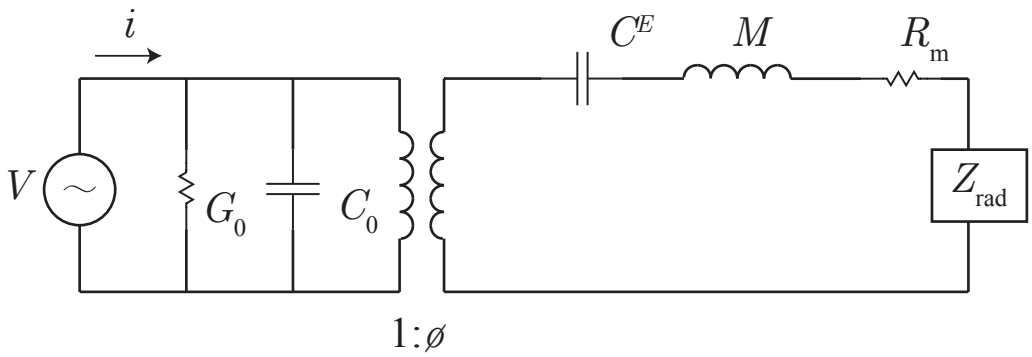

Figure 3.4: Lumped element circuit model for 31-mode ring.

$$G_0 = \omega C_{\mathrm{f}} \tan\delta \qquad C_0 = \frac{2\pi a h \epsilon_{33}^S}{t} \qquad \phi = \frac{2\pi h d_{31}}{s_{11}^E}$$

$$C^E = \frac{s_{11}^E a}{2\pi t h} \qquad M = \rho 2\pi a t h$$

3.2 Segmented Ring

The above analysis can be used to approximate the behavior of a segmented piezoelectric ring transducer composed of alternating segments of active and inactive material, as depicted schematically in Fig. 3.5. The electromechanical dynamic behavior of such a ring will in principle remain the same as the purely piezoelectric ring, though the physical properties will change due to the added inactive material. The analysis provided here derives approximate effective properties for the short-circuit compliance $s_{11}^{E,\text{eff}}$, density ρ^{eff}, piezoelectric constant d_{31}^{eff}, and stress-free permittivity ϵ_{33}^{T} for the composite ring based on the material properties of the active and inactive elements.

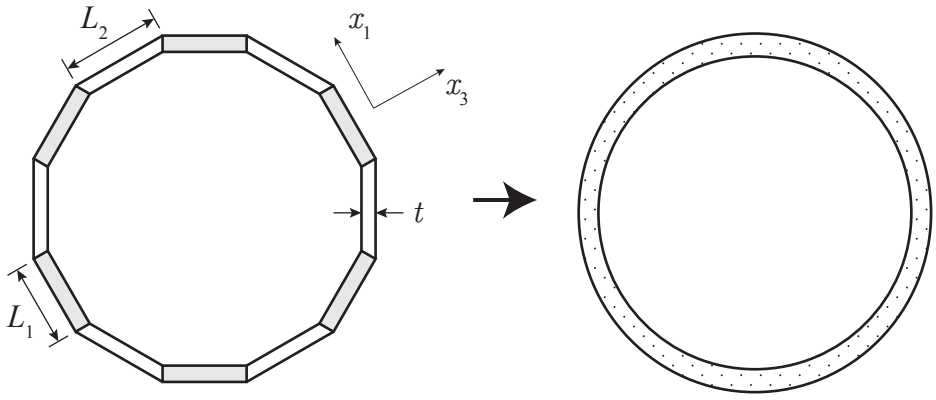

Figure 3.5: Segmented ring.

The treatment provided here assumes that the width (along x_3) and height (along x_2) dimension of each elements are equal and given by t and

h, respectively. Furthermore, it is assumed that the number of active and inactive elements is equal and given by n. These assumptions are consistent with typical segmented ring transducer designs. For the following analysis, element properties are subscripted with i, where $i = 1$ and $i = 2$ indicate properties of the active and inactive elements respectively.

The segmented ring can be represented as a grouping of n unit cells, containing one active and one inactive element each. Each cell has length $L_{\text{unit}} = L_1 + L_2$, where L_1 and L_2 are the active and inactive element lengths, respectively. The total circumferential length of the composite ring can then be written as $L = nL_{\text{unit}}$.

3.2.0.1 Effective Short-Circuit Compliance

An effective short-circuit compliance for the composite ring can be found by considering the change in length of the ring due to a uniform force acting along its circumference (as depicted in Fig. 3.3(a)). This can be visualized by imagining the ring "unwound" and allowed to stand vertically on its end, as shown in Fig. 3.6, with the force imposed at one end and a fixed boundary condition on the other to enforce symmetry. The analysis presented here is done in terms of an effective Young's modulus, given by

$$Y^{\text{eff}} = \frac{1}{s_{11}^{E,\text{eff}}}. \tag{3.27}$$

The force F applied in the x_1 direction (here vertical) will change the total length L by an amount δL and each individual element by an amount

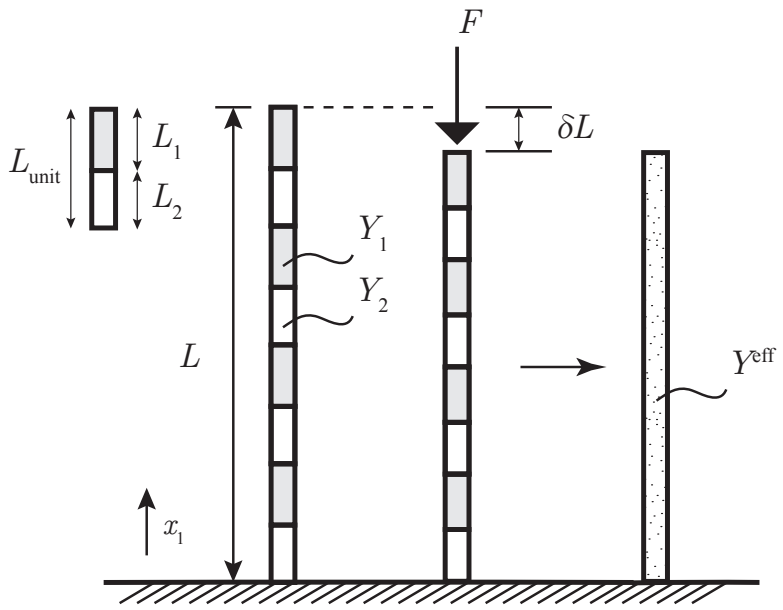

Figure 3.6: "Unwound" segmented ring.

δL_i. This applied force creates stress in each element given by $T = F/A$, where A is the cross-sectional area of the elements given by $A = ht$. Assuming a uni-axial stress state, the stress is given by Hooke's law as $T = Y_i S_i$, where S_i is the strain induced along x_1 in each element and is well approximated as $S_i = \delta L_i / L_i$. The change in length for each individual element can thus be written as

$$\delta L_i = S_i L_i = \frac{T L_i}{Y_i}. \tag{3.28}$$

The total change in length of the unwound ring is $\delta L = n\left(\delta L_1 + \delta L_2\right)$ or, using Eq. (3.28),

$$\delta L = n\left(\frac{L_1}{Y_1} + \frac{L_2}{Y_2}\right) T. \tag{3.29}$$

This total change in length δL of the unraveled ring can also be written in terms of an effective Young's modulus Y^{eff} for the composite ring:

$$\delta L = \frac{TL}{Y^{\text{eff}}}. \tag{3.30}$$

Combining Eqs. (3.29) and (3.30), eliminating T and solving for $1/Y^{\text{eff}}$ yields

$$\frac{1}{Y^{\text{eff}}} = \left(\frac{nL_1}{L}\right)\frac{1}{Y_1} + \left(\frac{nL_2}{L}\right)\frac{1}{Y_2} = \left(\left(\frac{L_1}{L_{\text{unit}}}\right)\frac{1}{Y_1} + \left(\frac{L_2}{L_{\text{unit}}}\right)\frac{1}{Y_2}\right). \tag{3.31}$$

The length fraction of unit cell that is material i may be definied as $\phi_i = L_i/L_{\text{unit}}$[4]. It is often convenient to write effective properties in terms of the length fraction of inactive interstitial material, $\phi_2 = l_2/L_{\text{unit}}$. ϕ_1 can then be written as $\phi_1 = 1 - \phi_2$. Eq. (3.31) may be written in terms of ϕ_2 to show the effective Young's modulus as a length-fraction-weighted harmonic average of the Young's moduli of each of the constituent materials:

$$\frac{1}{Y^{\text{eff}}} = \frac{1-\phi_2}{Y_1} + \frac{\phi_2}{Y_2}. \tag{3.32}$$

In terms of the effective short-circuit compliance, given Eq. (3.27), Eq. 3.33 may be written as

$$s_{11}^{E,\text{eff}} = \frac{1-\phi_2}{Y_1} + \frac{\phi_2}{Y_2}. \tag{3.33}$$

Eq. 3.33 provides a convenient approximation for the effective short-circuit compliance of the segmented ring, and is equivalent to the constant stress Reuss approximation for the effective elastic parameters of a composite material.

[4]Note that here ϕ is a length fraction and not a transformer turns ratio.

3.2.0.2 Effective Density

The effective density ρ^{eff} can be determined from the ratio of the mass and volume of the unit cell, that is, $\rho^{\text{eff}} = M_{\text{unit}}/V_{\text{unit}} = (\rho_1 AL_1 + \rho_2 AL_2)/(AL_{\text{unit}})$. In terms of length fraction ϕ_2 the effective density is

$$\rho^{\text{eff}} = \rho_1 (1 - \phi_2) + \rho_2 \phi_2. \tag{3.34}$$

3.2.0.3 Effective Coupling Coefficient and Piezolectric Constant

A similar analysis yields effective properties for the piezoelectric strain constant and dielectric constant in terms of the length fraction of inactive material:

$$d_{31}^{\text{eff}} = d_{31} (1 - \phi_2), \tag{3.35}$$

and

$$\epsilon_{33}^{\text{eff}} = \epsilon_{31} (1 - \phi_2). \tag{3.36}$$

Note that *i* the inactive material by definition has a piezoelectric strain constant and dielectric constant equal to zero and *ii* the effective properties shown above go to zero when the length fraction of inactive material approaches unity.

To model the segmented ring, the effective properties defined in Eqs. (3.33) through (3.36) may be substituted in place of the material properties defining the lumped parameters for the circuit model of the transducer shown in Fig. 3.4. The resulting one-degree-of-freedom model for the segmented ring is referred to here as "Model 1" to distinguish it from subsequent models with more degrees of freedom.

Plots of the magnitude and phase of the input admittance and radial velocity for the segmented ring transducer, using material parameters and dimensions for the ring given in Appendix A, are shown in Figs. 3.7 and 3.8. A distinct peak can be observed in the admittance and radial velocity curves, representing a mechanically free resonance. Additionally, a valley representing an anti-resonance can be observed in the admittance plot. The resonance frequency is $f_0 = \omega_0/(2\pi)$, where ω_0 is given by Eq. (3.15). This plot, and all subsequent plots, have been plotted against frequency normalized by this value. The levels of all plots are normalized by a reference value (subscripted with "ref"), representing the maximum value of the quantity given by Model 1 for the in-water case (discussed in Section 3.3.2).

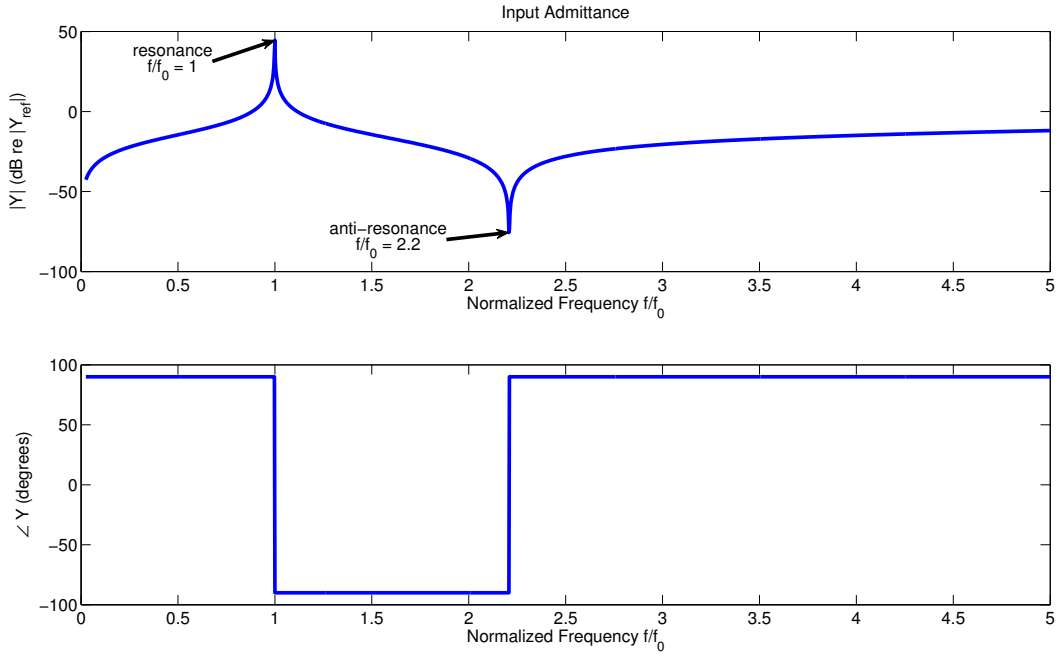

Figure 3.7: Input admittance of segmented ring transducer as given by Model 1.

3.3 Modifications to Model

The idealized model of the ring described above and depicted in the equivalent circuit shown in Fig. 3.4 does not account for many of the effects that are encountered when such rings are physically constructed and deployed in the field. Filament winding to impart a compressional pre-stress and urethane overmolding for sealing in aqueous environments are common modifications applied to the segmented ring transducer in order to increase its stability and durability. Such effects primarily add mass, stiffness, and damping to the transducer which can be accounted for in the model's mechanical lumped parameters. Additionally, the transducer is designed to radiate sound into a

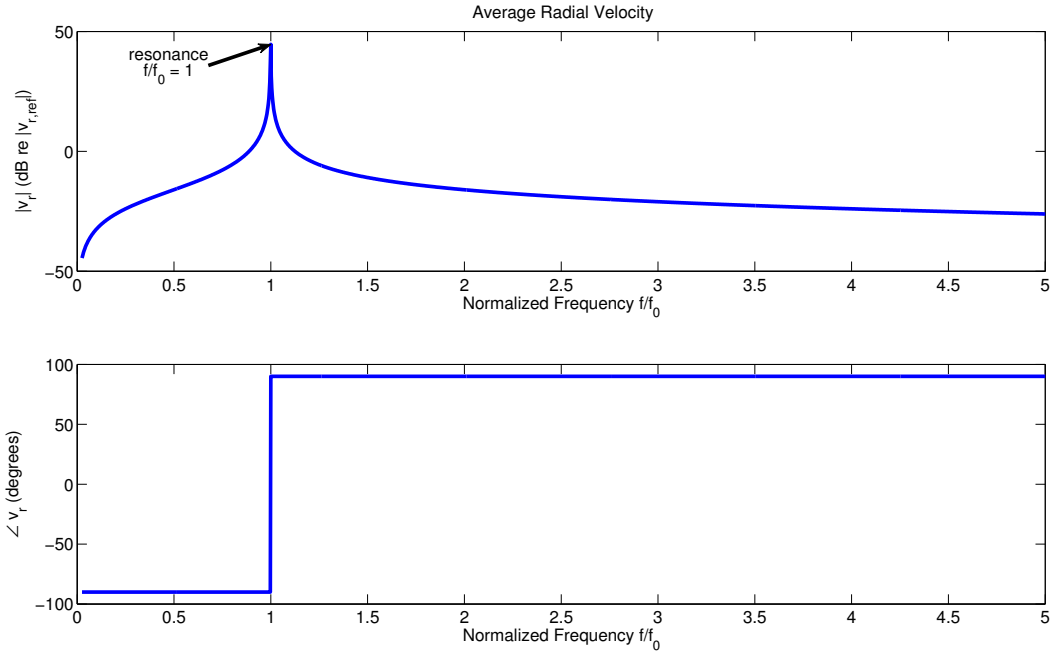

Figure 3.8: Average radial velocity of segmented ring transducer as given by Model 1.

medium so an accurate model of the radiation load which considers the finite geometry of the transducer must be considered. Similarly, the internal volume of such rings are commonly filled with oil or some other substance to prevent them from collapsing under ambient external pressure when submerged. This internal volume presents an impedance that effects the performance of the ring and must be accounted for. The radiation and internal volume impedances are often complex and frequency dependent, and are usually represented as separate block impedances, as shown in Fig. 3.9. The following sections detail how these effects are included through modifications to the previously presented model.

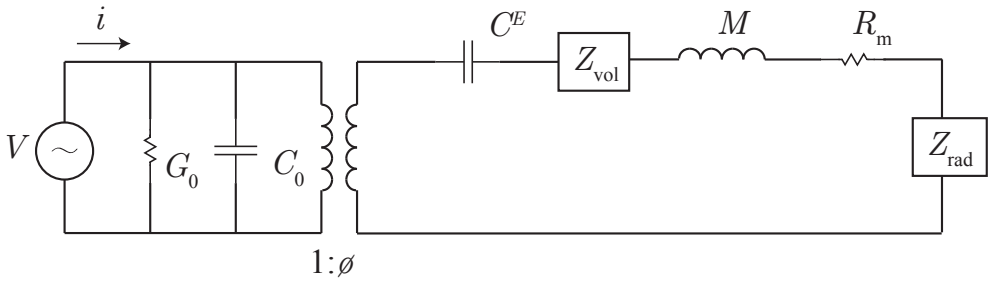

Figure 3.9: Lumped element circuit model for 31-Mode ring with block impedances for acoustic radiation and internal volume, defined in Sections 3.3.2 and 3.3.3 respectively.

3.3.1 Filiment Winding Effects

Segmented ring transducers are often encircled about their circumference with a pre-compressional filament winding in order to force all active elements to remain in compression when driven, since they readily fracture in tension. Because the filament winding is often a very thin layer of material, it typically adds more stiffness than mass to the system and thus pushes the resonances up to higher frequencies.

The mass added by the winding is equivalent to

$$M_{\mathrm{w}} = 2\pi a_{\mathrm{w}} t_{\mathrm{w}} h_{\mathrm{w}} \rho_{\mathrm{w}}, \tag{3.37}$$

where all parameters indicate the same properties as in Eq. 3.7, with the subscript "w" used to indicate properties of the winding. Typically the winding does not cover the full height of the ring and h_{w} is some fraction of h.

The force F_{w} due to the winding is similar to the force F derived for Eq. 3.6, except here of course the piezoelectric strain constant for the winding

is assumed to be zero and there is no voltage term. The radial force due to the winding is then

$$F_{\mathrm{w}} = \frac{t_{\mathrm{w}} h_{\mathrm{w}}}{s_{11}^{E,\mathrm{w}} a_{\mathrm{w}}} . \xi \tag{3.38}$$

The stiffness added to the entire ring due to the winding is the ratio of winding force to displacement, and given as

$$K_{\mathrm{w}} = \frac{2\pi t_{\mathrm{w}} h_{\mathrm{w}}}{s_{11}^{E,\mathrm{w}} a_{\mathrm{w}}}. \tag{3.39}$$

The total mass and mechanical stiffness of the ring is given by $K^{E,\mathrm{total}} = K^E + K_{\mathrm{w}}$ and $M^{\mathrm{total}} = M + M_{\mathrm{w}}$. The analysis in Sections 3.1.3 and 3.1.4 and the circuit model shown in Fig. 3.4 can be modified to account for the winding by replacing M with M^{total} and K^E with $K^{E,\mathrm{total}}$. Any mechanical aspects of the ring that primarily add mass or stiffness, such as polymer overmolding, can be dealt with in a similar fashion.

Plots of the magnitude and phase of the input admittance and radial velocity for a ring with various layers of filament winding (winding height $h_{\mathrm{w}} = 0.85h$) with typical material parameters and dimensions for a segmented ring (as given by Appendix A) are shown in Figs. 3.10 and 3.11. The added stiffness due to the winding pushes the primary resonance of the system up significantly, and this effect is increased as the number of winding layers is increased.

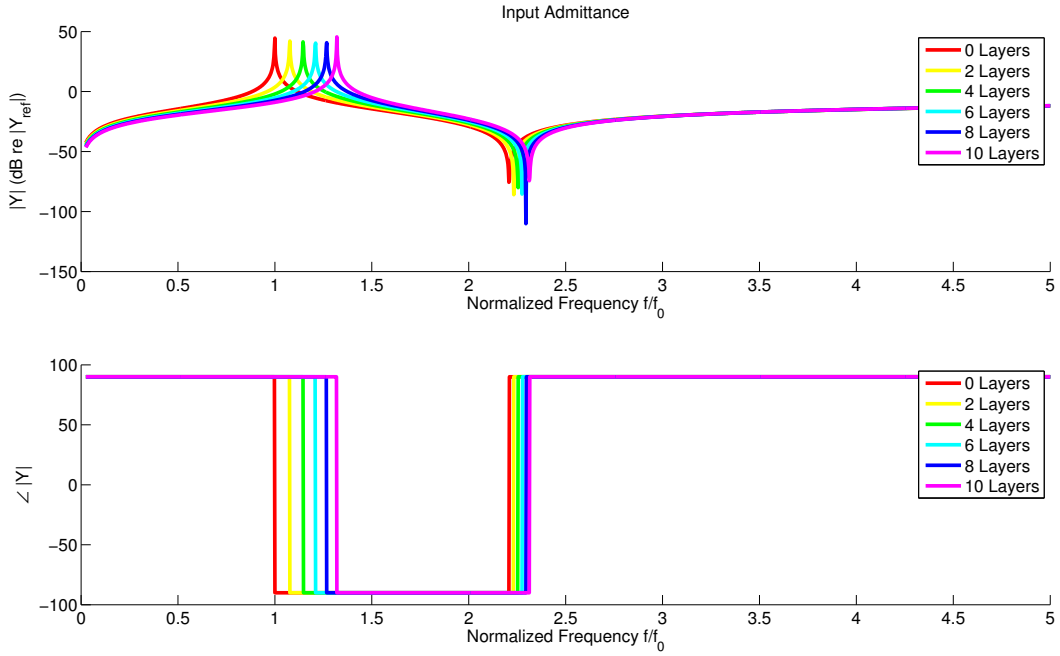

Figure 3.10: Input admittance of segmented ring transducer with various layers of winding.

3.3.2 Radiation Impedance

The medium that the ring is radiating into presents an impedance to the ring that may significantly alter its performance. This impedance is modeled most simply as that of a vibrating sphere with an equivalent volume, as shown by Sherman and Butler [7] and presented here in Section 3.3.2.1, or more accurately, as that of a finite cylinder, as shown by Butler [14] and presented here in Section 3.3.2.2. The medium itself is characterized by density ρ_0 and sound speed c_0.

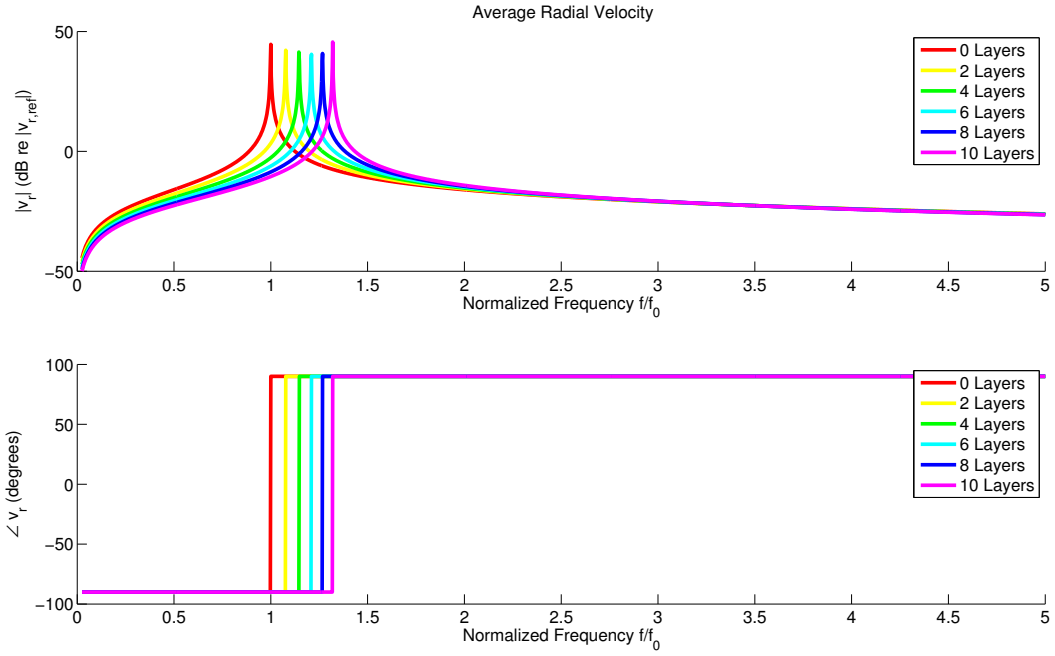

Figure 3.11: Radial velocity of segmented ring transducer with various layers of winding.

3.3.2.1 Equivalent Sphere

The specific acoustic radiation impedance of a pulsating sphere of radius a_{sph} is given by Blackstock [12] as

$$Z_{\text{rad,spac}} = \rho_0 c_0 \left(\frac{k^2 a_{\text{sph}}^2}{1 + k^2 a_{\text{sph}}^2} + j \frac{k a_{\text{sph}}}{1 + k^2 a_{\text{sph}}^2} \right), \tag{3.40}$$

where $k = \omega / c_0$ is the wave number. Given that a sphere has surface area $A = 4\pi r^2$, the mechanical radiation impedance is given by

$$Z_{\text{rad}} = 4\pi k a_{\text{sph}}^3 \rho_0 c_0 \frac{k a_{\text{sph}} + j}{1 + k^2 a_{\text{sph}}^2}. \tag{3.41}$$

A cylindrical ring with radius a and height h has volume $V_{\text{cyl}} = \pi a^2 h$ and a sphere of radius a_{sph} has volume $V_{\text{sph}} = \frac{4}{3}\pi r^3$. Setting these two volumes

equal to each other and solving for a_{sph} yields the radius of a sphere with equivalent volume:

$$a_{\text{sph}} = \left(\frac{3}{4}a^2 h\right)^{1/3}. \tag{3.42}$$

Substituting Eq. (3.42) into Eq. (3.41) provides an estimation of the radiation impedance seen by the cylindrical ring. This is a low frequency approximation that holds for wavelengths much larger than the a and h length dimensions of the transducer. These conditions are most commonly written in terms of the wave number k as $ka \ll 1$ and $kh \ll 1$.

3.3.2.2 Finite Cylinder

Equation (3.41) provides a first-order approximation of the effects of the radiation impedance, provided that the cylinder aspect ratios are close to unity and that their size is small compared to a wavelength ($ka \ll 1$ and $kH \ll 1$). For the cylinder dimensions given in Appendix A, these conditions do not hold in the frequency range of interest. A more accurate, though computationally demanding, model is provided by Butler and Butler [14]. In that work, the authors provide an estimate of the radiation impedance for a finite height cylindrical transducer using a periodic replicated model where an active cylinder system is capped by rigid cylindrical extensions and replicated to $\pm\infty$ with period d. This periodic replication allows the cylindrical wave equation for the acoustic pressure to have Fourier series solution. The period d must be chosen to be large enough so that the pressure on one radiating cylinder resulting from all of the others is negligible. It should also be noted

that this model cannot be used to create a valid far-field solution for a single cylinder. In the far field, the distances from the single cylinder and the replicas appear roughly the same, thus the replicas will contribute almost equally to the pressure field.

Butler and Butler give the mechanical radiation impedance for a finite cylinder as

$$Z_{\text{rad}} = \sum_{n=0}^{\infty} j\pi a H^2 \rho_0 \omega \delta_n \sum_{m=0}^{\infty} \epsilon_m \,\text{Sinc}^2\left(\frac{\alpha_m H}{2}\right) \frac{H_n(\beta_m a)}{\beta_m d H_n'(\beta_m a)}, \tag{3.43}$$

where

$$\delta_n = \begin{cases} 2, & \text{if } n = 0; \\ 1, & \text{otherwise.}, \end{cases} \tag{3.44}$$

$$\epsilon_m = \begin{cases} 1, & \text{if } m = 0; \\ 2, & \text{otherwise.}, \end{cases} \tag{3.45}$$

H_n is the Hankel function of order n, $\alpha_m = m2\pi/d$, $\beta_m = k^2 - \alpha_m^2$, and d is the replication distance (taken to be as large as computationally possible) used for a Fourier series solution.

Fig. 3.12 is a comparison of the real (resistive) and imaginary (reactive) parts of the radiation impedances given by Eqs. (3.41) and (3.43), for the ring dimensions given by Appendix A. It can be seen that for both models, the impedance is mass-like at low frequencies with the reactive part dominating. As the frequency increases, the radiation impedance becomes more resistive as the real part increases and the reactive part decreases. The radiation impedance of the equivalent sphere is significantly higher in magnitude

than that of the finite cylinder of the same volume. Additionally, the reactive part of the equivalent sphere model decreases much more dramatically with increasing frequency than the finite cylinder impedance. The MATLAB script used for the finite cylinder impedance is included in Appendix E.

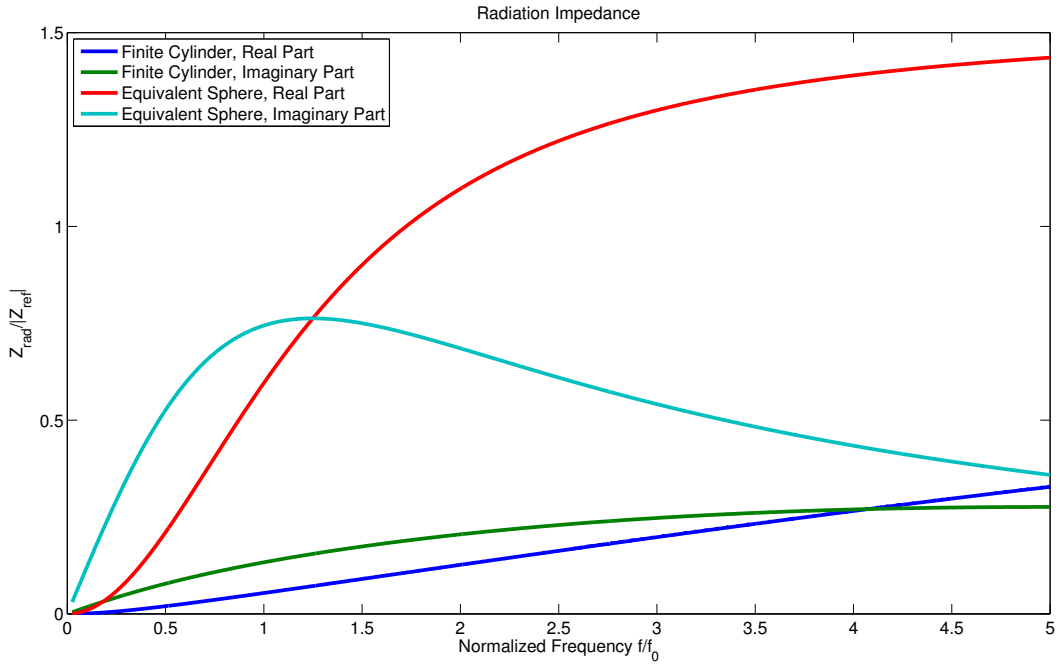

Figure 3.12: Real and imaginary parts of the radiation impedance due to water loading, for the transducer ring modeled as an equivalent sphere and finite cylinder.

Figs. 3.16 and 3.17 show the input admittance and radial velocity of the segmented ring in water subject to the radiation impedance of an equivalent sphere and finite cylinder. For both models, it can be seen that the radiation impedance reduces the amplitude and sharpness of the resonance and decreases the frequency at which it occurs. This effect is expected as both radiation

impedances are primarily mass-like at low frequencies. The effect is more dramatic when the radiation impedance is modeled as an equivalent sphere, as it has a significantly higher magnitude than the finite cylinder radiation impedance. The maximum amplitude of the admittance and radial velocity for the in-water case (when the radiation impedance is modeled as that of a finite cylinder) are referred to here as Y_{ref} and $v_{r,\text{ref}}$ respectively, and are used as reference values to normalize other plots in this thesis as indicated.

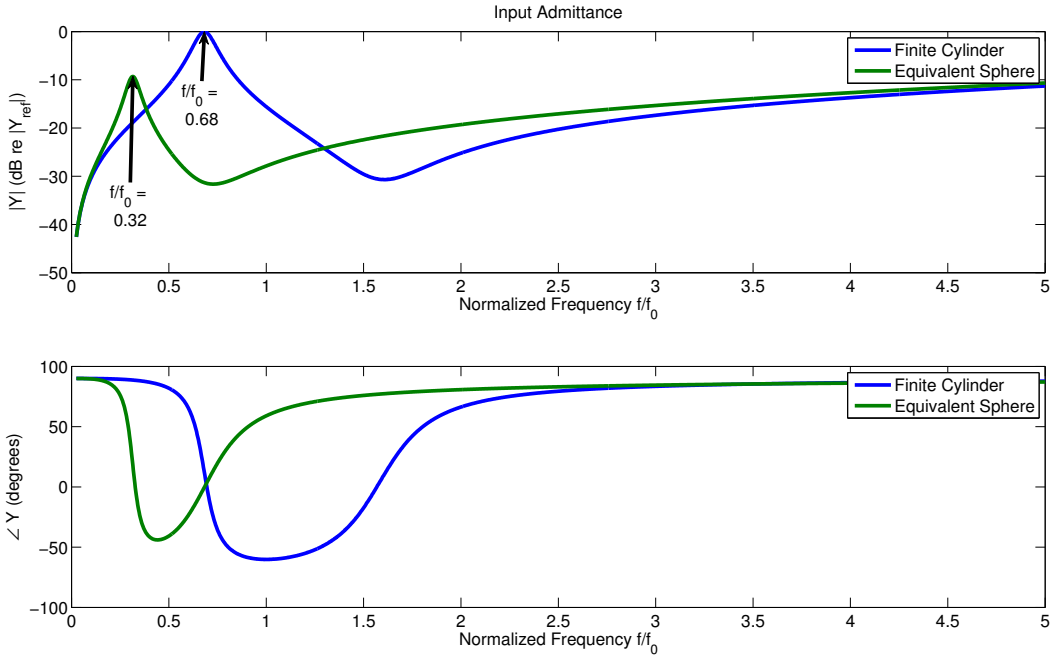

Figure 3.13: Input admittance of the segmented transducer ring with equivalent sphere and finite cylinder radiation impedance.

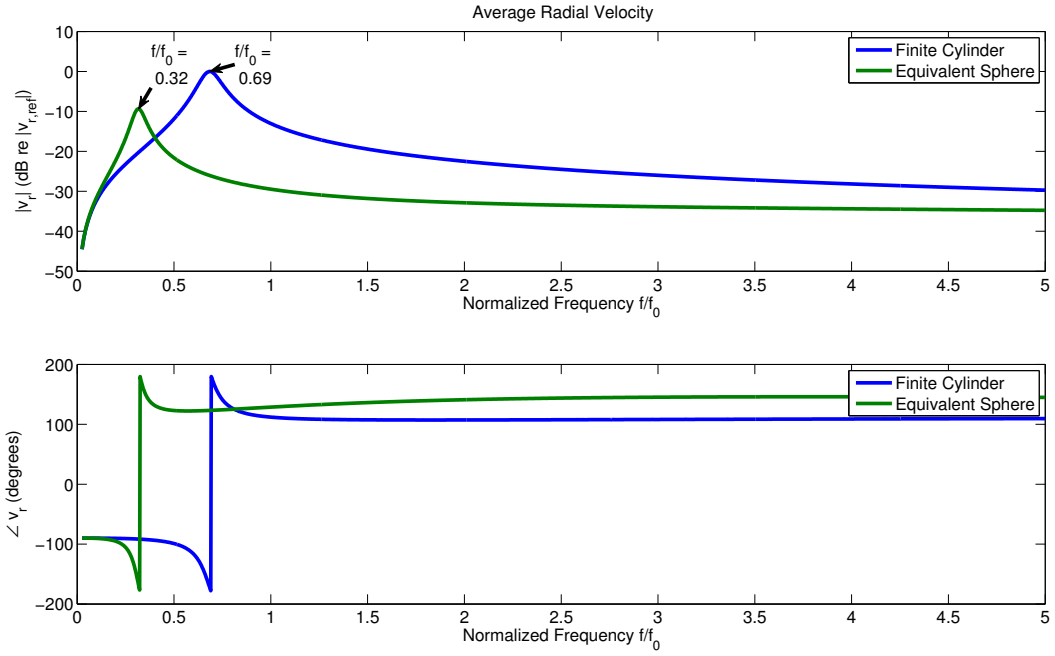

Figure 3.14: Average radial velocity of the segmented transducer ring with equivalent sphere and finite cylinder radiation impedance.

3.3.3 Internal Volume Effects

In underwater applications, the inner volume of cylindrical transducers is often filled with oil to prevent the transducer from collapsing under ambient water pressure when it is submerged. This internal volume can drastically alter the performance of the ring and must be considered to ensure accurate transducer performance predictions. Because the volume impedes the radial motion of each infinitesimal ring element, it should be included in the existing model as a mechanical impedance, denoted Z_{vol}, in series with the other mechanical elements of the ring, as shown in Fig. 3.9. The mechanical impedance of the internal volume is modeled as a lumped capacitance in Section 3.3.3.1

and as a distributed parameter system in Section 3.3.3.2.

3.3.3.1 Lumped Parameter Internal Volume

Suppose the ring is filled with a liquid of volume V and bulk modulus $B = \rho_{\text{vol}} c_{\text{vol}}^2$, where ρ_{vol} and c_{vol} are the density and sound speed of the internal volume respectively. As the ring radially expands and contracts, the equilibrium internal volume $V_0 = \pi a^2 h$ will change by an amount δV. A pressure P_{int} will be exerted by the volume on the ring that is proportional to the fractional change in volume, specifically

$$P_{\text{int}} = B \frac{\delta V}{V_0}. \tag{3.46}$$

When the radius of the ring is displaced by an amount ξ, the total volume is given by

$$V = \pi(a + \xi)^2 h = \pi a^2 (1 + S_1)^2 h \tag{3.47}$$

where $S_1 = \xi / a$ as before. The right-hand side of Eq. (3.47) may be expanded and approximated for small strain S_1 to obtain

$$V \approx \pi a^2 (1 + 2S_1) H = \pi a^2 h + 2\pi a^2 h S_1. \tag{3.48}$$

Since the total volume V is given by $V = V_0 + \delta V$, it can be seen from Eq. (3.48) that $\delta V \approx 2\pi a^2 h S_1$. Using Eq. (3.46), the internal pressure is given by $P_{\text{int}} \approx 2BS_1$.

The radial force resulting from pressure P_{int} applied over an area $2\pi ah$ is $F_{\text{vol}} = 4\pi BahS_1$. In terms of radial displacement $\xi = S_1 a$, the force may be

written as

$$F_{\text{vol}} = 4\pi Bh\xi. \tag{3.49}$$

This force due to the internal volume can be added to the total radial force F_r^{total} on the ring:

$$F_{\text{r}}^{\text{total}} = \frac{2\pi th}{s_{11}^E a}\xi - \frac{2\pi hd_{31}}{s_{11}^E}V + 4\pi Bh\xi \tag{3.50}$$

The radial equation of motion becomes

$$M\ddot{\xi} = F_0 - F_{\text{r}}^{\text{total}} = F_0 - \left(\frac{2\pi th}{s_{11}^E a} + 4\pi Bh\right)\xi - \left(\frac{2\pi hd_{31}}{s_{11}^E}\right)V, \tag{3.51}$$

The stiffness due to the internal volume can be defined as $K_{\text{vol}} = 4\pi Bh$. Like the filament winding stiffness, this stiffness can be added in series to the total mechanical stiffness of the ring and the analysis shown in Sections 3.1.3 and 3.1.4 and the circuit model shown in Fig. 3.4 hold. Alternatively, the circuit model in Fig. 3.9 can be used with

$$Z_{\text{vol}} = \frac{K_{\text{vol}}}{j\omega}. \tag{3.52}$$

3.3.3.2 Distributed Parameter Internal Volume

The results of Section 3.3.3.1 provide a low-frequency ($ka \ll 1$) approximation of the effects of the internal oil volume. However, if the wavelengths in the oil volume in the frequency band of interest are comparable in size to the dimensions of the transducer, it may be necessary to consider the effects of standing waves in the oil volume. This is the case for the material properties,

geometry, and frequency range given in Appendix A and considered here. Additionally, confirmation of this is given by an examination of the experimental results shown in Section 6 and the finite element modeling results shown in Section 4.2, in which standing wave behavior can be observed.

To determine the standing wave impedance, it is necessary to consider wave motion within the internal volume. A solution of the wave equation in cylindrical coordinates for a cylindrical cavity is given by Blackstock [12] as:

$$\Phi(r,\theta,z,t) = \begin{Bmatrix} J_m(k_r r) \\ N_m(k_r r) \end{Bmatrix} \begin{Bmatrix} \cos k_z z \\ \sin k_z z \end{Bmatrix} \begin{Bmatrix} \cos m\theta \\ \sin m\theta \end{Bmatrix} \begin{Bmatrix} \cos \omega t \\ \sin \omega t \end{Bmatrix}, \tag{3.53}$$

where Φ is the velocity potential; r, θ, and z are the radial, angular, and vertical coordinates, respectively; k_r and k_z are wave numbers and m is an integer; J_m and N_m are the ordinary Bessel and Neumann functions, respectively; ω is the angular frequency, t is time, and the curly braces indicate a linear combination of their contents.

The radial symmetry of the cylinder excitation dictates that $m = 0$ and allows the θ dependent factor to be dropped. Assuming the the volume is uniform in the z direction allows the z dependent factor to be dropped. The geometry under consideration contains the origin ($r = 0$) and thus the coefficient of the Neumann function $N_m(k_r r)$ must be zero, as this function is unbounded at $r = 0$. Moreover, the time-dependent factor may be dropped if its presence is implied. With the above in mind, the solution shown in Eq. 3.53 may be written as

$$\Phi(r) = AJ_0(kr), \tag{3.54}$$

where $k = k_r$, as wave motion only occurs in the r-direction, and A is an unknown coefficient.

The pressure p and velocity v are related to the velocity potential by the momentum equation and the definition of velocity potential. Specifically,

$$p = -j\omega\rho_0\Phi(r) = -j\omega\rho_0 A J_0(kr) \tag{3.55}$$

$$v = \frac{\partial}{\partial r}\phi(r) = kA J_0'(kr), \tag{3.56}$$

where time derivatives have been performed through multiplication of a factor of $j\omega$.

The specific acoustic impedance, or pressure-velocity ratio, at $r = a$ is given by

$$Z_{\text{vol,spac}} = \frac{p}{v} = \frac{-j\omega\rho c_0 J_0(ka)}{J_0'(ka)} = \frac{j\omega\rho c_0 J_0(ka)}{J_1(ka)} \tag{3.57}$$

where the relation $J_0'(x) = -J_1(x)$ has been used.

The corresponding mechanical impedance at the wall of the cylinder is given by multiplying the specific acoustic impedance by the lateral surface area of the cylinder, that is

$$Z_{\text{vol}} = 2\pi a H Z_{\text{vol,spac}} = \frac{j2\pi a h\omega\rho c_0 J_0(ka)}{J_1(ka)}. \tag{3.58}$$

For small ka, $J_0(ka) \approx 1$ and $J_1(ka) \approx ka/2$, thus the distributed parameter volume impedance given in Eq. 3.58 reduces to the lumped representation given in (3.52) as expected.

A comparison of the models for the internal volume impedance, given by Eqs. (3.52) and (3.58), for ring dimensions and internal volume properties

given in Appendix A is shown in Fig. 3.15. It can be seen that while the models are in good agreement at very low frequencies they quickly begin to diverge as the frequency is increased. The lumped compliance impedance is by definition purely capacitive, with a phase angle of −90 degrees. Its magnitude monotonically decreases with frequency and thus exhibits no resonant behavior. The standing wave model, by contrast, exhibits multiple resonances of the kind that appear in the finite-element and experimental data shown in later chapters.

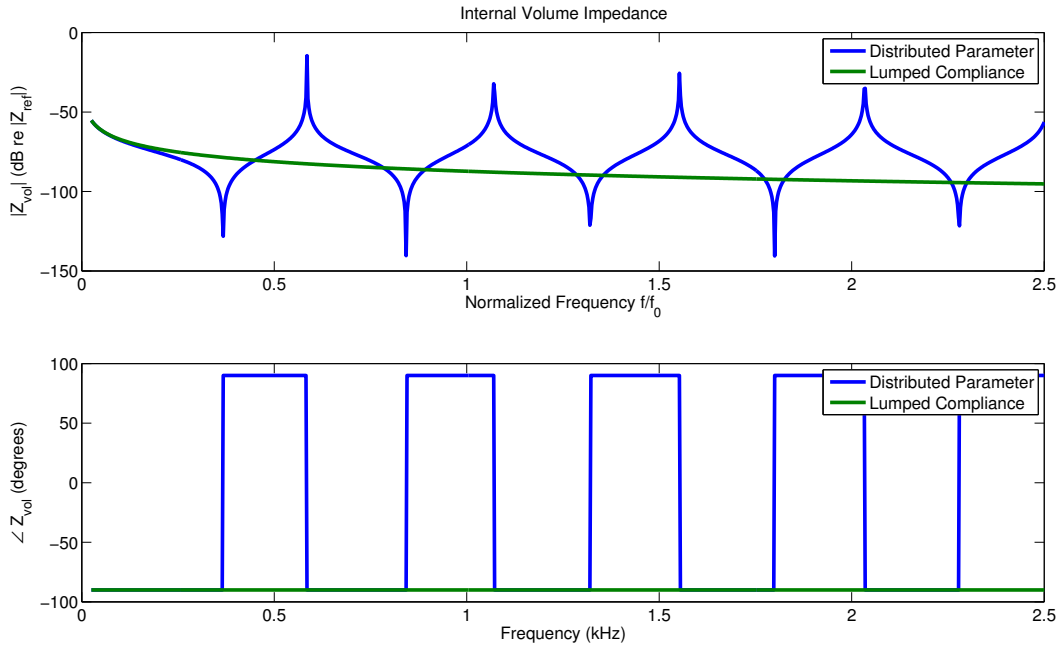

Figure 3.15: Impedance of distributed parameter and lumped compliance models for the internal oil volume.

These impedances have been used for Z_{vol} in the circuit model shown in Fig. 3.9 to produce the admittance and average radial velocity curves shown in

Figs. 3.16 and 3.17. The increase in the primary resonance for the distributed parameter model is not nearly as dramatic as suggested by the lumped parameter model. Additionally, it can be seen from the figures that standing waves in the internal oil volume create additional resonances and anti-resonances which can significantly affect the performance of the transducer. The location of these resonances as given by Model 1 with the distributed parameter impedance is in excellent agreement with that given by the finite element model discussed in Section 4.2.

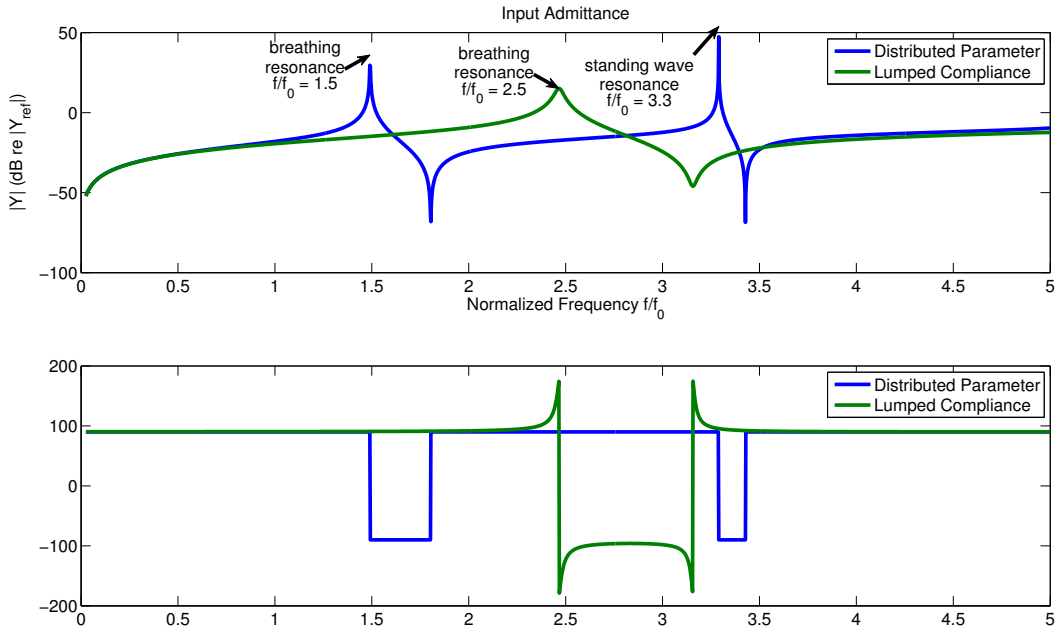

Figure 3.16: Input admittance of segmented transducer ring with internal oil volume, modeled as a lumped compliance and distributed parameter impedance

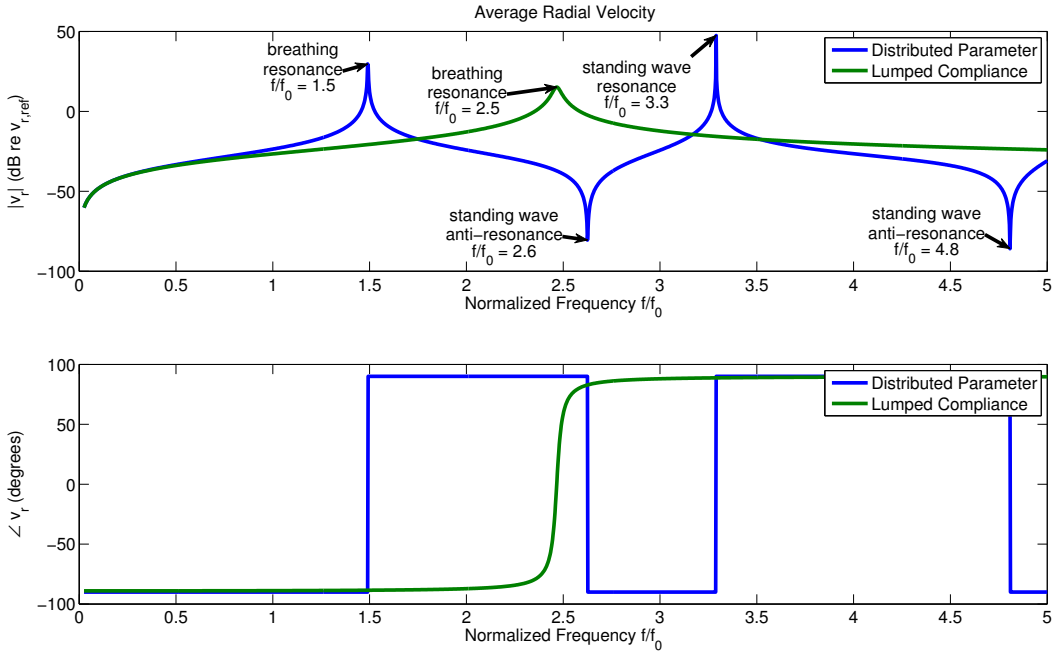

Figure 3.17: Average radial velocity of segmented transducer ring with internal oil volume, modeled as a lumped compliance and distributed parameter impedance

3.3.3.3 Effect of Impedance Along Axis of Cylindrical Ring Stack

To add durability and stability, a stack of ring transducers is typically contained in a structure of some kind that is topped with end-caps, secured with bolts, and filled with oil, as shown schematically in Fig. 3.18. This assembly introduces an impedance to motion along the vertical axis (referred to here as the z direction) of the cylindrical ring stack structure. Though this motion is orthogonal to motion along the radial, or r direction, it is coupled by the common pressure in the internal oil volume of the ring stack.

In order to account for the coupling of radial and vertical motion inside

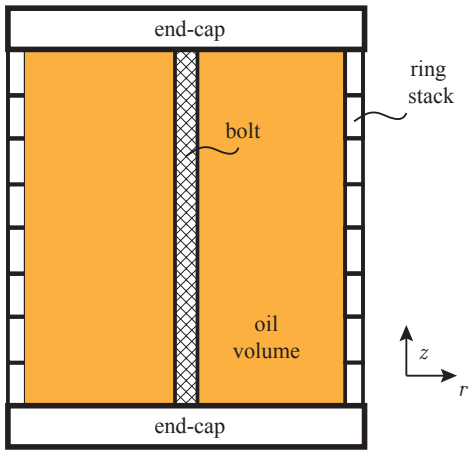

Figure 3.18: Cross section of cylindrical ring stack structure.

the assembly, the analogous situation of a ported loudspeaker cabinet is considered. The equivalent circuit model of the ported loudspeaker is shown in Fig. 3.19, as adapted from Leach [15]. The circuit element $Z_{\text{vol,ac}}$ represents the

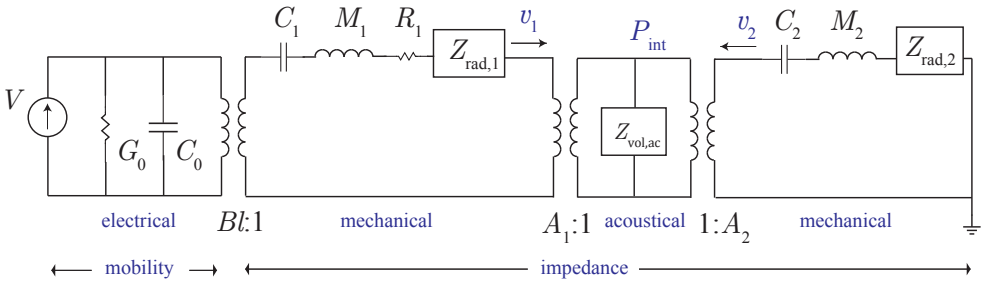

Figure 3.19: Circuit model for ported loudspeaker, adapted from Leach [15].

acoustic impedance of the internal volume of the speaker cabinet that couples the motion of the speaker (represented by current v_1) with the motion of the

slug of air inside the port (represented by current v_2). These mechanical flows are coupled into the acoustical domain with transformers that use the area of the piston face, A_1, and the cross-sectional area of the port, A_2, as turns ratios, transforming velocities into volume velocities and forces into pressure. The pressure P_{int} represents the common pressure inside the speaker cabinet.

Similarly, the ring stack assembly can be represented by the circuit model shown in Fig. 3.20. Here v_r represents the radial velocity of the ring and v_z represents the vertical velocity of the top cap of the boot assembly. Note that the transformer turns ratio connecting the radial mechanical domain to the acoustical domain is $N_{\text{R}}A_r$, representing the total radial surface area of the ring stack, with $A_r = 2\pi ah$ giving the radial surface area of one ring. The transformer turns ratio connecting the vertical mechanical domain to the acoustical domain is A_z, the surface area of the assembly cap, given by $A_z = \pi a_z^2$ for a circular cap. The volume velocity Q flowing through the internal volume is thus given by

$$Q = N_{\text{R}}A_r v_r + A_z v_z. \tag{3.59}$$

The impedance to motion along the axis of the cylinder is primarily due to the mass of the top cap M_z, the effective mechanical compliance of the bolts C_z, and the radiation impedance of the top cap $Z_{\text{rad},z}$ (which in this model has been approximated as that of a baffled piston).

The pressure inside of the assembly is the same as for a single ring and

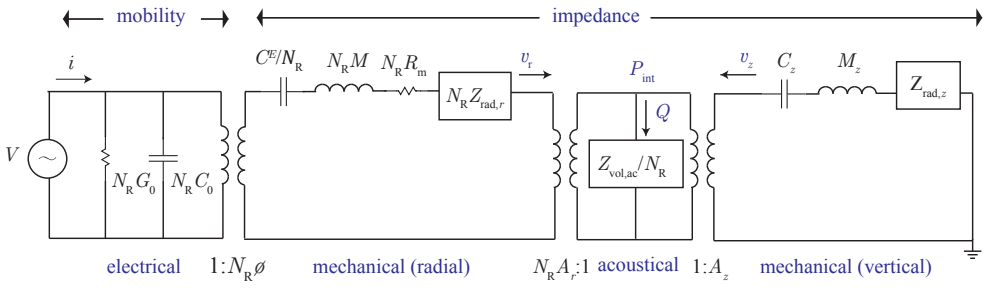

Figure 3.20: Circuit model for ring stack in assembly.

is given by Eq. 3.46. The change in volume δV can be written in terms of the integral of a time-harmonic volume velocity Q flowing through the internal volume, that is, $\delta V = 1/(j\omega)Q$. The acoustical impedance of the internal volume can then be defined as

$$Z_{\text{vol,ac}} = \frac{P_{\text{int}}}{Q} = \frac{1}{j\omega}\frac{B}{V_0} = \frac{1}{j\omega}\frac{1}{C_{\text{vol,ac}}},$$

where $C_{\text{vol,ac}} = V_0/B$ is the effective compliance of the internal volume.

The acoustic impedance can also be defined in terms of more complicated functions to account for standing waves inside the internal volume, as described in Section 3.3.3.2. Note that Eqs. (3.57) and (3.58) must be appropriately transformed by the radial area of the cylinder column in order to be used as an acoustic impedance.

This circuit model can be simplified by combining the elements into block impedances and moving them across transformers. To this end the following are defined:

- The total radial mechanical impedance for a one ring stack:

$$Z_r = \frac{1}{j\omega C^E} + M + R_{\mathrm{m}} + Z_{\mathrm{rad},r}. \tag{3.60}$$

- The total vertical mechanical impedance:

$$Z_z = \frac{1}{j\omega C_z} + M_z + Z_{\mathrm{rad},z}. \tag{3.61}$$

- The (blocked) electrical impedance:

$$Z_{\mathrm{e}} = \frac{1}{G_0 + j\omega C_0}. \tag{3.62}$$

These values can be modified to account for a stack of multiple rings through multiplication or division by the number of rings N_{R} as appropriate. Figure 3.21 shows the equivalent circuit for a stack of N_{R} rings in terms of these impedances, with the additional step of moving Z_z and $Z_{\mathrm{vol,ac}}/N_{\mathrm{R}}$ across the transformers into the radial mechanical domain. Note that moving $Z_{\mathrm{vol,ac}}/N_{\mathrm{R}}$ from the acoustical domain into the radial mechanical domain involves multiplication by the transformer turns ratio $(N_{\mathrm{R}}A_r)^2$, which yields $N_{\mathrm{R}}A_r^2 Z_{\mathrm{vol,ac}} = N_{\mathrm{R}}Z_{\mathrm{vol}}$, where Z_{vol} is the (radial) mechanical impedance of the internal volume as given by Eqs. (3.52) or (3.58).

TO further simplify the circuit, all impedances can be moved into the electrical domain to produce the (electrical) impedances $Z_0 = Z_{\mathrm{e}}/N_{\mathrm{R}}$, $Z_1 = N_{\mathrm{R}}Z_r$, $Z_2 = N_{\mathrm{R}}Z_{\mathrm{vol}}$, $Z_3 = (N_{\mathrm{R}}A_r/A_z)^2 Z_z$. From the circuit model shown in Fig. 3.22, it can be seen that the input impedance of the circuit is

$$Z_{\mathrm{in}} = Z_0 || \left(Z_1 + Z_2 || Z_3\right), \tag{3.63}$$

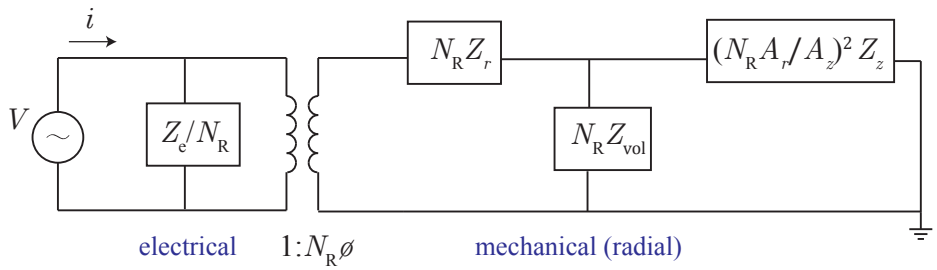

Figure 3.21: Reduced circuit model for ring stack in assembly.

where the || operator indicates that impedances Z_2 and Z_3 are wired in parallel. The total electrical impedance due to mechanical effects is given by

$$Z_{\mathrm{M}} = Z_1 + Z_2||Z_3 = \frac{1}{N_{\mathrm{R}}\phi^2}\left(Z_r + \frac{\left(\frac{A_r}{A_z}\right)^2 Z_z Z_{\mathrm{vol}}}{\frac{Z_{\mathrm{vol}}}{N_{\mathrm{R}}} + \left(\frac{A_r}{A_z}\right)^2 Z_z}\right). \tag{3.64}$$

As N_{R} becomes increasingly large, it can be seen from Eq. (3.64) that Z_{M} approaches $\frac{1}{N_{\mathrm{R}}\phi^2}(Z_r + Z_{\mathrm{vol}}) = Z_1 + Z_2$ as expected. In other words, the axial motion and associated impedances become negligible if there are a large number of rings in the stack.

Fig. 3.23, 3.24, and 3.25 show magnitude and phase plots for the electrical admittance, radial and vertical velocities, and transmit voltage response of an eight ring stack with internal volume (modeled as a lumped compliance), with and without consideration of the effects of axial motion. An additional low-frequency resonance is observed in the response when axial motion is considered. This resonance is due to the interaction of the mass of the end-cap and the stiffness of the bolt. Additionally, the primary resonance (associated

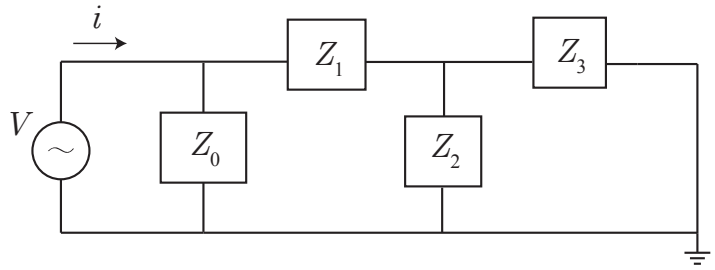

Figure 3.22: Reduced circuit model in electric domain.

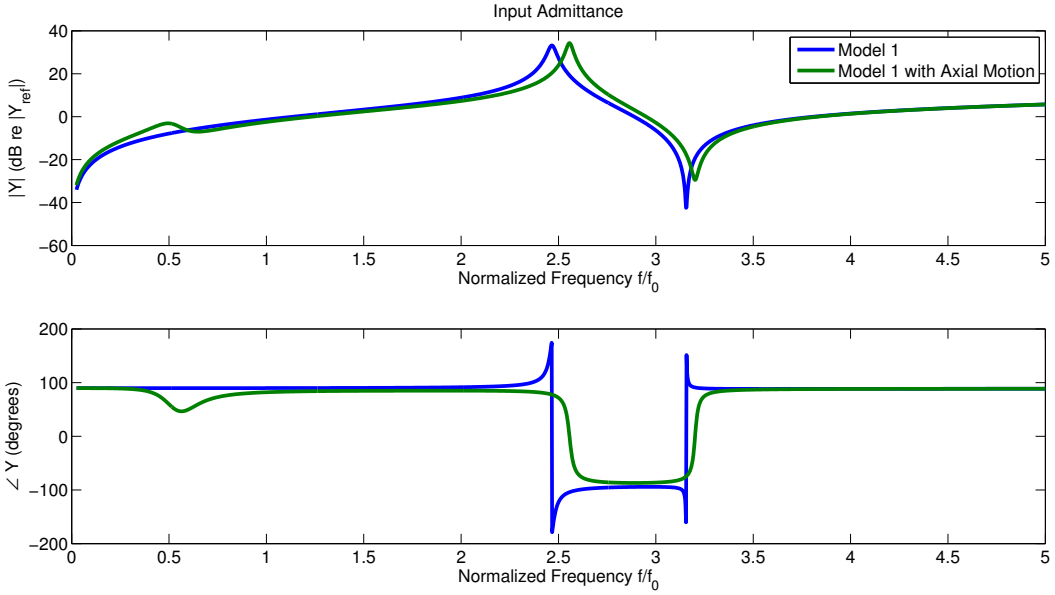

Figure 3.23: Input admittance of stack of eight transducer rings, with and without axial motion effects.

with the breathing mode of the ring) occurs at a slightly higher frequency, indicating that the assembly adds stiffness to the system. The radial and vertical velocities v_r and v_z are plotted in Fig. 3.24, from which it can be seen that the vertical velocity of the end-cap v_z is significantly lower in magnitude than

the radial velocity of the cylinder walls. Thus the mass in the surrounding medium displaced by the motion of the end-cap does not contribute significantly to the far-field pressure field created by the transducer. The transmit voltage response (TVR) for the ring stack plotted in Fig. 3.25 is calculated using Eq. (2.34) and (2.35) with volume velocity Q given by Eq. (3.59). It should

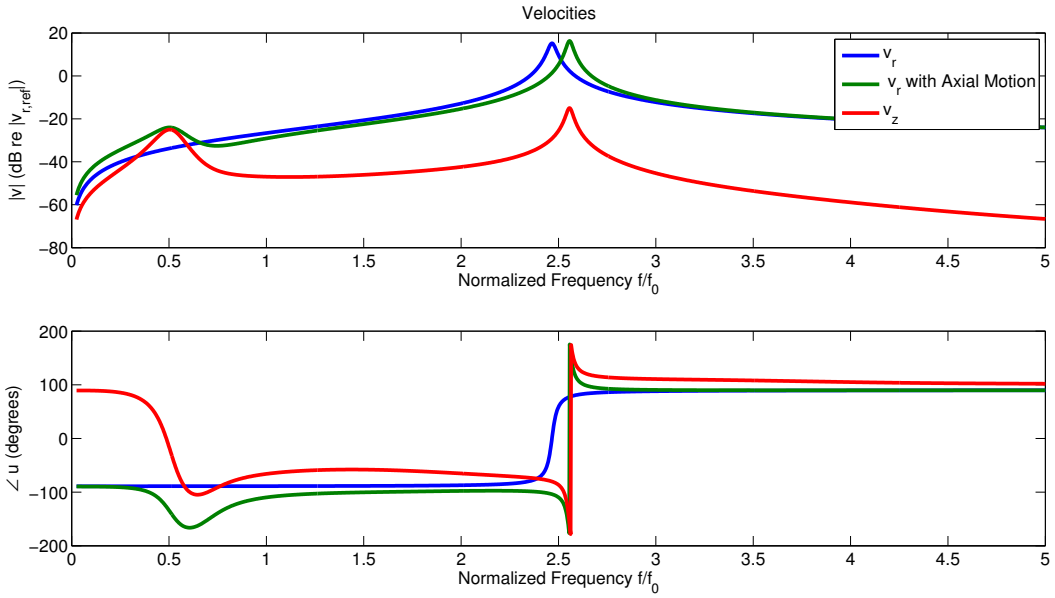

Figure 3.24: Radial and vertical velocities of stack of eight transducer rings,.

be noted that since the far-field pressure is found using Eq. (2.35), which is an approximation of the transducer as a simple spherical source ($ka \ll 1$ and $kh \ll 1$), it becomes less valid as the height of the cylindrical structure is increased as more transducer rings are added to the stack. For a tall cylinder (large N_{R}), a more accurate model would calculate the far-field pressure field resulting from a radiating cylinder. Additionally, an additional approximation has been made in the model by assuming that the internal pressure P_{int} is

everywhere the same on the end-cap. A more realistic model would allow this pressure field to vary along the radial direction due to the presence of standing waves within the cylindrical volume.

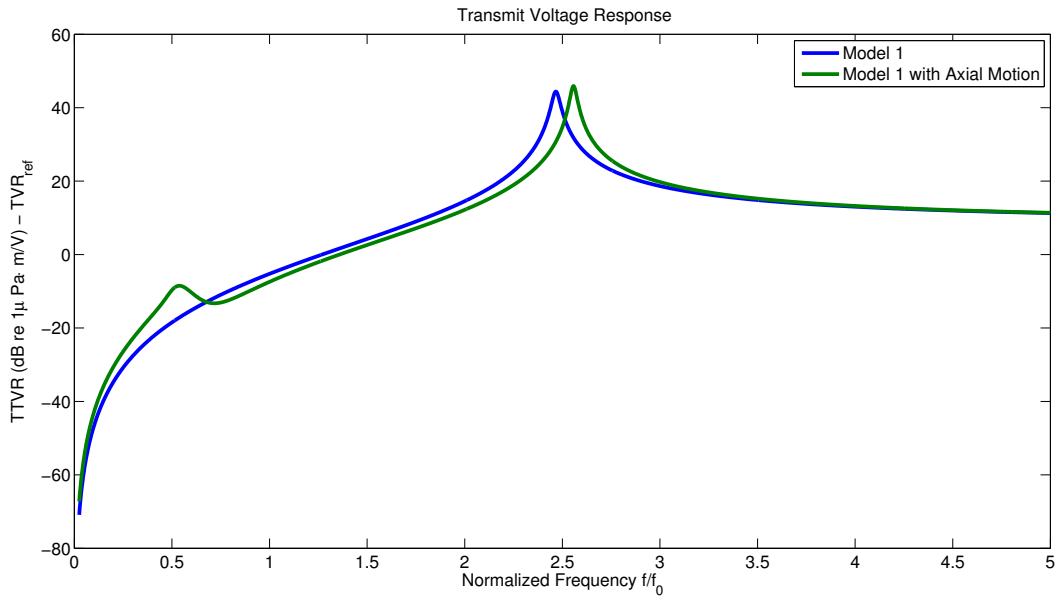

Figure 3.25: Transmit voltage response of stack of eight transducer rings, with and without axial motion effects.

3.4 Conclusions

A one-degree-of-freedom model for a piezoelectric 31-mode segmented ring transducer has been presented in this chapter. This type of model is commonly used and provides a relatively simple means to analyze the performance of the transducer. However, results from the finite-element modeling and experimental data, shown in Chapter 4 and Chapter 6 respectively, indicate that significant aspects of the transducer's performance are not captured by

this one-degree-of-freedom model. For this reason, a higher-degree-of-freedom model is developed in Chapter 5.

Chapter 4

Finite Element Modeling

The models presented in Chapters 3 and 5 represent physical systems whose characteristics have been idealized as discrete elements, an approach known as lumped parameter modeling. In general, as the number of lumped parameters is increased (rendering the model more spatially distributed) the model becomes more accurate, as a large number of discrete elements will better approximate the continuum of properties that exists in the real system being modeled. The finite element method (FEM) is essentially a systematic discretization procedure that produces lumped element models with an arbitrary degree of discretization. The lumping algorithm can be automated and implemented by a computer, making a multi-dimensional model with a large number of degrees of freedom relatively easy to create. Because of this, FEM models often capture effects of physical behavior that are neglected by more basic lumped parameter models. However, because the differential equations governing the system being modeled must be solved for each element, running a simulation with an FEM model can be computationally costly. Commercial packages like COMSOL Multiphysics have made it easier to systematically run parametric studies for explorations of design space, though such studies may take a significant amount of time and computing power. For this reason, FEM

models are typically used in conjunction with simpler lumped parameter models when designing a transducer so that an ideal configuration may be rapidly converged upon.

This chapter presents two approaches to finite element modeling of the ring transducer system. Section 4.1 is a development of a one-dimensional finite element model of the mechanical domain of the ring transducer system. Section 4.2 presents three-dimensional FEM models of the transducer involving multiple domains, created with the commercial program COMSOL. This program makes it relatively easy to create complex models with complicated geometries and coupling between various physical domains. These models are used in Chapter 5 as a reference to compare the accuracy of the multi-degree-of-freedom lumped parameter model which is the primary interest of the research presented in this work. Due to concerns of the project sponsor, the results presented here have been normalized according to the scheme described in Appendix A.

For both FEM models presented in this chapter, the radial symmetry of the ring design is used to reduce the system to a representative unit cell, shown in Fig. 4.1. Because the driving voltage at each active element in the ring is applied in phase and the geometry of the ring is symmetrical, an equivalent model of the full segmented ring can be created from an adjacent active and inactive element pair on which zero normal displacement, zero rotation boundary conditions (referred to here in shorthand as roller boundary conditions) have been imposed at the lengthwise midpoint of each element. This unit cell

will exhibit all of the modes present in the full ring. The unit cell contains one active and one inactive element with length dimension (along the circumference of the ring) half that of their original lengths L_1 and L_2 respectively, that is, $l_1 = L_1/2$ and $l_2 = L_2/2$. For a ring with N elements (both active and inactive), this unit cell is repeated N times around the circumference of the ring and the angle θ that the unit cell subtends is given by $\theta = 2\pi/N$. This reduced model decreases computational time while producing identical solutions to a model with the same physical assumptions that considers all elements of the ring.

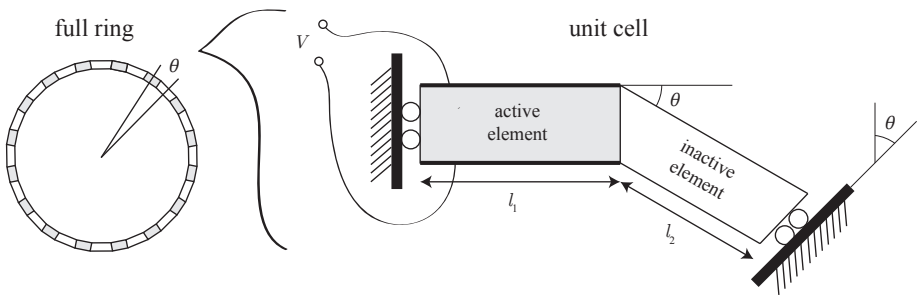

Figure 4.1: Unit cell of ring with roller boundary conditions.

4.1 One-Dimensional Finite Element Model

This section follows a procedure detailed in Chapter 8 of Meirovitch [16]. In this method systems are lumped into a finite number of continuous elements, the displacement at any point of which is expressed in terms of displacements at the element boundaries, or joints. Lagrange's equations of motion are written for each element in terms of these boundary displacements, and inertia

and stiffness matrices for each element are taken from these equations.

For an element in the form of a bar in bending subject to axial forces, as shown in Fig. 4.2, the inertia and stiffness matrices are given by Meirovitch as

$$[m] = \frac{mL}{420}\begin{bmatrix} 140 & 0 & 0 & 70 & 0 & 0 \\ 0 & 156 & 22L & 0 & 54 & -13L \\ 0 & 22L & 4L^2 & 0 & 13L & -3L^2 \\ 70 & 0 & 0 & 140 & 0 & 0 \\ 0 & 54 & 13L & 0 & 156 & -22L \\ 0 & -13L & -3L^2 & 0 & -22L & 4L^2 \end{bmatrix} \tag{4.1}$$

and

$$[k] = \frac{EI}{L^3}\begin{bmatrix} \left(\frac{L}{r}\right)^2 & 0 & 0 & -\left(\frac{L}{r}\right)^2 & 0 & 0 \\ 0 & 12 & 6L & 0 & -12 & 6L \\ 0 & 6L & 4L^2 & 0 & -6L & 2L^2 \\ -\left(\frac{L}{r}\right)^2 & 0 & 0 & \left(\frac{L}{r}\right)^2 & 0 & 0 \\ 0 & -12 & -6L & 0 & 12 & -6L \\ 0 & 6L & 2L^2 & 0 & -6L & 4L^2 \end{bmatrix} \tag{4.2}$$

where L is the element length, m is the mass per unit length, E[1] is the Young's modulus, I is the area moment of inertia, and $r = \sqrt{\frac{I}{A}}$ is the radius of gyration of the cross-sectional area.

The motion at the joints can be represented as generalized displacements—two linear displacements along each of the local x-y coordinate axes and one rotation about the axis perpendicular to the element. With this understanding, the generalized displacements are referred to here simply as displacements and written as u_1, u_2, u_3, u_4, u_5, and u_6.

[1]To maintain consistency with our references, E is used here for the Young's modulus rather than Y. Note that here E does not represent electric field as in Chapters 2 and 3.

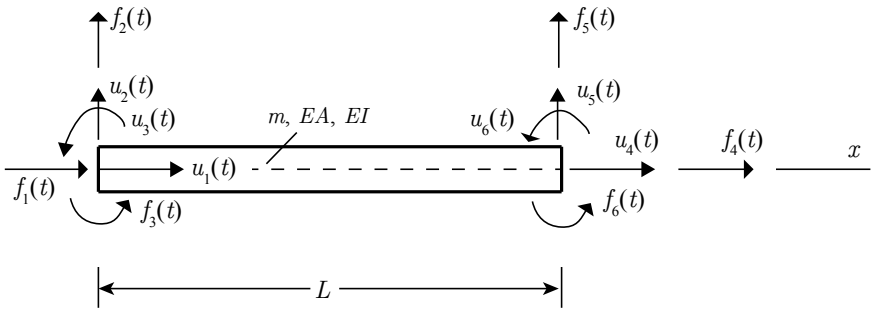

Figure 4.2: Element of bending beam subject to axial forces, adapted from Meirovitch. [16]

If the local coordinate system of the bar element is rotated by a clockwise angle θ with respect to some global $\bar{x}$-$\bar{y}$ coordinate axes, as in Fig. 4.3, the two coordinate systems may be related through a direction cosine transformation matrix $[l]$ as

$$\begin{Bmatrix} x \\ y \\ z \end{Bmatrix} = [l] \begin{Bmatrix} \bar{x} \\ \bar{y} \\ \bar{z} \end{Bmatrix}, \tag{4.3}$$

with

$$[l] = \begin{bmatrix} \cos\theta & \sin\theta & 0 \\ -\sin\theta & \cos\theta & 0 \\ 0 & 0 & 1 \end{bmatrix}. \tag{4.4}$$

If the six displacements are written in column matrices $\{u\}$ and $\{\bar{u}\}$, in the local and global coordinate system respectively, they may be related through a transformation matrix $[L]$ by

$$\{u\} = [L] \{\bar{u}\}, \tag{4.5}$$

where

$$[L] = \begin{bmatrix} [l] & [0] \\ [0] & [l] \end{bmatrix}. \tag{4.6}$$

The mass and stiffness matrices for the element in terms of the global coor-

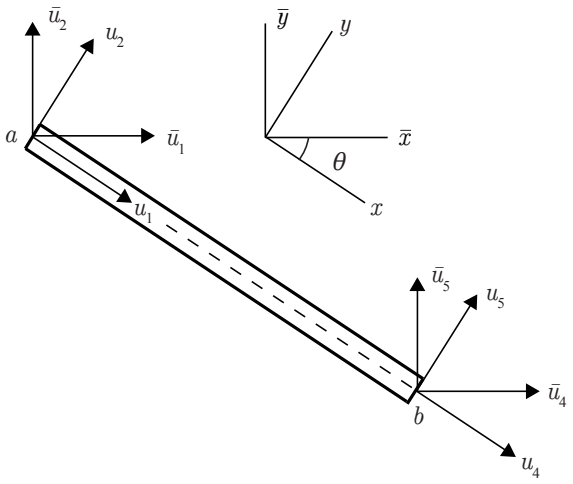

Figure 4.3: Local and global coordinate system, adapted from Meirovitch. [16]

dinate system can then be written as

$$[\bar{m}] = [L]^{\mathrm{T}}[m][L], \tag{4.7}$$

and

$$[\bar{k}] = [L]^{\mathrm{T}}[k][L], \tag{4.8}$$

respectively, where superscript T indicates a matrix transpose.

When extending these results to the entire structure it is useful to introduce the column matrix $\{\bar{U}\}$, a vector consisting of the joint displacements (with respect to the global coordinate system) of the discretized structure. This vector represents a set of generalized coordinates for the complete sys-

tem. The joint displacements of the sth element can be written as

$$\{\bar{u}\}_s = [A]_s\{\bar{U}\}, \tag{4.9}$$

where $[A]_s$ is a matrix of appropriate dimensions whose rows contain all zeros, except for one diagonal consisting of all ones designating the appropriate joint displacements for element s. Finally, the mass and stiffness matrix for the entire structure of p elements can be written as

$$[\bar{M}] = \sum_{s=1}^{p} [A]_s^T [\bar{m}]_s [A]_s \tag{4.10}$$

and

$$[\bar{K}] = \sum_{s=1}^{p} [A]_s^T [\bar{k}]_s [A]_s, \tag{4.11}$$

respectively.

Boundary conditions are applied by eliminating the entries representing restricted displacements from the generalized coordinate vector and removing corresponding rows and columns from the matrices $[\bar{M}]$ and $[\bar{K}]$.

The first finite element approximation of the ring section shown in Fig. 4.1 that is considered here is a purely mechanical component assumed to be composed of the bending bar elements shown in Fig. 4.2. The simplest case reticulates the system into two elements, one each for the active and inactive elements, as depicted in Fig. 4.4. Vectors, matrices, and entries for each of these elements are subscripted by 1 and 2, representing the active and inactive elements respectively. Three displacements (axial, transverse, and angular) for each of the three joints in the system yields nine degrees of freedom for the

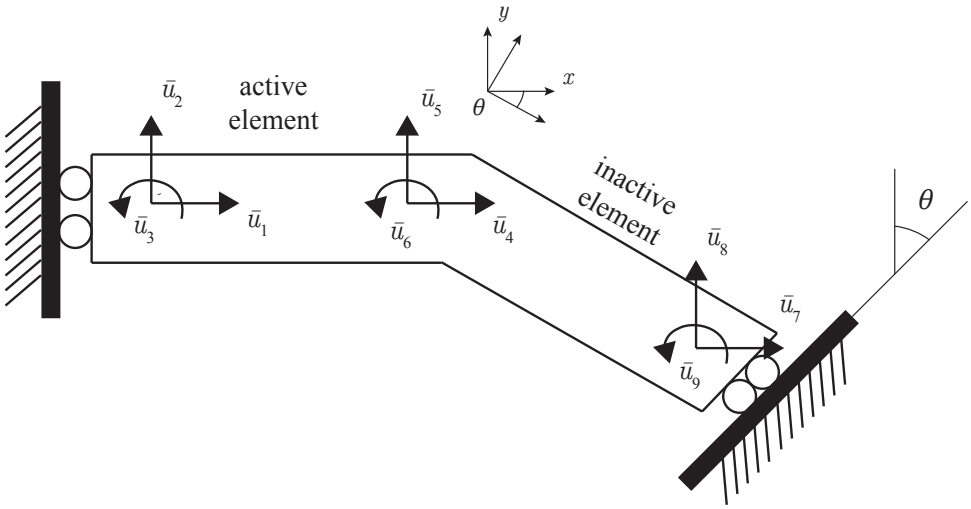

Figure 4.4: Reduced ring model as composed of two bending bar elements.

total system. These can be written in terms of the global coordinate system and placed in a generalized coordinate column matrix

$$\{\bar{U}\} = \begin{Bmatrix} \bar{u}_1 \\ \bar{u}_2 \\ \bar{u}_3 \\ \bar{u}_4 \\ \bar{u}_5 \\ \bar{u}_6 \\ \bar{u}_7 \\ \bar{u}_8 \\ \bar{u}_9 \end{Bmatrix}. \tag{4.12}$$

The displacement coordinates for elements 1 and 2 can be selected from $\{\bar{U}\}$

using $[A]$ matrices in the following manner:

$$\left\{\bar{u}\right\}_1 = \begin{Bmatrix} \bar{u}_1 \\ \bar{u}_2 \\ \bar{u}_3 \\ \bar{u}_4 \\ \bar{u}_5 \\ \bar{u}_6 \end{Bmatrix} = \begin{bmatrix} 1 & 0 & 0 & 0 & 0 & 0 & 0 & 0 & 0 \\ 0 & 1 & 0 & 0 & 0 & 0 & 0 & 0 & 0 \\ 0 & 0 & 1 & 0 & 0 & 0 & 0 & 0 & 0 \\ 0 & 0 & 0 & 1 & 0 & 0 & 0 & 0 & 0 \\ 0 & 0 & 0 & 0 & 1 & 0 & 0 & 0 & 0 \\ 0 & 0 & 0 & 0 & 0 & 1 & 0 & 0 & 0 \end{bmatrix} \begin{Bmatrix} \bar{u}_1 \\ \bar{u}_2 \\ \bar{u}_3 \\ \bar{u}_4 \\ \bar{u}_5 \\ \bar{u}_6 \\ \bar{u}_7 \\ \bar{u}_8 \\ \bar{u}_9 \end{Bmatrix} = \left[A\right]_1 \left\{\bar{U}\right\} \quad (4.13)$$

and

$$\left\{\bar{u}\right\}_2 = \begin{Bmatrix} \bar{u}_4 \\ \bar{u}_5 \\ \bar{u}_6 \\ \bar{u}_7 \\ \bar{u}_8 \\ \bar{u}_9 \end{Bmatrix} = \begin{bmatrix} 0 & 0 & 0 & 1 & 0 & 0 & 0 & 0 & 0 \\ 0 & 0 & 0 & 0 & 1 & 0 & 0 & 0 & 0 \\ 0 & 0 & 0 & 0 & 0 & 1 & 0 & 0 & 0 \\ 0 & 0 & 0 & 0 & 0 & 0 & 1 & 0 & 0 \\ 0 & 0 & 0 & 0 & 0 & 0 & 0 & 1 & 0 \\ 0 & 0 & 0 & 0 & 0 & 0 & 0 & 0 & 1 \end{bmatrix} \begin{Bmatrix} \bar{u}_1 \\ \bar{u}_2 \\ \bar{u}_3 \\ \bar{u}_4 \\ \bar{u}_5 \\ \bar{u}_6 \\ \bar{u}_7 \\ \bar{u}_8 \\ \bar{u}_9 \end{Bmatrix} = \left[A\right]_2 \left\{\bar{U}\right\}. \quad (4.14)$$

For element 1, displacements are the same in the local and global coordinate system, that is $\left\{u\right\}_1 = \left\{\bar{u}\right\}_1$. Alternatively, Eqs. (4.4) through (4.6) may be used with $\theta_1 = 0$.

For element 2, local and global coordinate systems and displacements are related through Eqs. (4.4) through (4.6), with $\theta_2 = 2\pi/N$ for a ring with N active elements. The mass and stiffness matrices for the entire system are thus

$$[\bar{M}] = \sum_{s=1}^{2} [A]_s^T [L]_s^T [m]_s [L]_s [A]_s \quad (4.15)$$

and

$$[\bar{K}] = \sum_{s=1}^{2} [A]_s^T [L]_s^T [k]_s [L]_s [A]_s, \tag{4.16}$$

respectively, where $[m]_s$ and $[k]_s$ are given by Eqs. (4.1) and (4.2), with m, L, E, I, and r given by the properties of the appropriate element.

It is now appropriate to consider the boundary conditions placed on the elements. For the case of an entirely free beam, the equations of motion for the system are given in matrix form as

$$[\bar{M}] \left\{ \ddot{\bar{U}} \right\} + [\bar{K}] \left\{ \bar{U} \right\} = \left\{ 0 \right\}. \tag{4.17}$$

A roller boundary condition does not allow for axial or angle displacement at the joints where it is imposed. For the system under consideration here this means that $u_1 = u_3 = u_7 = u_9 = 0$. The roller boundary condition can be applied by removing these displacements from $\left\{ \bar{U} \right\}$, and removing the rows and columns 1, 3, 7, and 9 from the total mass and stiffness matrices given in Eqs. (4.15) and (4.16).

By assuming time-harmonic displacements with angular frequency ω, Eq. (4.17) can written as the eigenvalue equation

$$\left[[\bar{K}] - \omega^2 [\bar{M}] \right] \left\{ \bar{U} \right\} = \left\{ 0 \right\}, \tag{4.18}$$

whose solution will be a set of eigenvalues, ω_r^2, and eigenvectors, $\left\{ \bar{u}^{(r)} \right\}$, one for each degree of freedom in the system. These eigenvalues and eigenvectors will determine the natural frequencies and natural modes of the system.

After applying the roller boundary conditions, the system has five degrees of freedom and thus five resonant modes. Only the first two are in the frequency range of interest for the research presented here. The first two resonance frequencies represent the breathing and bending modes of the ring, which are shown schematically in Figs. 4.5 and 4.6, respectively.

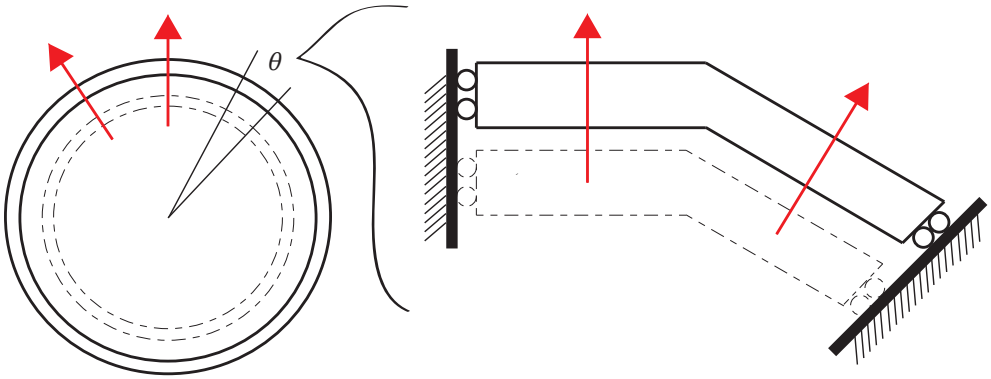

Figure 4.5: Breathing mode of ring.

The above procedure can be generalized for reticulation of the system into p elements. The first five normalized resonance frequencies for various values of p, using the above procedure and the material properties and dimensions given in Appendix A, are given in Table 4.1. Increasing the number of elements increases the accuracy of the finite-element model, though it can be seen from the table that increasing the number of elements has the most dramatic effect on the higher frequencies and that the resonance frequencies of interest (the 1st and 2nd) are adequately captured by reticulating the sys-

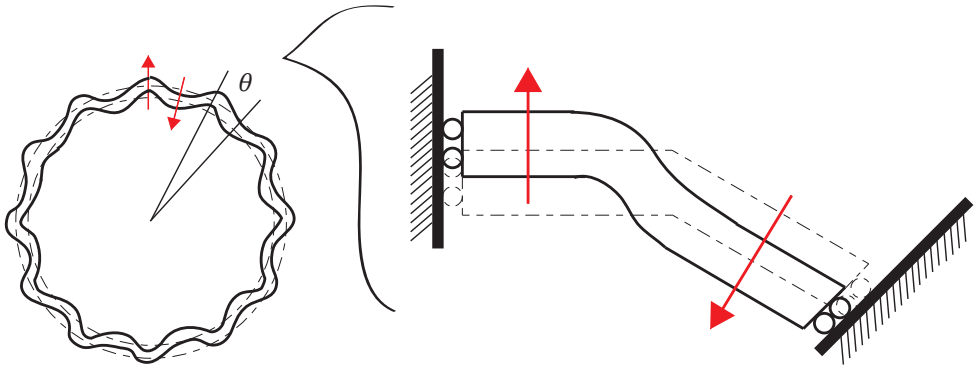

Figure 4.6: Bending mode of ring.

tem into only two elements. The MATLAB script in Appendix C presents the finite element modeling code used determine these resonance frequencies.

Table 4.1: Normalized Resonance Frequencies f/f_0

Resonance	p = 2	p = 4	p = 10	p = 20
1st	0.993	0.993	0.992	0.992
2nd	4.486	4.463	4.461	4.461
3rd	14.054	13.696	13.588	13.584
4th	39.225	20.756	19.267	19.063
5th	63.313	33.756	33.487	33.405

4.2 COMSOL Finite Element Models

COMSOL Multiphysics is a commercially available finite element modeling program in which structures with complex geometries can be rendered and made subject to the physics of various coupled domains, including electric, piezoelectric, elastic, and acoustical. In principal, COMSOL applies the same method described in Section 4.1: a system is reticulated into a discrete number of elements, boundary and forcing conditions are applied, and constitutive differential equations given by the physics of the domain are solved. COMSOL, however, makes it easy to implement complicated models that would be difficult to create and solve manually. Models can be created in 2D or 3D and their solutions can be displayed graphically. For this reason COMSOL is a useful tool for gaining insight into complicated systems in which traditional lumped parameter models do not fully capture all phenomena. It enables simple implementation for modeling more general geometries and coupled physics than is possible in custom FEM codes like the one described in the preceding section. FEM models can be computationally expensive, so it is preferable to use no more elements than are required to meet the convergence criteria needed for a particular application.

4.2.1 Reduced Model Rendering

The work presented in this section results from a 3D COMSOL rendering of the reduced model of the segmented ring shown in Fig. 4.1. The symmetry of the full ring is exploited to reduce the full ring geometry to a

slice containing one joint where the active and inactive staves meet. Applying roller boundary conditions halfway along each element enforces symmetry such that the reduced model is equivalent to the full segmented ring model. In this way the model is simplified and the computational power and time required to run simulations is drastically reduced. It should be noted, however, that some performance metrics, such as input admittance and impedance, need to be properly scaled by the number of unit cells when using the reduced model. Figure. 4.7 shows a COMSOL rendering of the unit cell, meshed into discrete finite elements. In this figure and all subsequent figures of the unit cell, the active element is on the left and the inactive element is on the right.

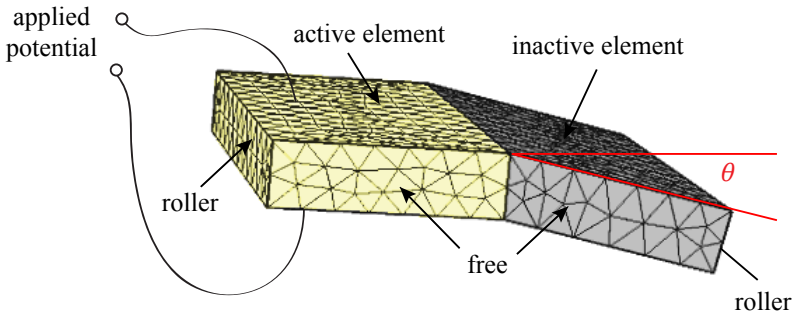

Figure 4.7: Meshed COMSOL model of unit cell of ring.

The active and inactive elements have dimensions and material properties given by Appendix A, with the exception of their length, which is half the full element length in each case, for reasons of symmetry as discussed above. COMSOL has a set of predefined physics that can be applied to a domain within a model in order to subject it to the appropriate constitutive

equations. The domain of the active element stave is given "Piezoelectric Material" physics while the domain of the inactive element is given "Linear Elastic Material" physics. Additionally, the active element is subject to an electric potential across its inner and outer faces. The remaining faces of the staves are given a mechanically free boundary condition, corresponding to the unloaded case that most closely resembles the response of the transducer in air.

The effects of an internal oil volume and radiation impedance are accounted for in the model by adding acoustical domains that interface with the elements. The symmetry of the model can be invoked again to reduce the full system to the wedge shown in Fig. 4.8. This is accomplished by adding acoustically hard boundary conditions on the walls of the wedge. The top and bottom of the wedge (with faces perpendicular to the x_2 direction) are also given acoustically hard boundary conditions, making the oil and water domains in the model effectively infinite in extant along the direction of the transducer axis. This approximation was necessary for the sake of computational simplicity, though the deviation from the actual conditions of the real system must be noted when considering results of the model. A correction for the radiation impedance of the ring due to the infinite water domain is presented in Appendix D. Additionally, a cylindrical wave radiation condition is imposed at the far end of the wedge. The cylindrical wave boundary condition is based on a series expansion of the outgoing wave in cylindrical coordinates. It effectively allows the outgoing wave to leave the modeling do-

main with minimal reflections, simulating free-field conditions in which waves propagate out indefinitely. Both oil and water domains are given "Pressure Acoustics" physics and an "Acoustic-Structure Boundary" is applied at the interface with the elements.

The meshing must be dense enough to provide solutions with adequate resolution but not so dense as to be computationally prohibitive. A general rule of thumb is to mesh the domain such that there are ten elements per wavelength, that is let

$$L_{\mathrm{e}} = \frac{\lambda}{10} = \frac{c_0}{10f}, \tag{4.19}$$

where L_{e} is the element length, is the wavelength in the material or medium, c_0 is the sound speed in the medium, and f is the frequency of interest. It can be seen from Eq. (4.19) that a higher frequency simulation will require a smaller element length. For frequency-based simulations involving a range of frequencies, the element length can be based on the highest frequency involved or, if necessary, scaled dynamically as the frequency changes. Additionally, since the wavelength is dependent on the medium that the wave propagates in, domains should be meshed separately in order to optimize accuracy and computation time. The models with acoustical domains were meshed separately here, as shown in Fig. 4.9.

All simulations presented in this chapter use material properties and dimensions given in Appendix A. Additionally, default settings for COMSOL version 4.3a were used, except for the meshing, which was done to satisfy Eq. (4.19) for the highest frequency involved.

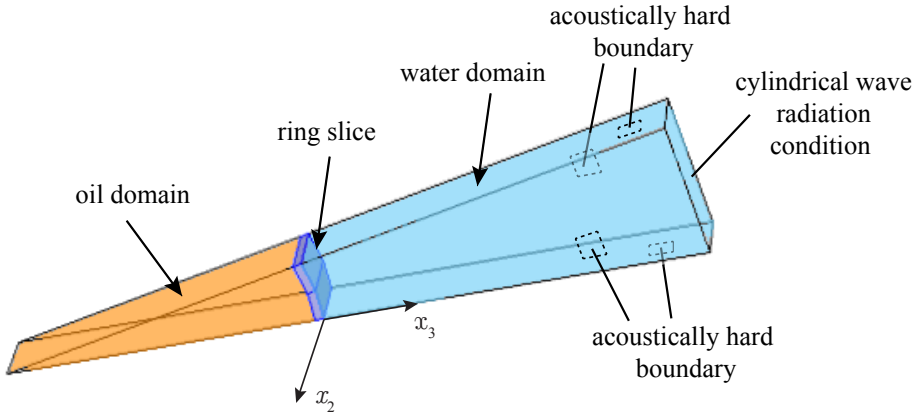

Figure 4.8: Reduced ring model with acoustical domains.

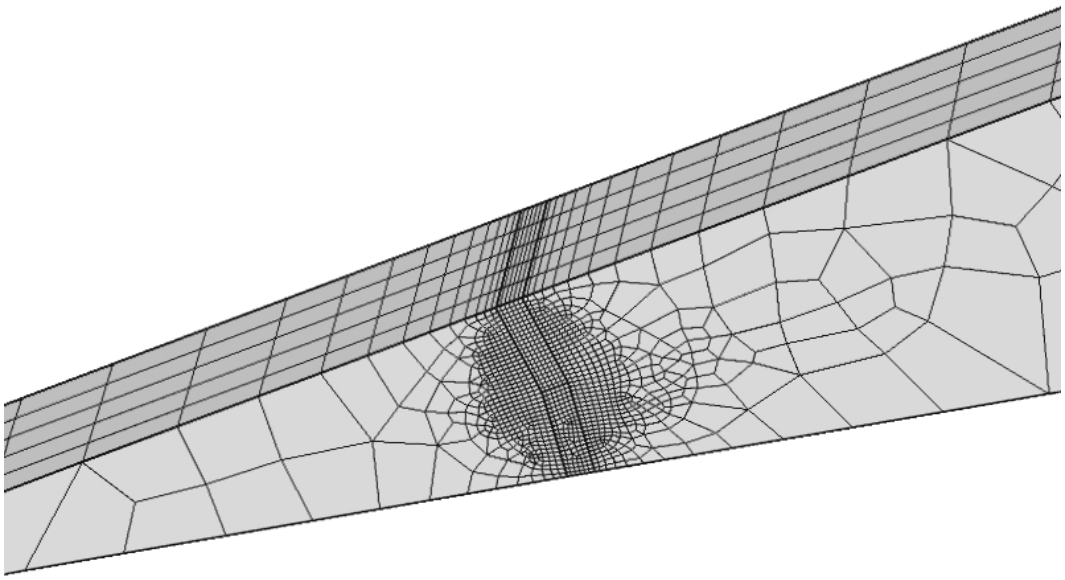

Figure 4.9: Meshed model with acoustical domains.

4.2.2 Finite Element Model Solutions

Finite element models created in COMSOL can produce a wide variety of information that can be used to measure the performance of a device. For the models presented here, the metrics of interest are the input impedance and the average radial velocity. These can be compared with corresponding quantities readily found both experimentally and from the lumped parameter models given in Chapters 2 and 5.

4.2.2.1 Input Admittance and Average Radial Velocity

The input admittance of an electrical device, as described in Section 2.4.2, is the ratio of current to voltage at its electrical input terminals. In the COMSOL model presented here, the applied voltage V is a boundary condition specified by the user, and the current is given as the surface integral of electric displacement (also known as the charge density), D_{n}:

$$i = \int_A D_{\mathrm{n}} dA, \tag{4.20}$$

where A denotes the electroded surface over which the voltage is applied.

The average radial velocity is found by performing a surface integral of the radial component of the velocity at each point of the moving surface and dividing by the area A of the surface:

$$\bar{v}_r = \frac{1}{A} \int_A \vec{v}(\vec{r}) \cdot \hat{e}_r \, dA, \tag{4.21}$$

where $\vec{v}(\vec{r})$ is the velocity vector at position $\vec{r}$, and $\hat{e}_r$ is a unit vector in the radial direction and the overbar indicates an average. As discussed in

Section 2.4.3, for a transducer with this geometry the average radial velocity is essentially a scaled version of the transmit voltage response and can be used to provide an estimate of the pressure response.

Frequency domain studies of the input admittance and average radial velocity where conducted on the models described in Section 4.2.1 for the normalized frequency range $f/f_0 = 0.25$ to $f/f_0 = 5$ in steps of $f/f_0 = 0.025$. Results are presented in Sections 4.2.2.2 through 4.2.2.5.

4.2.2.2 In-Air Response of Transducer

Figs. 4.10 and 4.11 depict the input admittance and average radial velocity for the transducer without loading resulting from either an internal oil volume or acoustic radiation. This case is most representative of the in-air performance of the transducer, as air has such a relatively low acoustic impedance that its effect is considered negligible. Results are compared with the one-degree-of-freedom model (Model 1) presented in Chapter 3.

Two distinct resonances, appearing as peaks in the admittance and radial velocity curves, can be observed at $f/f_0 = 1.1$ and $f/f_0 = 4.9$, related to axial and bending deformation of the elements, respectively. These are the same resonances discussed in Section 4.1. Fig. 4.12 shows a visual representation of the deformation that occurs in the elements for each of these modes, with a color bar representing the axial material strain in each element. In the breathing mode, it can be seen that most of the strain occurs in the active element (the left stave in the figure). This is because the axial stiffness of the

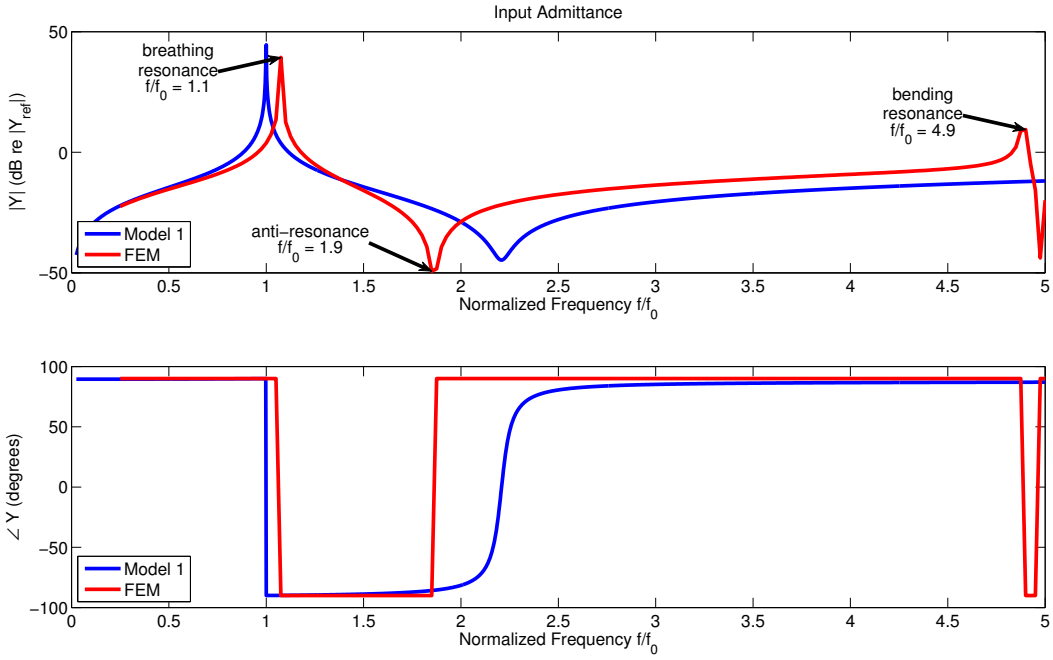

Figure 4.10: Input admittance of transducer (in air) as given by the COMSOL FEM model, compared with results of Model 1. Axial and bending resonances occur at $f/f_0 = 1.1$ and $f/f_0 = 4.9$, respectively.

inactive material is significantly higher than that of the active material and presents a large impedance at this frequency. The axial deformation pushes both elements out radially in unison, consistent with the design described in Section 3.1. In the bending mode, shown in Fig. 4.12(b), the axial strain is uniformly much lower in both the active and inactive elements. The deformation indicates that the elements move out of phase with one another, effectively decreasing the volume pushed out by the transducer and decreasing its effectiveness as a radiator of sound. It can be seen from the admittance and radial velocity plots that the bending resonance has a significant effect on

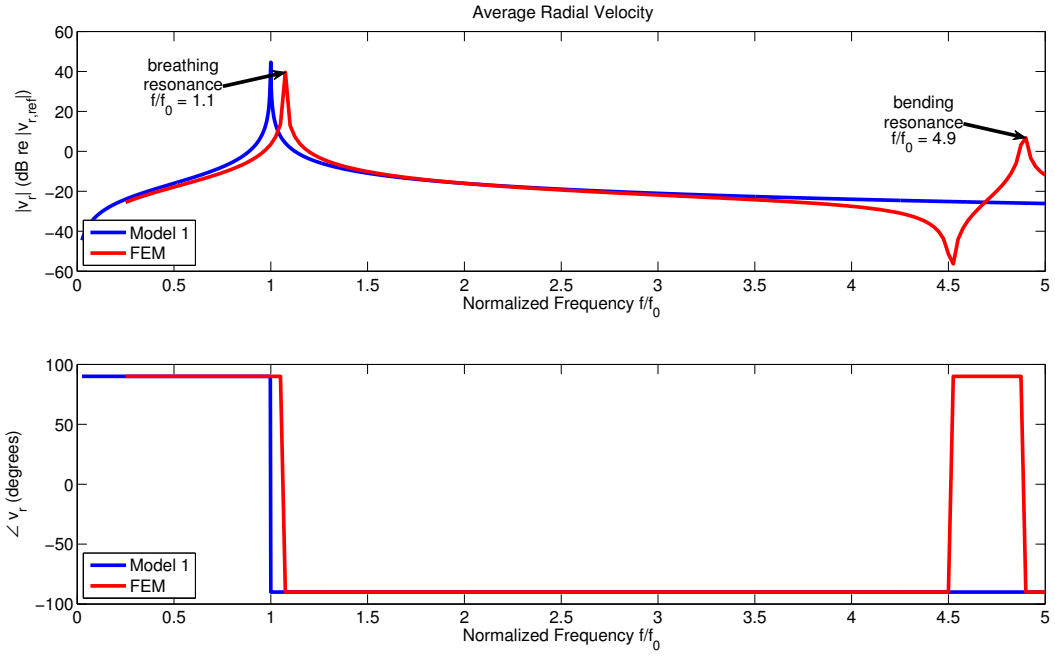

Figure 4.11: Average radial velocity of transducer (in air) as given by the COMSOL FEM model, compared with results of Model 1. Axial and bending resonances occur at $f/f_0 = 1.1$ and $f/f_0 = 4.9$, respectively.

the performance of the transducer.

Additionally, it can be seen from comparison of the admittance curve for the FEM model and Model 1 in Fig. 4.10, that the former exhibits a decreased anti-resonance frequency, at $f/f_0 = 1.9$, in the admittance curve with respect to the same, at $f/f_0 = 2.2$, in the latter. As discussed in Section 2.4.1, this indicates that the electroacoustic efficiency of the transducer in the COMSOL model is lower than that given by Model 1. Specifically, the square of the electromechanical coupling coefficient given by the FEM model

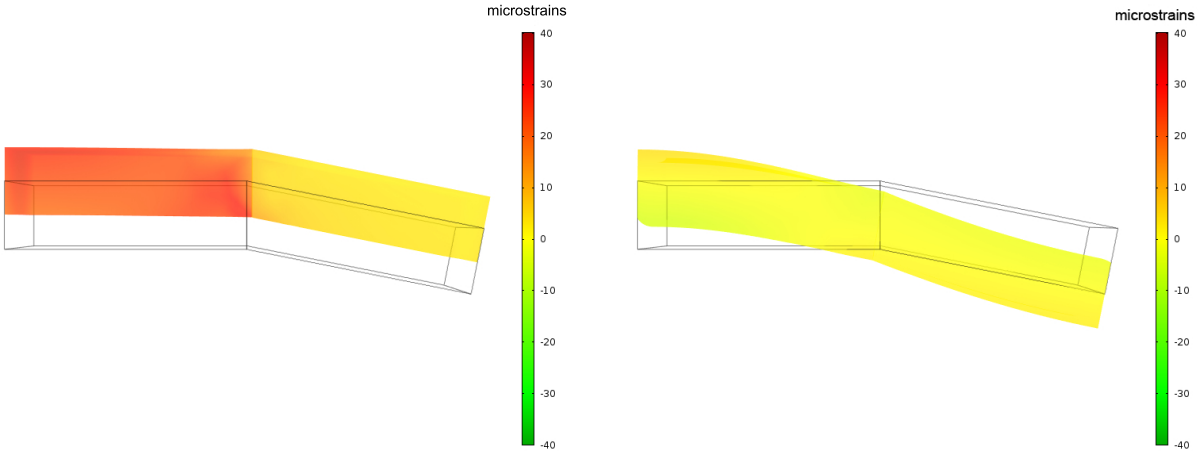

(a) Deformation in axial mode.

(b) Deformation in bending mode.

Figure 4.12: Visual representation of element deformations from COMSOL, with color gradient representing axial strain (in microstrains) for each element. Compare with schematic representations in Figs. 4.5 and 4.6.

is approximated by

$$k^2_{\text{FEM}} = 1 - \frac{1.1^2}{1.9^2} \approx 0.6648, \tag{4.22}$$

while that of Model 1 is approximated by

$$k^2_{\text{Mod1}} = 1 - \frac{1^2}{2.2^2} \approx 0.7934. \tag{4.23}$$

This is primarily a geometrical effect: a ring composed of sections of rectilinear staves (as in the COMSOL model) will necessarily have a less efficient mechanical response than that of a composite ring that is purely cylindrical.

4.2.2.3 Response of Transducer with Internal Oil Volume

Figures 4.13 and 4.14 depict the input admittance and average radial velocity for the transducer with loading due to an internal volume of castor oil, as given by the FEM model and Model 1. The COMSOL FEM model was created as shown in Fig. 4.8, with the exception that the water domain was removed. The internal oil volume introduces an impedance that alters the response of the transducer. The FEM model exhibits three resonances appearing in the frequency band of interest at $f/f_0 = 1.5$, $f/f_0 = 3.3$, and $f/f_0 = 4.2$. The modes associated with these resonances are depicted visually in Fig. 4.15, where a color gradient represents the normalized pressure field inside the oil volume and the deformed ring is superposed on the pressure field with color gradient representing axial strain the elements.

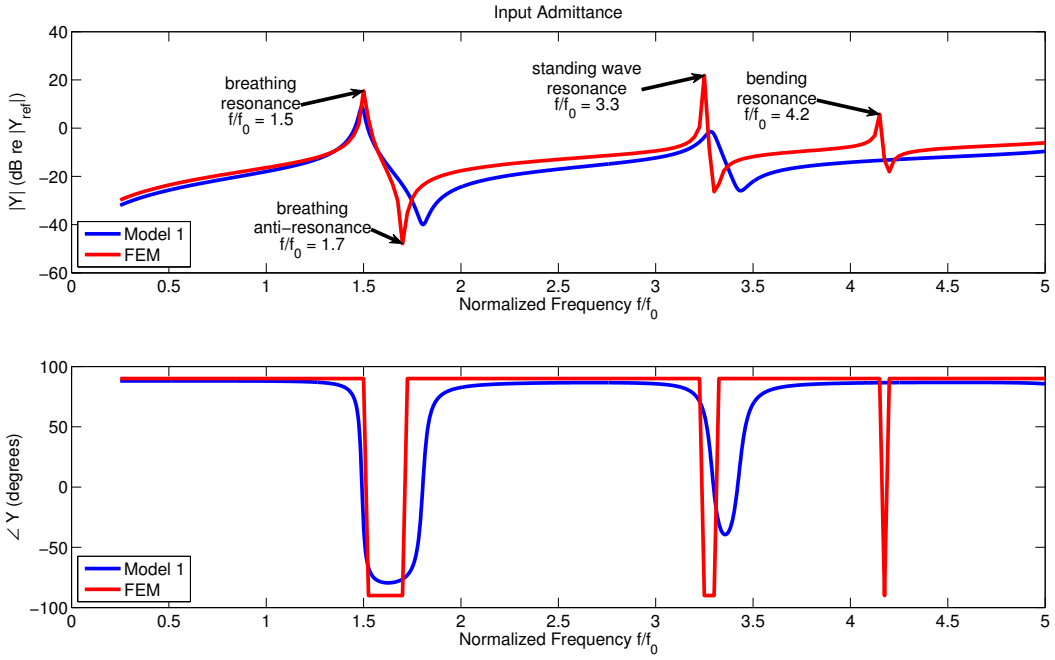

Figure 4.13: Input admittance of transducer (with oil volume) as given by the COMSOL FEM model, compared with results of Model 1. Resonances occur at $f/f_0 = 1.5$, $f/f_0 = 3.3$, and $f/f_0 = 4.2$.

At low frequencies the internal volume acts as a spring (i.e. a lumped compliance), adding stiffness to the system, as described in Section 3.3.3. This is evident in the higher frequency primary resonance observed in comparing the response of the transducer with (at $f/f_0 = 1.5$) and without (at $f/f_0 = 1.1$) the internal volume. A resonance at $f/f_0 = 3.3$ is observed between the primary and bending resonances that is primarily due to standing waves inside the internal volume. In the radial velocity plot, the effects of the oil volume can also be seen in the anti-resonances at $f/f_0 = 2.6$ and $f/f_0 = 4.8$, respectively. The standing wave mode in the internal oil volume occurs at $f/f_0 = 3.3$ and

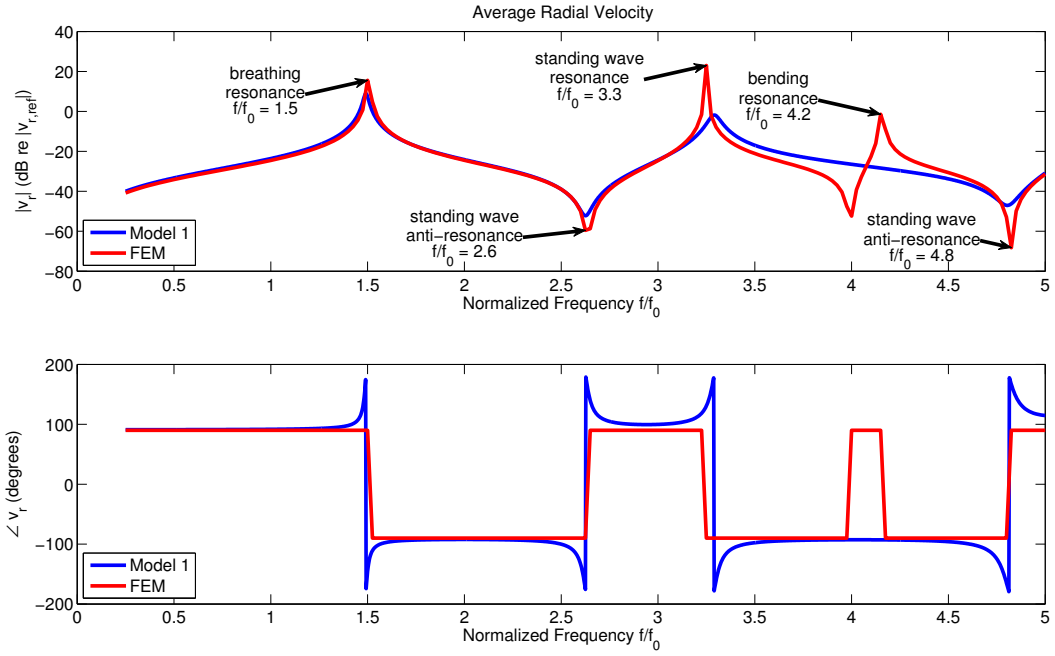

Figure 4.14: Average radial velocity of transducer (with oil volume) as given by the COMSOL FEM model, compared with results of Model 1. Resonances occur at $f/f_0 = 1.5$, $f/f_0 = 3.3$, and $f/f_0 = 4.2$.

is represented visually in Fig. 4.15(b). At higher frequencies near the bending resonance ($f/f_0 = 4.8$), when the staves are moving out of phase with one another, mass in the adjacent oil volume domain is being sloshed around, thus the internal volume acts more like a mass and lowers the bending resonance frequency to $f/f_0 = 4.2$. This effect can be seen visually in Fig. 4.15(c).

For both the admittance and the radial velocity, Model 1 is in fairly good agreement with the FEM model around the first two resonances. By design Model 1 does not capture the third, bending resonance. In the admittance curve it is noted that the FEM results show a higher overall level and

lower anti-resonance frequencies for the first two resonances.

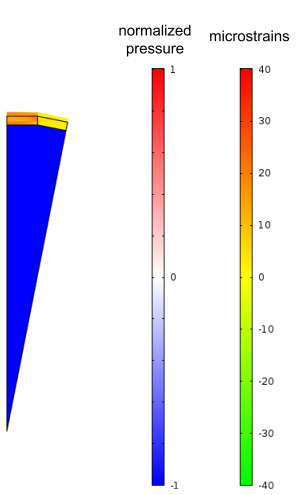

(a) Breathing Mode.

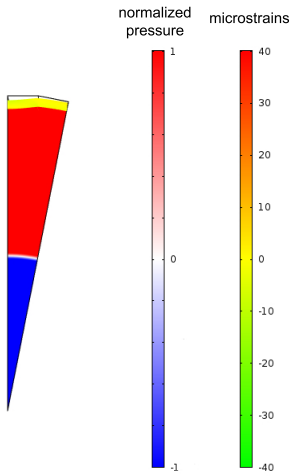

(b) Standing Wave Mode.

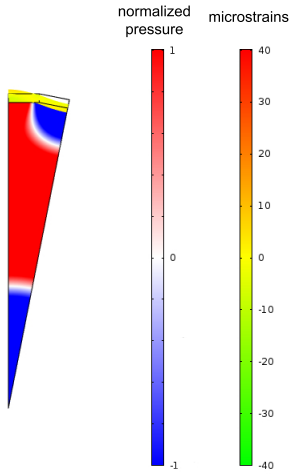

(c) Bending Mode.

Figure 4.15: Visualization of modes in oil volume from COMSOL. The color bars represent the normalized pressure field and axial strain in the oil volume and elements respectively.

4.2.2.4 Response of Transducer with Radiation Loading

The results of the COMSOL model for an air-filled transducer in water are shown in Figs. 4.16 and 4.17, along with that of Model 1. The COMSOL FEM model was created as shown in Fig. 4.8 with the exception that the oil domain was replaced with air. As shown in that figure, a cylindrical wave radiation condition was imposed at the outer-most radial surface, approximating free-field conditions where no waves are reflected back into the water domain from the boundary. When the transducer radiates sound into an external medium, it is subject to the impedance resulting from this radiation. As indicated by the radiation impedance model for a finite cylinder discussed in Section 3.3.2.2, this impedance is primarily mass-like at low frequencies, and becomes increasingly resistive as the frequency is increased. The frequency where this transition occurs depends on both the radius of the transducer and its height. As described in Section 4.2.1, the water domain in the COMSOL model is effectively infinite in extent due to the acoustically hard boundary conditions imposed on the top and bottom wedge walls (the faces perpendicular to x_2). As a result, the modeled transducer sees the radiation impedance of an infinite, rather than finite, length cylinder. Because the radiation impedance imposed on an infinite cylinder is significantly more resistive than that imposed on a finite cylinder, the performance of the transducer given by the COMSOL model is much more heavily damped than that of Model 1. Despite this extra damping in the COMSOL model, a strong bending resonance persists, at around $f/f_0 = 4$.

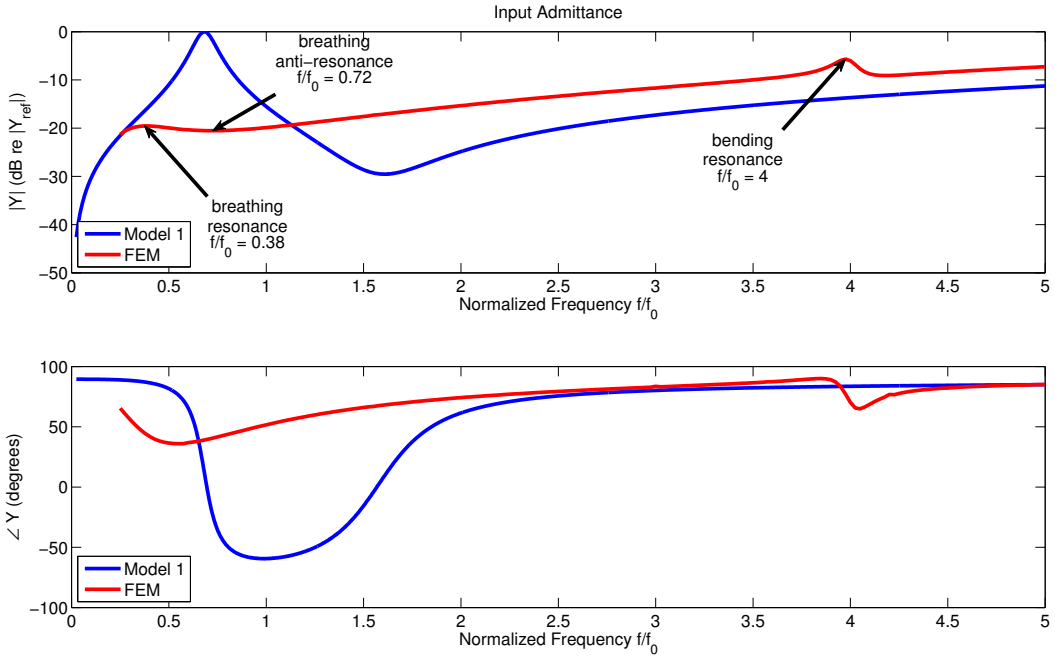

Figure 4.16: Input admittance of transducer (air-filled, with radiation loading) as given by the COMSOL FEM model, compared with results of Model 1. Resonances occur at $f/f_0 = 0.38$ and $f/f_0 = 4$.

The COMSOL results shown in Figs. 4.16 and 4.17, with effective radiation impedance of an infinite cylinder, can be manipulated to represent the response of a transducer ring subject to the radiation impedance of a finite cylinder. Appendix D details this process and the results are shown here in Figs. 4.18 and 4.19. The response for the finite cylinder case is significantly less damped, with sharper breathing mode resonance peaks that are shifted to a higher frequency. The bending resonance appears equally strong and at the same frequency in both infinite and finite cylinder case, because the magnitudes of the infinite and finite cylinder radiation impedance begin to converge

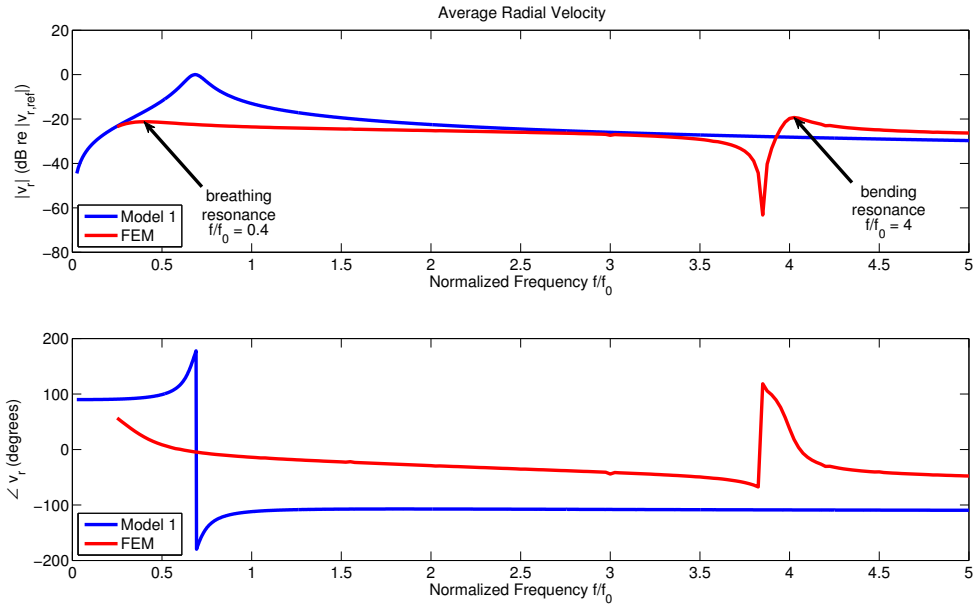

Figure 4.17: Average radial velocity of transducer (air-filled, with radiation loading) as given by the COMSOL FEM model, compared with results of Model 1. Resonances occur at $f/f_0 = 0.40$ and $f/f_0 = 4$.

around the frequency that the bending resonance takes place (see Fig. D.7).

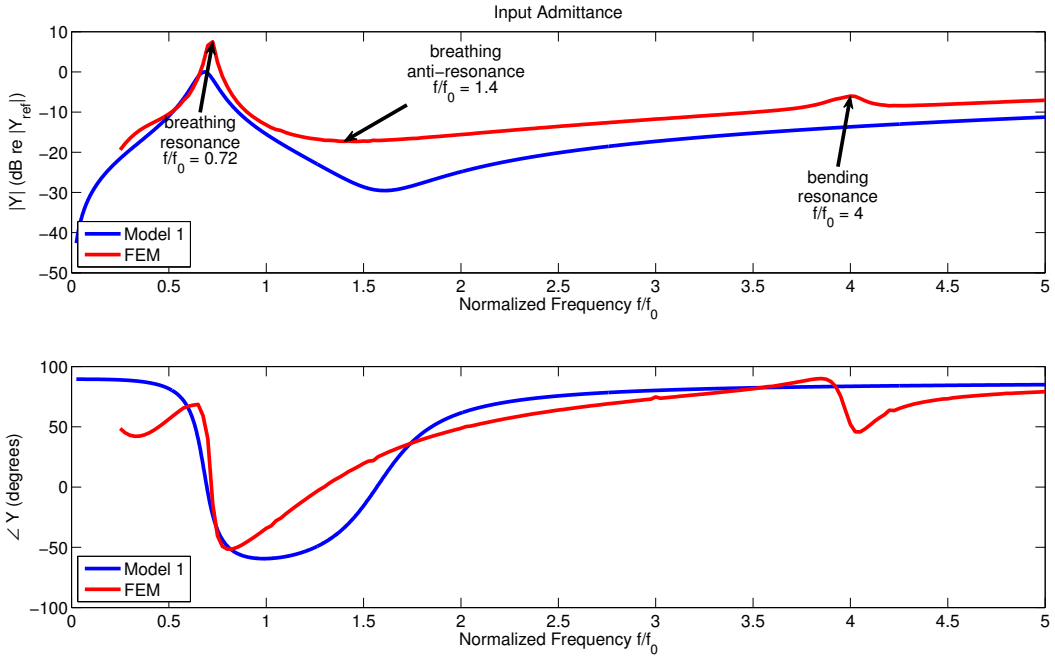

Figure 4.18: Input admittance of transducer (air-filled, with finite cylinder radiation loading) as given by the COMSOL FEM model, compared with results of Model 1. Resonances occur at $f/f_0 = 0.72$ and $f/f_0 = 4$.

The results of the FEM model, as corrected for the finite cylinder case, indicate that both the primary and secondary resonances are reduced in frequency with respect to the in-air case. The breathing and bending resonances occur at $f/f_0 = 0.72$ and $f/f_0 = 4$, respectively, down from $f/f_0 = 1.1$ and $f/f_0 = 4.9$, respectively for the in-air case. At frequencies near the bending resonance, when the staves are moving out of phase with one another, the transducer is less effective in radiating sound into the water medium, as much of the mass of the water is sloshed back and forth between the staves rather than being compressed.

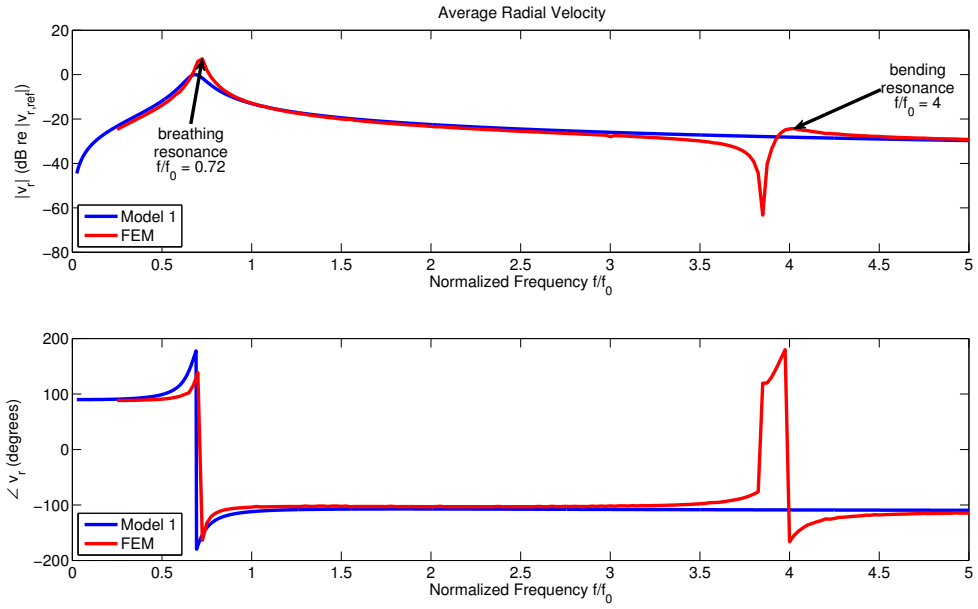

Figure 4.19: Average radial velocity of transducer (air-filled, with finite cylinder radiation loading) as given by the COMSOL FEM model, compared with results of Model 1. Resonances occur at $f/f_0 = 0.72$ and $f/f_0 = 4$.

4.2.2.5 Response of Transducer with Internal Oil Volume and Radiation Loading

When the transducer is subject to loading from an internal oil volume and acoustic radiation into water the effects of both can be observed. In order to separate the influence of the oil and water loading and effectively track each resonance, COMSOL simulations were performed with the transducer radiating sound into a water-like medium of various levels of impedance. This was done by allowing ρ_{w} and c_{w}, the sound speed and density of water, to vary from zero to that of water. The FEM model was created from COMSOL exactly as shown in Fig. 4.8, where the boundary conditions imposed present

the transducer with the radiation impedance of an infinite cylinder. The results of this study are presented in Figs. 4.20 and 4.21. It can be seen that the primary effect of increasing the impedance of the medium being radiated into is to dampen the resonances and reduce the frequency at which they occur.

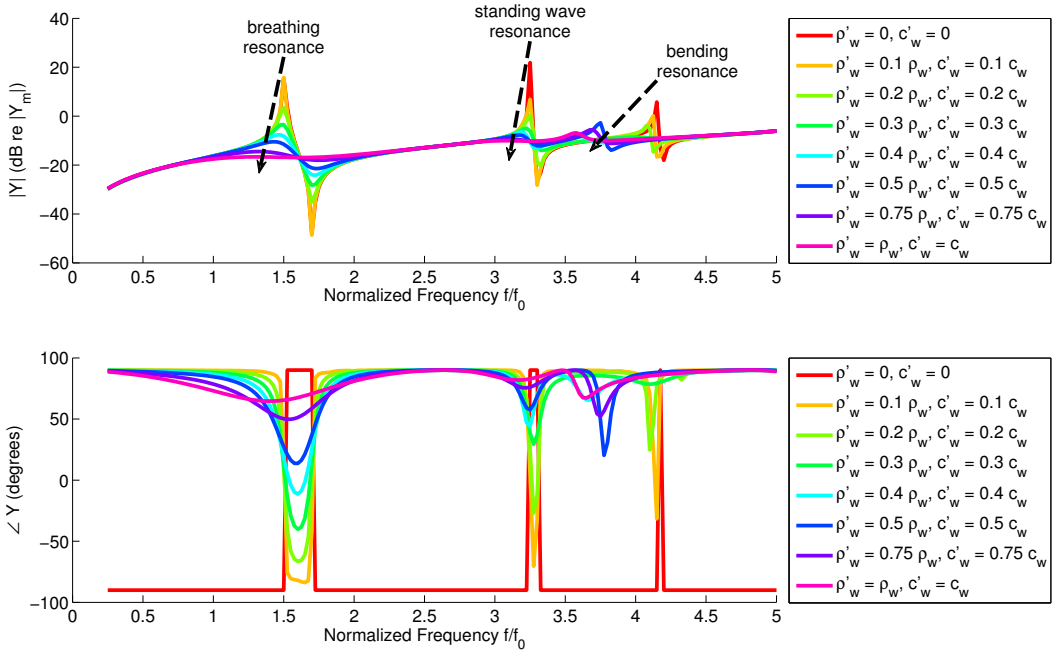

Figure 4.20: Input admittance of transducer with radiation loading due to water-like medium of increasing impedance.

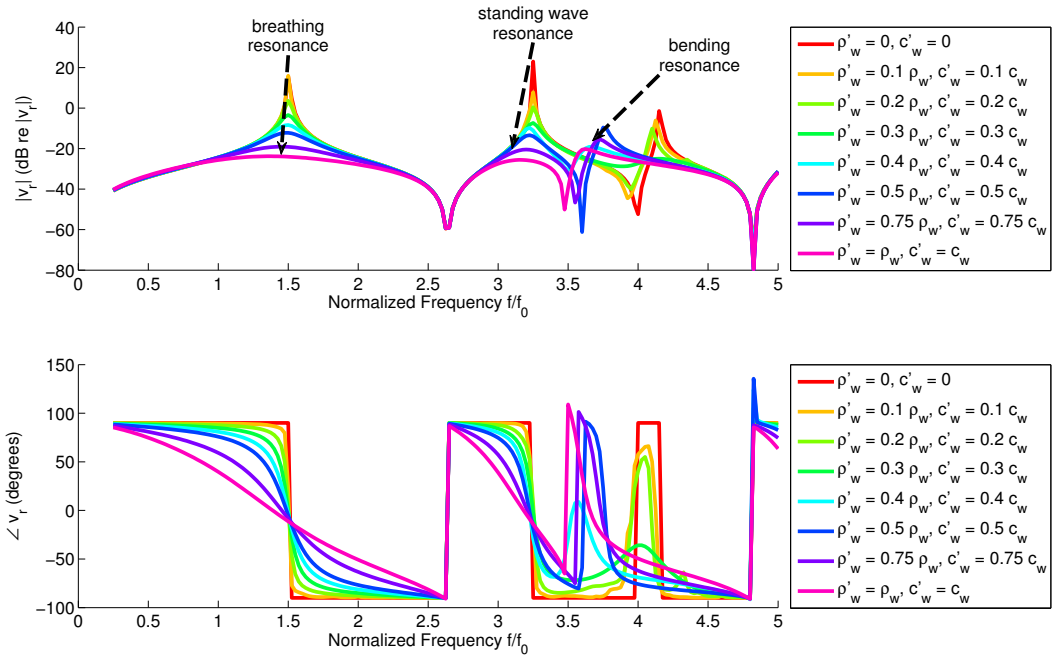

Figure 4.21: Average radial velocity of transducer with radiation loading due to water-like medium of increasing impedance.

The response of the FEM model and Model 1 subject to loading from an internal oil volume and acoustic radiation into water (with true density and sound speed) is shown in Figs. 4.22 and 4.23. The FEM results have been modified to represent the response of a transducer ring subject to the radiation impedance of a finite cylinder, as described in Appendix D. The stiffness of the oil volume slightly increases the frequency at which primary axial resonance occurs, from $f/f_0 = 1.1$ to $f/f_0 = 1.3$. The mass of oil and water sloshing around dramatically decreases the frequency at which the bending resonance occurs, here at $f/f_0 = 3.6$. Effects of the the oil volume can be seen in both plots in the standing wave resonance around $f/f_0 = 3$ and, in the radial

velocity results, in the anti-resonances around $f/f_0 = 2.6$ and $f/f_0 = 4.8$.

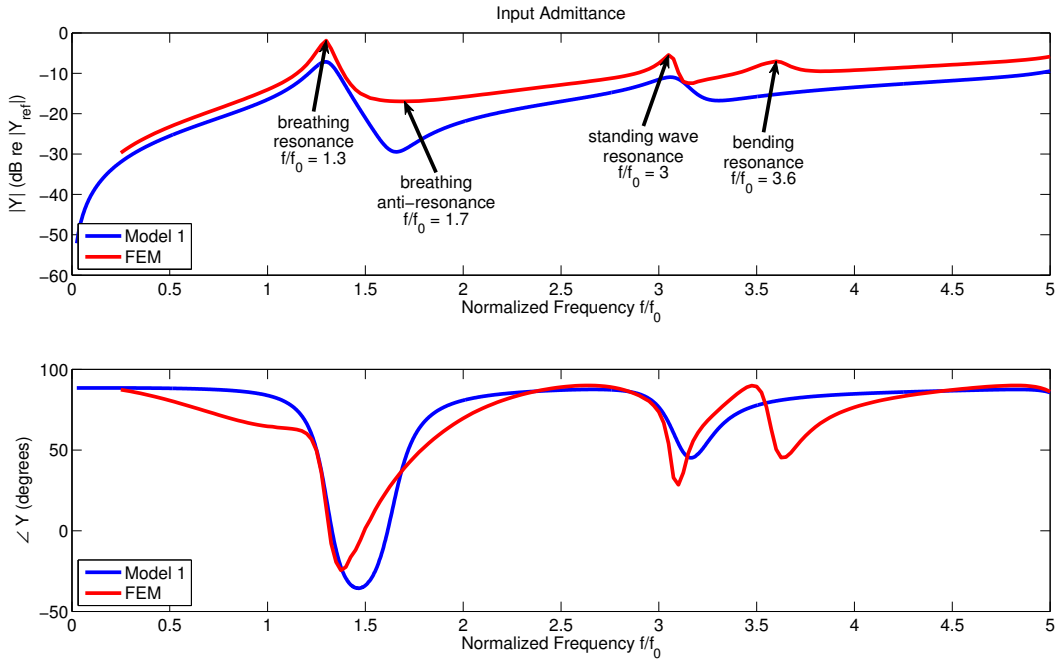

Figure 4.22: Input admittance of transducer (with oil and radiation loading) as given by the COMSOL FEM model, compared with results of Model 1. FEM results have been modified to represent the response of a transducer ring subject to the radiation impedance of a finite cylinder, as described in Appendix D. from Resonances occur at $f/f_0 = 1.3$, $f/f_0 = 3$, and $f/f_0 = 3.6$.

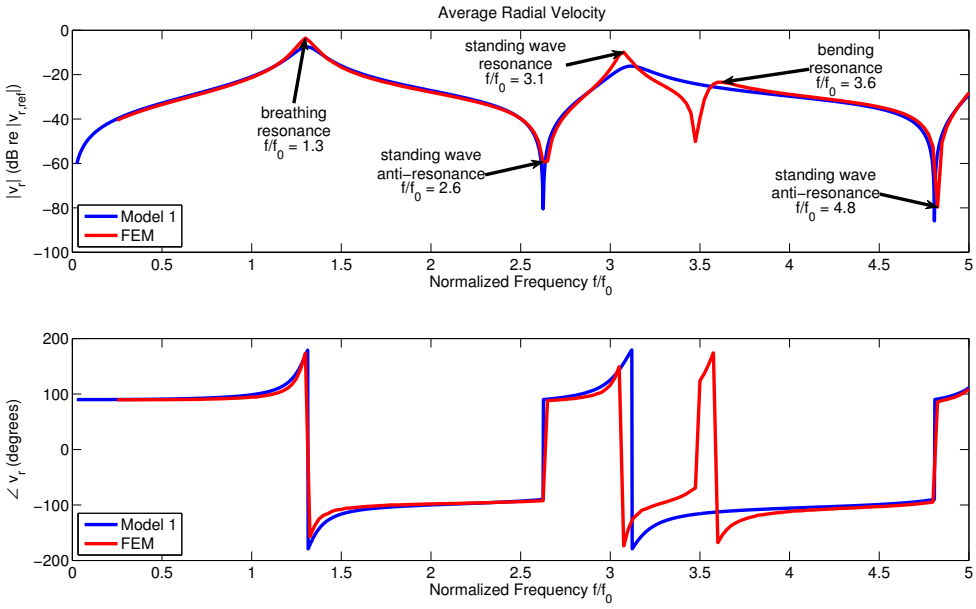

Figure 4.23: Average radial velocity of transducer (with oil and radiation loading) as given by the COMSOL FEM model, compared with results of Model 1. FEM results have been modified to represent the response of a transducer ring subject to the radiation impedance of a finite cylinder, as described in Appendix D. Resonances occur at $f/f_0 = 1.3$, $f/f_0 = 3.1$, and $f/f_0 = 3.6$.

4.2.2.6 Summary of Modification Effects

A summary of the effects of modifications to the FEM COMSOL model are presented in Table 4.2. The primary breathing resonance, breathing anti-resonance, standing wave resonance, and bending resonance frequencies are presented for each case indicated.

Table 4.2: Effect of Modifications to FEM COMSOL Model on Resonances of Interest

	Breathing Resonance f/f_0	Breathing Anti-Resonance f/f_0	Standing Wave Resonance f/f_0	Bending Resonance f/f_0
In-Air	1.1	1.9	-	4.9
Oil Volume	1.5	1.7	3.3	4.2
Radiation Loading	0.72	1.4	-	4
Oil Volume and Radiation Loading	1.3	1.7	3	3.6

4.3 Conclusions

The finite element method results presented in this chapter indicate that the simple one-degree-of-freedom model (Model 1, as presented in Chapter 3) does not adequately capture the true performance of the transducer. The COMSOL model provides a more realistic estimate of the transducers electroacoustic efficiency, which Model 1 overestimates due to geometrical approximations. More significantly, Model 1 neglects effects due to the bending mode of the transducer that are captured by the finite element models. This

makes Model 1 a problematic design tool as this bending mode can drastically reduce the transducer's effectiveness at radiating sound.

As discussed earlier, finite element models with multiple domains and high resolution can be computationally costly and are not ideal for the initial stages of design. It is therefore preferable to have an analytical model that can capture not only the breathing mode that the ring is designed to operate in, but the bending mode, which one would hope to avoid. One such model is developed in Chapter 5, the results of which are compared with Model 1 and the finite element models from this chapter.

Chapter 5

Multi-Degree-of-Freedom Model with Bending

The transducer model for the 31-mode ring described in Chapter 3 has only one degree of freedom and thus can only capture the fundamental breathing mode resonance of the ring. This is the mode at which the ring was designed to operate, though the finite element method results shown in Chapter 4 indicate that the ring has a higher frequency mode within the operating frequency band of interest. This second resonance, referred to here as a bending resonance, negatively affects the performance of the transducer because it leads to a scenario where nearly equal areas of the ring vibrate 180 degrees out of phase. The COMSOL models described in Section 4.2 exhibit this resonance, but can cost significant computational time and power. For this reason, a relatively simple lumped parameter transducer model is sought that can capture this parasitic second resonance and thus enable improved design capabilities for segmented cylindrical transducers. The following is a development of a multi-degree-of-freedom (MDOF) lumped parameter model that captures this bending resonance and provides a more accurate estimate of the efficiency of the transducer. As the final version of this model is quite complicated, the development begins with the simplest possible model and proceeds with modifications until the model is complete, in order to ensure

accurate modeling of the dominant physics at each level of complexity. Model predictions will be shown as mechanical schematics, equivalent circuits, and bond graphs at each step in order to benefit from the insight provided by each. Results are compared with that of analogous cases using Model 1 and the COMSOL FEM model described in Chapters 3 and 4. Due to concerns of the project sponsor, all results have been normalized according to the scheme described in Appendix A.

5.1 Reduced Model

To make a complicated model with multiple degrees of freedom more tractable, it is useful to exploit the radial symmetry of the design so that the model is reduced to the minimum number of independent variables. Each active element in the ring is electroded identically and excited by the same applied voltage, causing them to move in phase with one another. Because of this symmetrical driving voltage and the symmetrical geometry of the ring, an equivalent model of the segmented ring can be created from an adjacent active and inactive element pair on which zero normal displacement, zero rotation boundary conditions (referred to here in shorthand as roller boundary conditions) have been imposed at the lengthwise midpoint of each element, as shown in Figure 5.1. All modes of the full ring subject to electrical excitation are captured in this unit cell. For the analysis presented here, element properties are subscripted with i, where $i = 1$ and $i = 2$ indicate properties of the active and inactive elements respectively. The unit cell contains an active and an

inactive element with length dimension (along the circumference of the ring) half that of the original length L_1 and L_2 respectively, that is, $l_1 = L_1/2$ and $l_2 = L_2/2$. For a ring with N elements (both active and inactive), this unit cell is repeated N times around the circumference of the ring and the angle θ that the unit cell subtends is given by $\theta = 2\pi/N$. The roller condition ensures that points on the elements at the boundaries of the unit cell only move radially. This reduced model decreases computational time while producing identical solutions to a model with the same physical assumptions that considers all elements of the ring. Electrical excitation is indicated by the leads and applied voltage V.

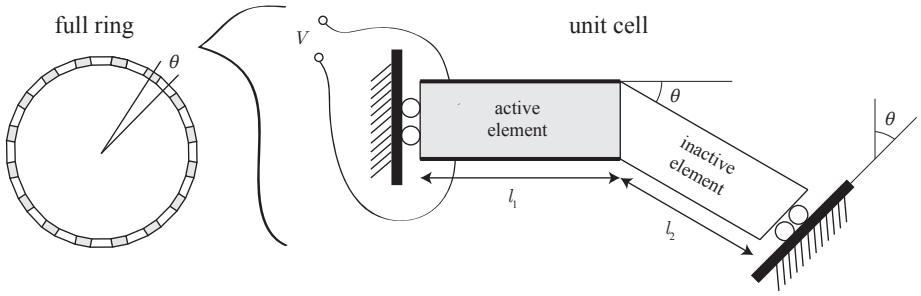

Figure 5.1: Unit cell of ring, subtending angle θ, with roller boundary conditions.

5.2 Single-Degree-of-Freedom System Modeling

The simplest possible model for the unit cell has one degree of freedom and thus one equation of motion. The reduced model shown in Fig. 5.1 can be modeled with one degree of freedom by neglecting the electrical domain, re-

moving the angle (or alternatively, setting $\theta = 0$), and restricting the elements to motion along their axes. Though such a model is necessarily an inaccurate representation of the system, it provides insight that can be used in the creation of the more accurate, higher-degree-of-freedom, models presented in Section 5.3. A lumped parameter model for an element stave as an axial bar is presented in Section 5.2.1, and used in Sections 5.2.2, 5.2.3, and 5.2.4 to model the one-degree-of-freedom system with zero angle, nonzero angle, and nonzero angle with electrical excitation respectively. Equations of motion are found for the purely mechanical systems described in Sections 5.2.2 and 5.2.3. When the electrical excitation is considered in Section 5.2.4, the response of the system is represented by its input electrical admittance.

5.2.1 Elements as Lumped Parameter Axial Bars

The development of this model first neglects bending effects in each element to ensure that the fundamental breathing mode is captured by this representative instantiation. This mode results from motion along the circumference of the ring, that is, along the axis of each element, and will be referred to here as the axial mode. In this approximation, each element behaves like a bar subject only to axial forces F and displacements u as shown in Fig. 5.2.

A uniform bar of length l, cross-sectional area A, density ρ, and Youngs modulus E[1] has total mass is $M = \rho A l$ and axial stiffness is $k = AE/l$. The

[1] As in Chapter 4, E is used here for the Young's modulus rather than Y. Note that here E does not represent electric field as it in Chapters 2 and 3.

axial motion of such a bar can be modeled by assuming distributed mass and stiffness throughout the bar or by lumping these into a finite number of mass and spring elements. This model employs a basic "T" model lumping procedure that accounts for all intertial and stiffness effects with the simple mass-spring-mass system shown in Fig 5.3. Systems are well represented by lumped parameter models when the wavelength in the material is much longer than any dimension of the lump. For the frequency range we are concerned with here, a lumped model is sufficient, though it should be noted that a distributed "T" model can be used in place of the lumped mass and stiffness elements if necessary (see Sherman and Butler, Chapter 7 [7]).

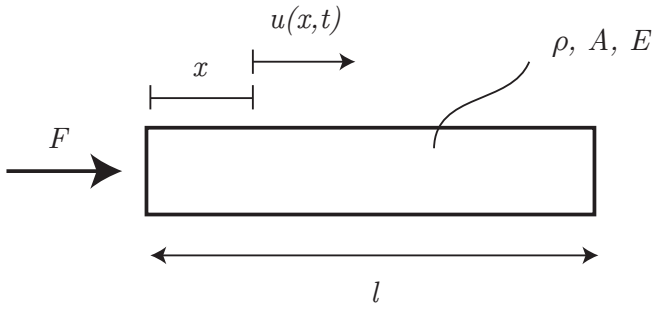

Figure 5.2: Element as axial bar, adapted from Meirovitch [16].

For the simplest two-degree-of-freedom "T" model, the mass of the bar is distributed between two point masses, each with mass

$$m = M/2 = \rho Al/2, \tag{5.1}$$

and the stiffness is represented by one massless spring of stiffness

$$k = AE/l, \tag{5.2}$$

or conversely, of mechanical compliance

$$c = l/AE. \tag{5.3}$$

Figures 5.3 depicts the mechanical schematic, equivalent circuit, and bond graph for one such bar.

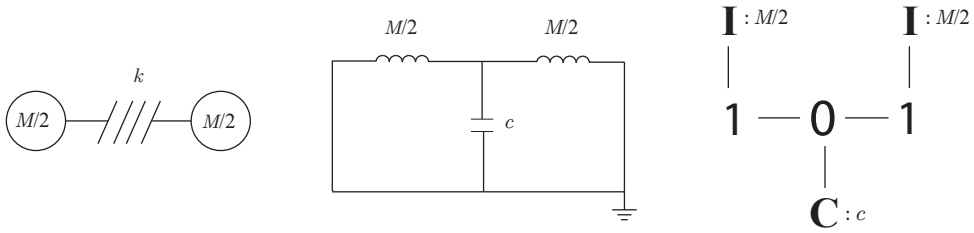

Figure 5.3: Mechanical schematic, equivalent circuit, and bond graph lumped parameter models for axial rod.

5.2.2 One-Degree-of-Freedom Model, with Zero Angle

Modeling both the active element and inactive element in our reduced system as two-mass "T" models produces a total of four degrees of freedom for the combined system, with mass and stiffness elements given by Eqs. (5.1) through (5.3), subscripted with 1 and 2 for the active and inactive element respectively.

Temporarily neglecting the angle θ offsetting the inactive element (or alternatively setting the angle to zero) produces system shown in the top half of Fig. 5.4. The degrees of freedom are represented by the axial displacement of each mass, u_1 and u_2 for the active element, and u_3 and u_4 for the inactive element. Connecting one mass from each element at the joint of the elements equates u_2 and u_3 and reduces the degrees of freedom by one. Imposing roller boundary conditions (in this one-dimensional case equivalent to a rigid, zero axial displacement condition if rigid body vertical motion is neglected) sets $u_1 = u_4 = 0$, further reducing the degrees of freedom to one. Thus $u_2 = u_3 = u$ as shown in Fig. 5.4. A 0mechanical schematic, equivalent circuit, and bond graph of the system are shown in Fig. 5.5. In the equivalent circuit, the motion of the mass is represented by the velocity $\dot{u}$, where dot notation is used to indicate the time derivative of the displacement. Likewise, in the bond graph the velocity is represented as a generalized flow at the **1**-junction, which represents common flow. For more information on equivalent circuit and bond graph models, see Beranek [17] and Karnopp and Margolis [18], respectively.

Using Newton's second law, the equation of motion for the combined mass $M_1 + M_2 2$, without no driving force, is

$$\left(\frac{M_1 + M_2}{2}\right) \ddot{u} = -\left(k_1 + k_2\right) u, \tag{5.4}$$

or

$$\left(\frac{M_1 + M_2}{2}\right) \ddot{u} + \left(k_1 + k_2\right) u = 0, \tag{5.5}$$

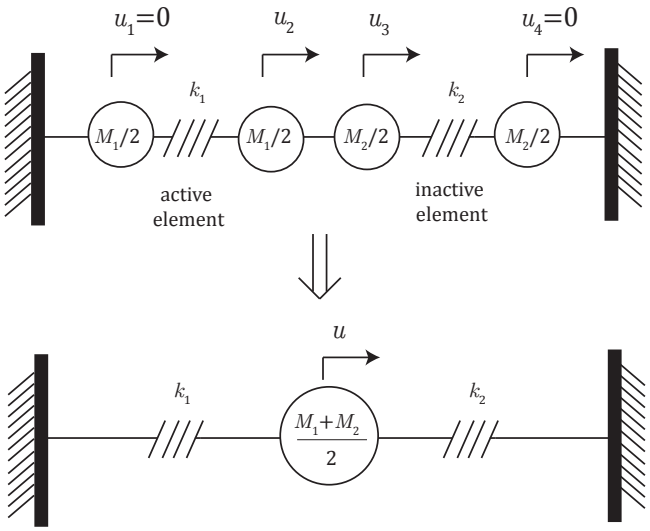

Figure 5.4: 1-DOF axial model with no angle.

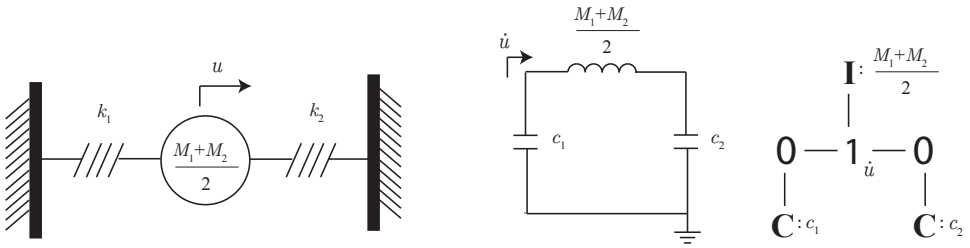

Figure 5.5: Mechanical schematic, equivalent circuit, and bond graph for 1-DOF axial model with no angle.

where $\ddot{u}$ is used to indicate the second derivative of u with respect to time. Equation 5.9 is the classical equation for a simple harmonic oscillator. By assuming time-harmonic displacements with angular frequency ω, it can be

written as

$$\left((k_1 + k_2) - \omega^2 \left(\frac{M_1 + M_2}{2}\right)\right) u = 0. \tag{5.6}$$

The angular resonance frequency, at which u is unbounded, is given by

$$\omega_\mathrm{r} = \sqrt{\frac{2(k_1 + k_2)}{M_1 + M_2}}, \tag{5.7}$$

or as resonance frequency

$$f_\mathrm{r} = \frac{1}{2\pi}\sqrt{\frac{2(k_1 + k_2)}{M_1 + M_2}}. \tag{5.8}$$

For material parameters given by that of Appendix A, the normalized resonance frequency is $f_\mathrm{r}/f_0 = 39.25$. This is significantly higher than the resonance frequency given by Model 1, due to the axial motion restriction in this model. As will be seen in Section 5.3.1, the system becomes less stiff as vertical motion is allowed, lowering this primary resonance.

5.2.3 One-Degree-of-Freedom Model with Nonzero Angle

To account for the geometry of the ring, the inactive element may be rotated in the unit cell by an angle θ as indicated by Fig. 5.1. The displacement of the mass in this rotated coordinate system is notated as u' and given geometrically by $u' = u\cos\theta$. In the equivalent circuit and bond graph, this rotation is represented by a transformer with turns ratio $1/\cos\theta$, as per transformer conventions. The transformer is represented schematically by two inductors in the equivalent circuit, and as **TF** in the bond graph. A mechanical schematic, equivalent circuit, and bond graph for this system are shown in

Fig. 5.6. Note that while they are still rigidly attached and represent a single degree of freedom, the masses have been drawn separately in the schematic to facilitate solving the dependent equations of motion for each.

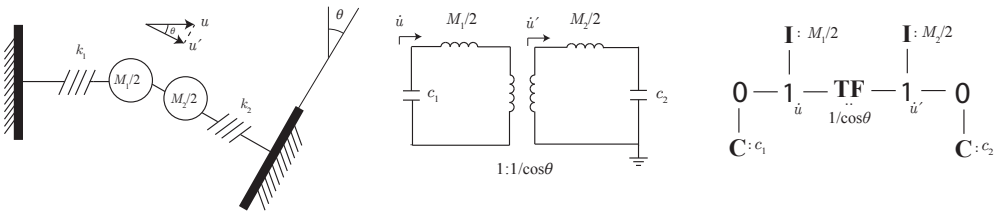

Figure 5.6: Mechanical model, equivalent circuit, and bond graph for angled axial model.

With no driving force, the equation of motion for this system is given by

$$\left(\frac{M_1}{2} + \frac{M_2}{2}\cos^2\theta\right)\ddot{u} + \left(k_1 + k_2\cos^2\theta\right)u = 0. \tag{5.9}$$

Assuming time-harmonic displacements as before, the resonance frequency of the system is given by

$$f_\mathrm{r} = \frac{1}{2\pi}\sqrt{\frac{2(k_1 + k_2\cos^2\theta)}{M_1 + M_2\cos^2\theta}}. \tag{5.10}$$

It can be seen from Eq. (5.10) that both the stiffness and the mass of the system are decreased by the addition of the angle. Using the material properties given in Appendix A, the normalized resonance frequency of the angled 1 DOF system is $fr/f_0 = 31.75$, significantly reduced from $fr/f_0 = 39.25$ for the non-angled case.

5.2.4 One-Degree-of-Freedom-Model, with Nonzero Angle and Electrical Excitation

The system is coupled into the electrical domain by the piezoelectric properties of the active element, as governed by the canonical equations (Eqs. 3.1 and 3.2). As described for the full ring in Section 3.1, the electrical properties of the piezoelectric material can be represented by a lumped capacitance C_0, given by Eq. 3.22, and the coupling between electrical and mechanical domains by the electromechanical turns ratio ϕ, given by Eq. 3.10. Additionally, the system is driven by electrical excitation in the form of an applied voltage V. The models presented in Fig. 5.6 can be augmented to include these electrical effects, as shown in Fig. 5.7. Note the electrical loss conductance G_0 has been ignored here for the sake of simplicity. In the mechanical model, the capacitance of the element is represented as a mechanical spring, the compliance of which is the capacitance transformed into the mechanical domain. Likewise, the applied voltage appears as an applied force. In the equivalent circuit and bond graph model, the electrical and mechanical domains are coupled through ideal transformers with turns ratio ϕ.

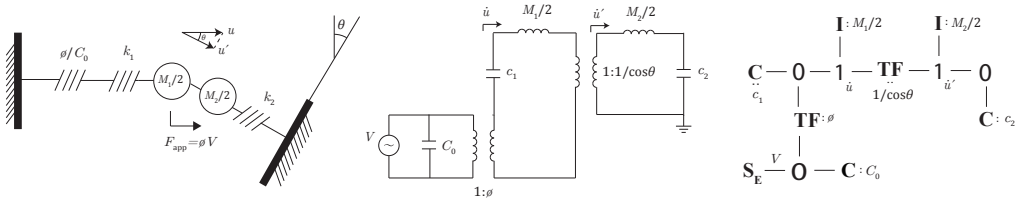

Figure 5.7: Mechanical model, equivalent circuit, and bond graph for angled axial model with electrical excitation.

The input electrical admittance of the equivalent circuit shown in Fig. 5.7 is shown in Fig. 5.8. When driven by an applied voltage, the resonance of the system appears as a peak in the admittance curve, occurring here at normalized frequency $f/f_0 = 31$. This resonance frequency is slightly lower than that of the purely mechanical system, due to the compliance added by the capacitive properties of the piezoelectric material.

5.3 Two-Dimensional Modeling

The system can only be accurately modeled if the elements are allowed to move in the transverse, as well as axial, direction. This adds a degree of freedom to the system and necessitates a method for coupling motion in the axial and transverse domains. This is done in the following section using ideal transformers to represent a coordinate transform. A model, referred to as Model 2, is presented in Section 5.3.1 that allows for transverse motion and incorporates the roller boundary conditions of the ring unit cell. Section 5.3.3 develops a model, referred to as Model 3, that adds more degrees of freedom

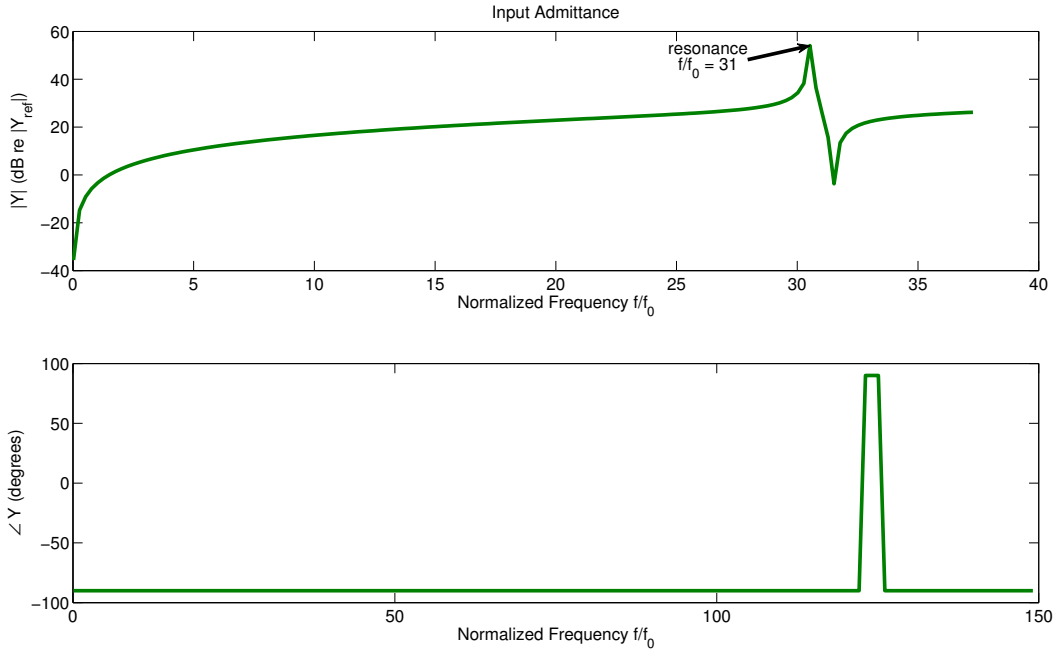

Figure 5.8: Input admittance for one-degree-of-freedom angled axial model with electrical excitation. Resonance occurs at $f/f_0 = 31$.

to the system by allowing for bending motion in the elements, and represents the final stage of the development presented here. Following the development of each model is an analysis of its performance. As the transverse direction is roughly in line with the radial direction of the full ring, plots of the average radial velocity and transmit voltage response are included in addition to electrical admittance plots.

5.3.1 Model 2: Two-Dimensional Axial Model with Nonzero Angle

Two-dimensional motion can be accounted for by introducing a transverse degree of freedom, w, orthogonal to each axial displacement u. When

such motion is allowed, the rigid boundary condition show in Fig. 5.4 reverts to a roller condition to indicate that only axial motion is restricted at the boundaries. The mechanical model for this case is shown in Fig. 5.9, where axial and transverse displacements for each mass are labeled for the sake of clarity. The orthogonal displacements u and w can be used to determine the corresponding displacements u' and w' in the rotated coordinate system. Specifically, for the ith mass, the displacements in the rotated coordinate system are given by the coordinate transform

$$\begin{Bmatrix} u_i' \\ w_i' \end{Bmatrix} = \begin{bmatrix} \cos\theta & \sin\theta \\ -\sin\theta & \cos\theta \end{bmatrix} \begin{Bmatrix} u_i \\ w_i \end{Bmatrix}. \tag{5.11}$$

Because of the complicated coupling of degrees of freedom due to the angled axial spring representing the inactive element, a bond graph model, shown in Fig. 5.10, provides perhaps the most convenient representation. Note that bonds have been augmented here to explicitly show the direction of power flow. In the bond graph, each of the flows (here velocities) for axial and transverse motion are represented by **1**-junctions. These flows are labeled in blue as time derivatives of the corresponding displacements next to the appropriate **1**-junctions for convenience. The top half of the bond graph structure models the transverse motion while the bottom half models the axial motion. Similarly, the left half of the figure is in the original coordinate system and the right half is in the rotated coordinate system. The coordinate transform is accomplished though ideal transformers which couple the transverse and axial domains as indicated by Eq. (5.11). As an example, consider the **1**-junction

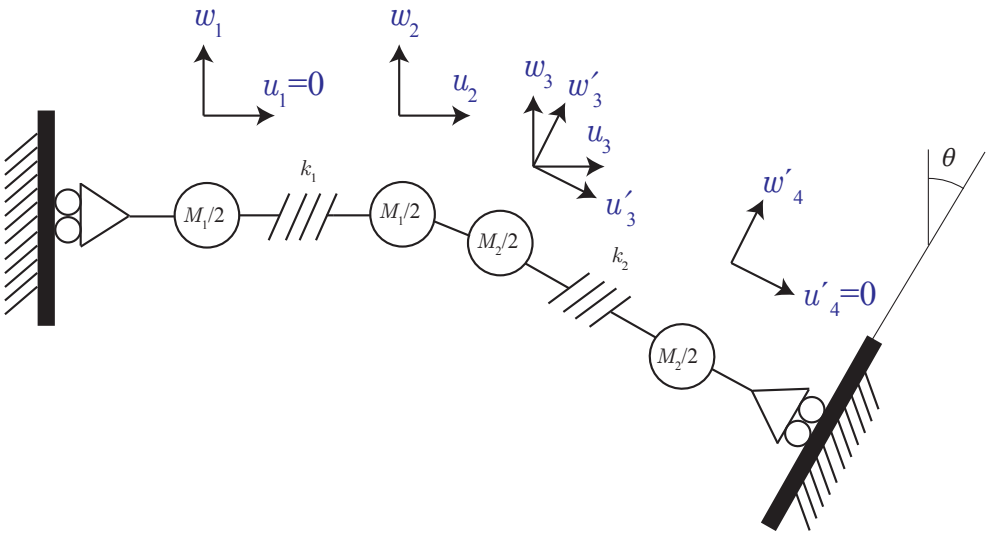

Figure 5.9: 2D axial mechanical model

labeled du_2'/dt. The **0**-junction to the left of it represents a common effort junction for which the sum of the flows must be zero as prescribed by bond graph rules, here analogous to Kirchhoff's current law. Accounting for the direction of each flow as indicated by the arrows on the bonds, transforming the flows du_2/dt and dw_2/dt as indicated by the transformers, and summing the flows to zero at the **0**-junction yields the equation

$$\frac{du_2'}{dt} = \frac{du_2}{dt}\cos\theta + \frac{dw_2}{dt}\sin\theta \tag{5.12}$$

which is consistent with Eq. (5.11) since the time derivative is independent of the transform.

The roller boundary conditions appear as zero effort sources,$\mathbf{S_E}$, on the outer transverse **1**-junctions and as zero flow sources, $\mathbf{S_F}$, on the outer

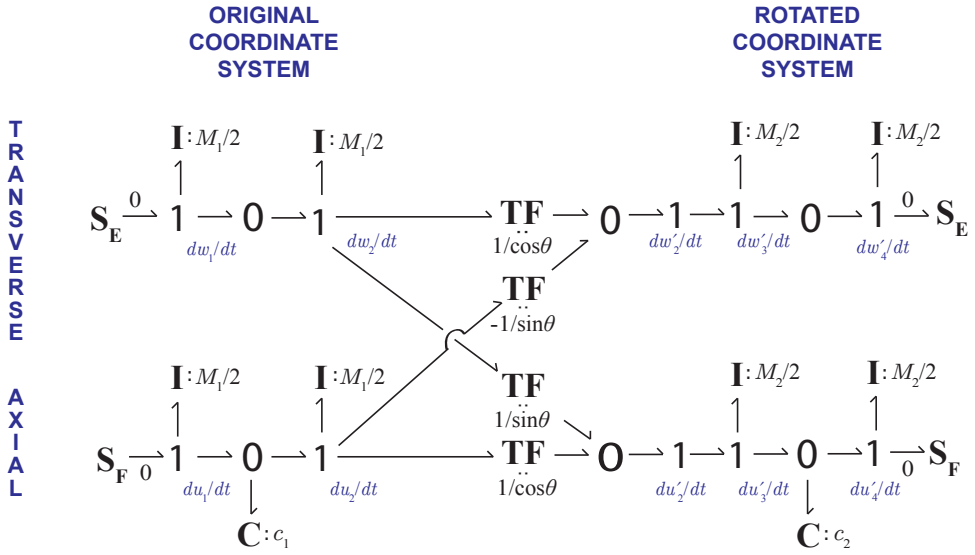

Figure 5.10: 2D axial bond graph model.

axial **1**-junctions, as shown in Fig. 5.10. A zero flow source on a **1**-junction effectively removes that degree of freedom, while zero effort source on a **1**-junction has no effect on the system and can itself be removed from the bond graph. Bond graph simplification rules dictate that any **0** or **1**-junctions not directly bonded to any elements may be removed and adjacent junctions of the same type may be combined. These rules can be invoked to combine the **1**-junctions for dw_1/dt and dw_2/dt after which the values of their inertial **I** elements can be added in series to produce a single degree of freedom with mass M_1. Similar reasoning combines the transverse inertial elements in the rotated coordinate system.

Finally, this model can be coupled to the electrical domain in the same

way as the one-dimensional axial model shown in Fig. 5.7. The resulting, simplified, complete bond graph for the system (henceforth referred to as Model 2) is shown in Figs. 5.11. The mechanical form of Model 2 is much the same as that depicted in Fig. 5.9, with an added spring and force representing the transformed capacitance and applied voltage, respectively. The equivalent circuit for Model 2 is shown in Fig. 5.12.

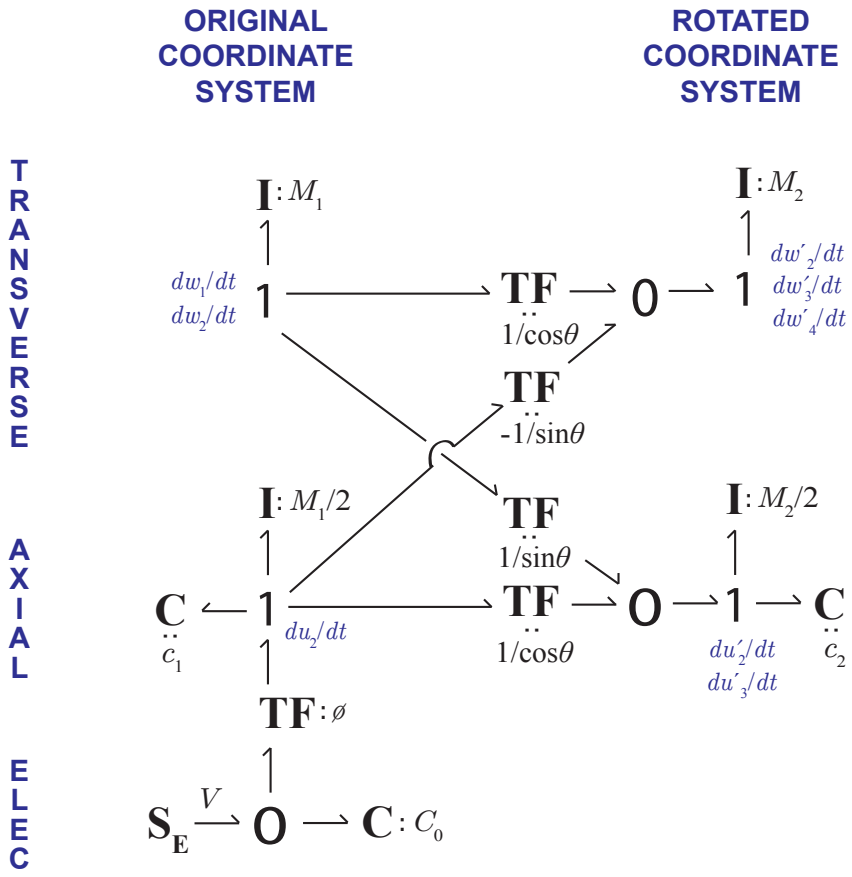

Figure 5.11: Reduced bond graph of 2D axial model with electrical domain.

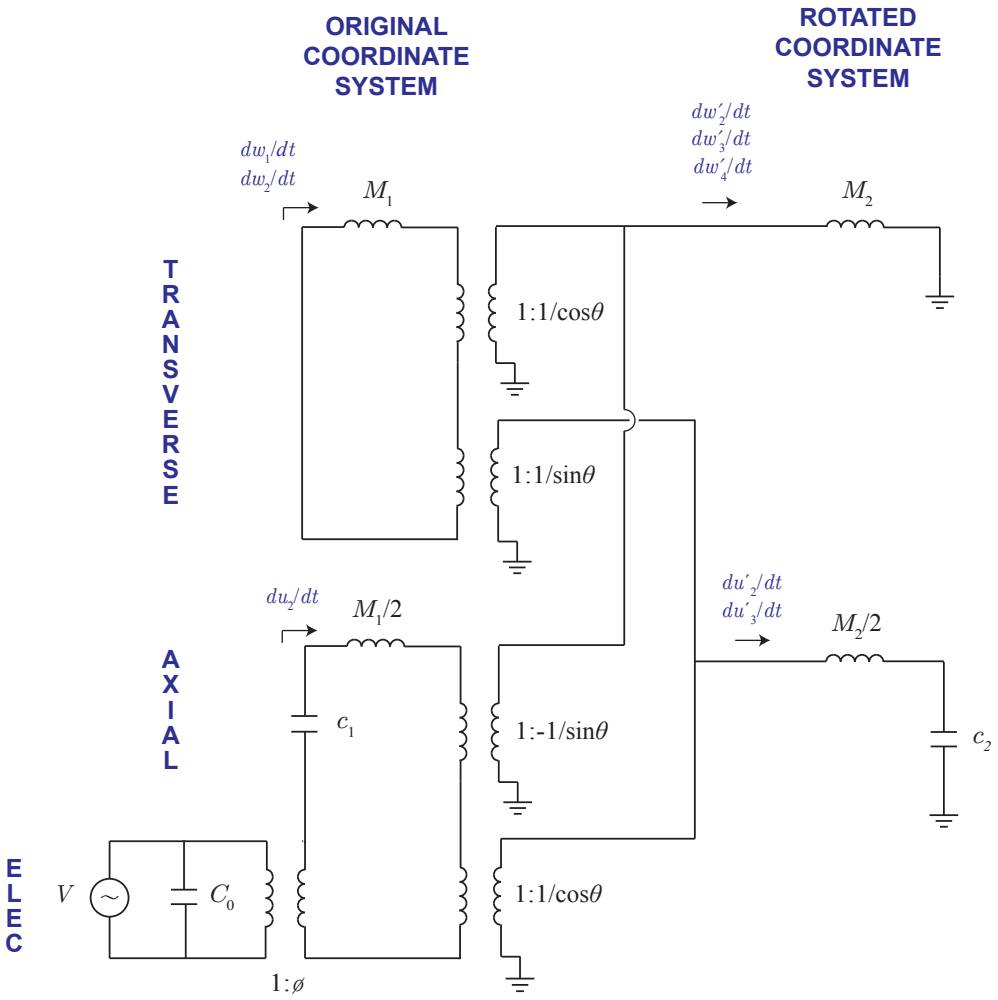

Figure 5.12: Equivalent circuit of 2D axial model with electrical domain.

5.3.2 Model 2 Analysis

Fig. 5.13 shows the full bond graph for Model 2 annotated with causal strokes to facilitate the identification of states of the system. Additionally, each bond has been numbered for convenient referencing. Bonds with independent causality (shown in green) represent states, while those with dependent causality (shown in red) do not. For the following analysis, a generalized momentum state on the i^{th} bond will be represented by p_i while the generalized displacement on the same will be represented by q_i.

From the figure it can be seen that the system has four independent states (or two degrees of freedom) that can be solved for using standard techniques described in Karnopp and Margolis [18]. The three dependent states create algebraic loops that can make writing the state equations somewhat unwieldy. For this reason we define the following constants which will be used in writing the state equations:

$$\gamma_1 = 1 + \frac{M_2}{M_1}\cos^2\theta + 2\frac{M_2}{M_1}\sin^2\theta, \tag{5.13}$$

$$\gamma_2 = 1 + \frac{M_2}{M_1}\cos^2\theta + \frac{1}{2}\frac{M_2}{M_1}\sin^2\theta, \tag{5.14}$$

$$\gamma_3 = \frac{M_2}{M_1}\sin\theta\cos\theta, \tag{5.15}$$

and

$$\Gamma = 1 - \frac{\gamma_1^3}{2\gamma_1\gamma_2}. \tag{5.16}$$

Defining matrices

$$\mathbf{x} = \begin{Bmatrix} q_5 \\ q_{15} \\ p_6 \\ p_{16} \end{Bmatrix}, \tag{5.17}$$

$$\mathbf{d} = \begin{Bmatrix} 0 \\ 0 \\ \frac{1}{\gamma_1 \Gamma} N \\ \frac{\gamma_3}{\gamma_1 \gamma_2 \Gamma} N \end{Bmatrix} V, \tag{5.18}$$

and

$$\mathbf{A} = \begin{bmatrix} 0 & 0 & \frac{2}{M_1} & 0 \\ 0 & 0 & \frac{2\cos\theta}{M_1} & \frac{\sin\theta}{M_1} \\ -\frac{1}{\gamma_1 \Gamma c_1} & -\frac{1}{\gamma_1 \Gamma c_2}\left(\cos\theta + \frac{\gamma_3}{\gamma_2}\sin\theta\right) & 0 & 0 \\ -\frac{\gamma_3}{\gamma_1 \gamma_2 \Gamma c_1} & -\frac{1}{\gamma_2 \Gamma c_2}\left(\frac{\gamma_3}{\gamma_1}\cos\theta + \sin\theta\right) & 0 & 0 \end{bmatrix}, \tag{5.19}$$

the state equations for the four states of the system (q_5, q_{15}, p_6, and p_{16}) can be represented by the following matrix equation:

$$\dot{\mathbf{x}} = \mathbf{A}\mathbf{x} + \mathbf{d}, \tag{5.20}$$

where the dot notation indicates a time derivative of the state. Assuming time-harmonic input, Eq. (5.20) can be written as $s\mathbf{x} = \mathbf{A}\mathbf{x} + \mathbf{d}$ (where $s = j\omega$ is the assumed exponent of the exponential form of the time-harmonic input) or finally, as

$$\mathbf{F}\mathbf{x} = \mathbf{d}, \tag{5.21}$$

where $\mathbf{F} = s\mathbf{I} - \mathbf{A}$ with $\mathbf{I}$ as an identity matrix. Equation (5.21) can be solved for each element of $\mathbf{x}$ using Cramer's Rule:

$$x_i = \frac{\det \mathbf{F}^{(i)}}{\det \mathbf{F}}, \tag{5.22}$$

where x_i is the amplitude of the i^{th} state variable and $\mathbf{F^{(i)}}$ is the matrix $\mathbf{F}$ with $\mathbf{d}$ replacing the i^{th} column.

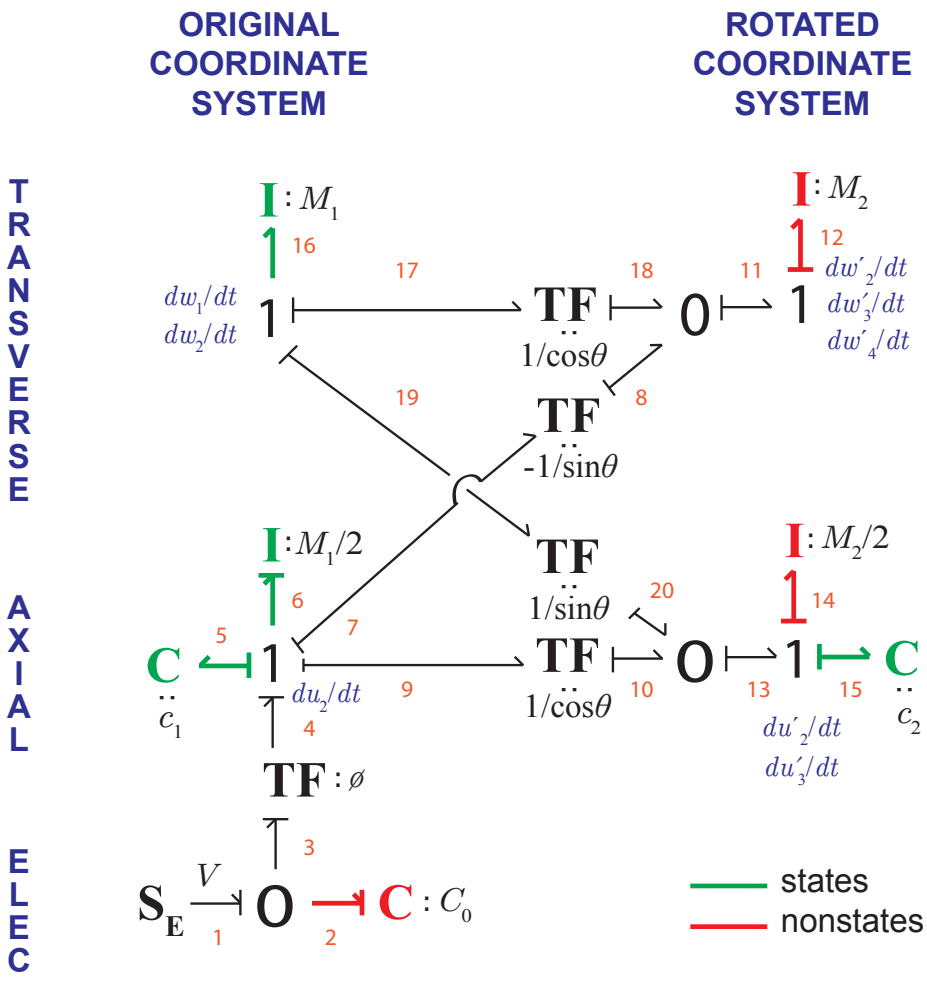

Figure 5.13: Annotated bond graph of 2D axial model with electrical domain.

All results for Model 2 in this section are compared with the results from Model 1, described in Section 3.1, and the finite-element model, described

in Section 4.2.

5.3.2.1 Input Admittance

The input admittance of the system is given by $Y_{\text{in}} = i/V$, where V is the applied voltage and i is the resulting current. The flows at the **0**-junction where the voltage is applied sum to zero according to bond graph convention. Thus, according to the power flow indicated by the arrows on the bonds,

$$f_1 = f_2 + f_3, \tag{5.23}$$

where f_i is used to represent the generalized flow at the ith bond. The flow f_1 is the current i, f_2 is the time derivative of the displacement at bond 2, that is, $f_2 = \dot{q_2}$. Likewise, the flow f_3 is determined by the transformed generalized momentum state at bond 6, thus $f_3 = 2\phi/M_1 p_6$. Thus the admittance can be written in terms of the generalized displacements and momenta of the system as

$$Y_{\text{in}} = \frac{\dot{q_2} + \frac{2\phi}{M_1} p_6}{V}. \tag{5.24}$$

The (electric) displacement q_2 is not a state of the system, but is given by $q_2 = C_0 V$ and, assuming a time-harmonic input voltage, its time derivative can be written as $\dot{q_2} = sC_0V$. The input admittance can thus be written as

$$Y_{\text{in}} = \frac{sC_0V + \frac{2\phi}{M_1} p_6}{V}, \tag{5.25}$$

where p_6 can be found by solving Eq. (5.22) with $i = 3$. The resulting expression for the input admittance is too complicated to show analytically, though a

numerical solution can easily be found for given material properties. Fig. 5.14 is a plot of the input admittance of this model (Model 2) using material properties values given by Appendix A, along with the same given by Model 1 and the FEM COMSOL model.

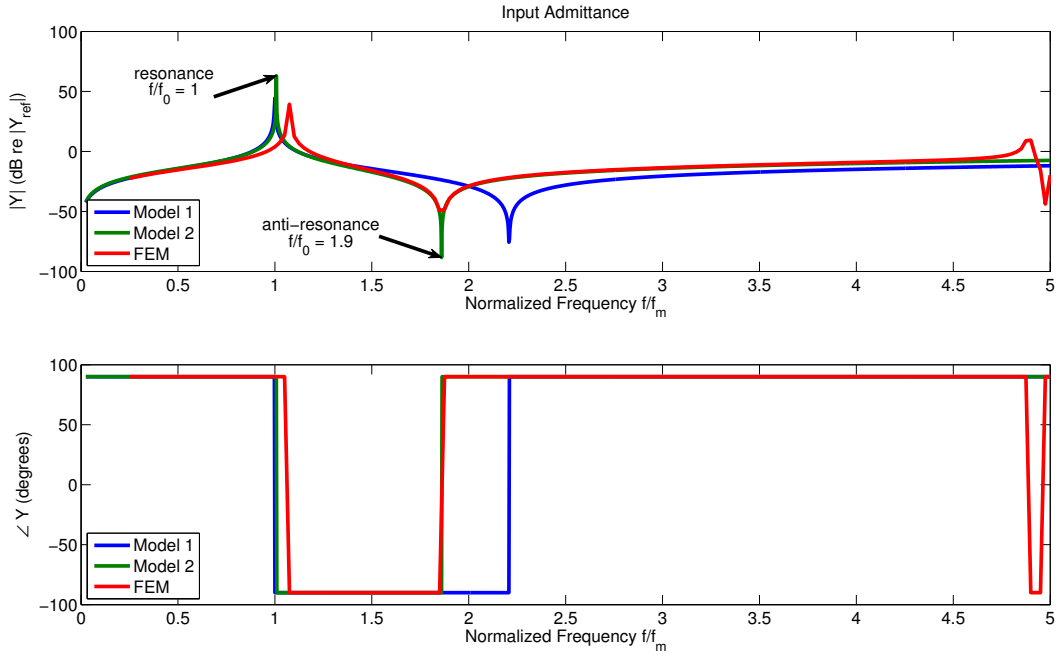

Figure 5.14: Input electrical admittance as given by Model 3, compared with that of Model 1 and an FEM COMSOL model.

It can be seen from the figure that Model 2 is in good agreement with Model 1 for the lower frequencies and around the resonance (the peak of the admittance curve at $f/f_0 = 1$) and starts to deviate from Model 1 around the anti-resonance (the minimum of the admittance curve at $f/f_0 = 1.9$). As described in Section 2.4.1, the resonance and anti-resonance frequency of a transducer can be used to determine the electromechanical coupling coefficient

k, which is a measure of the transducer's transduction efficiency. Model 2 predicts a lower frequency anti-resonance, and thus a less efficient transducer, which is more consistent with experimental and finite-element data than the idealized Model 1. This is primarily due to the geometry of each model—a ring composed of sections of rectilinear staves (as in Model 2) will necessarily have a less efficient mechanical response than that of a composite ring that is purely cylindrical (as in Model 1).

5.3.2.2 Average Radial Velocity

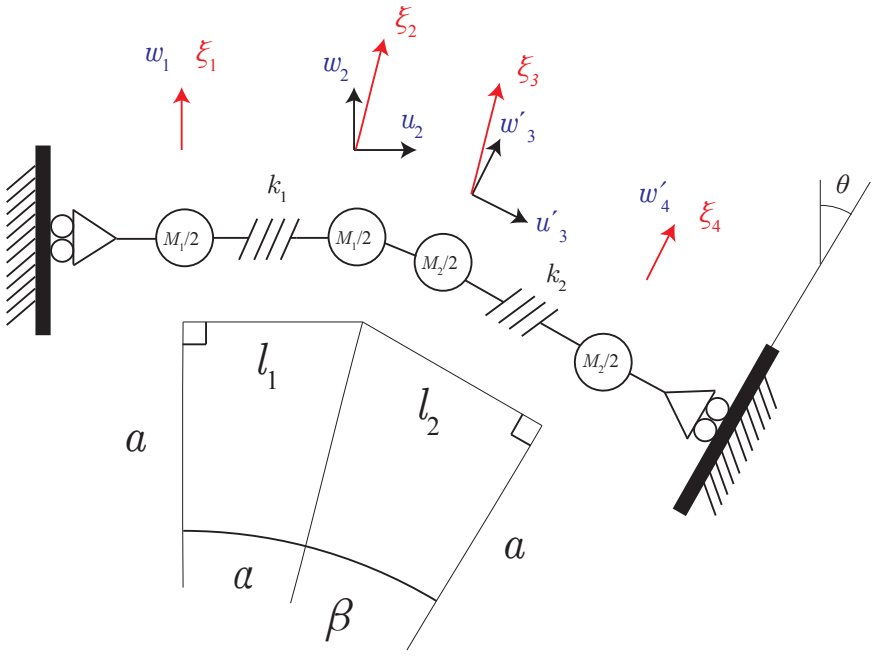

Figure 5.15: Radial displacements.

The average radial velocity is a metric indicating the potential of the

transducer to radiate acoustic energy. It can be determined through ξ_i, the radial displacement of the i^{th} mass, as shown in Fig. 5.15. Inspection of the figure reveals the following geometric relations:

$$\xi_1 = w_1, \tag{5.26}$$

$$\xi_2 = u_2 \sin\alpha + w_2 \cos\alpha, \tag{5.27}$$

$$\xi_3 = w_3' \cos\beta - u_3' \sin\beta, \tag{5.28}$$

and

$$\xi_4 = w_4', \tag{5.29}$$

with $\alpha = \arctan\left(\frac{l_1}{a}\right)$ and $\beta = \arctan\left(\frac{l_2}{a}\right)$.

The radial velocity at each point mass is the time derivative of the radial displacement and can be written in terms of the generalized momenta of the system by using the following relations, as indicated in the bond graph shown in Fig. 5.13:

$$\dot{w_1} = \frac{1}{M_1} p_{16}, \tag{5.30}$$

$$\dot{u_2} = \frac{2}{M_1} p_6, \tag{5.31}$$

$$\dot{w_2} = \frac{1}{M_1} p_{16}, \tag{5.32}$$

$$\dot{u_3'} = \frac{2}{M_2} p_{14}, \tag{5.33}$$

$$\dot{w_3'} = \frac{1}{M_2} p_{12}, \tag{5.34}$$

and (5.35)

$$\dot{w_4'} = \frac{1}{M_2} p_{12}. \tag{5.36}$$

Momenta p_6 and p_{16} are states of the system and can be solved for using Eq. (5.22). Momenta p_{12} and p_{14} are not states but can be written in terms of the states with the following relations:

$$p_{14} = \left(\frac{M_2}{M_1}\cos\theta\right) p_6 + \left(\frac{M_2}{2M_1}\sin\theta\right) p_{16} \tag{5.37}$$

$$p_{12} = \left(\frac{M_2}{M_1}\cos\theta\right) p_{16} - \left(\frac{2M_2}{M_1}\sin\theta\right) p_6 \tag{5.38}$$

Finally, the average radial velocity is estimated by the numerical average of the time-derivative of the radial displacements:

$$\bar{v_r} = \frac{\dot{\xi_1} + \dot{\xi_2} + \dot{\xi_3} + \dot{\xi_4}}{4}, \tag{5.39}$$

where the overbar is used to indicate an average.

A plot of the average radial velocity for this model (Model 2), using material properties values given by Appendix A, along with the same given by Model 1 and the FEM COMSOL model, is shown in Fig. 5.14. It can be seen that the average radial velocity given by Model 2 is in very good agreement with the results from Model 1. The resonance appearing around $f/f_0 = 4.9$ in the radial velocity given by the FEM model does not occur in that given by Model 2, as this resonance is associated with bending effects that Model 2 does not account for. The following section incorporates bending effects in Model 2 in order to capture this resonance.

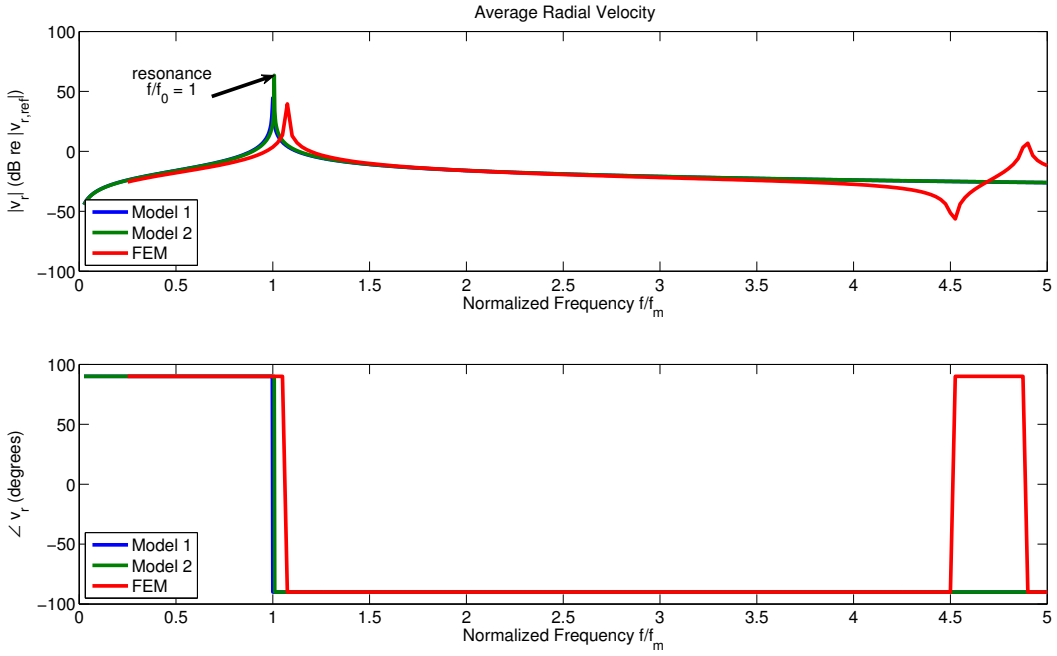

Figure 5.16: Average radial velocity as given by Model 3, compared with that of Model 1 and an FEM COMSOL model.

5.3.3 Model 3: Two-Dimensional Axial Model with Nonzero Angle and Bending

The model being developed here ultimately aims to capture the secondary bending resonance observed in finite element modeling, therefore the final step is to capture the effects of element bending on the dynamic behavior of the cylinder. Appendix B discusses the mechanical schematic, equivalent circuit, and bond graph for a bending beam, including modifications that allow for plate-like and Timoshenko bending effects. The results of Appendix B are used here with each element depicted in Fig. 5.1 modeled as an Euler-Bernoulli beam composed of two lumps, with bending stiffness given by that

of an orthotropic plate (EI is replaced by Eq. B.15 in defining the bending stiffness c_b for each element). It should be noted that while a two lump beam model for each element is used here, an arbitrary number of lumps could be used to model the bending elements if a higher frequency operating band is required.

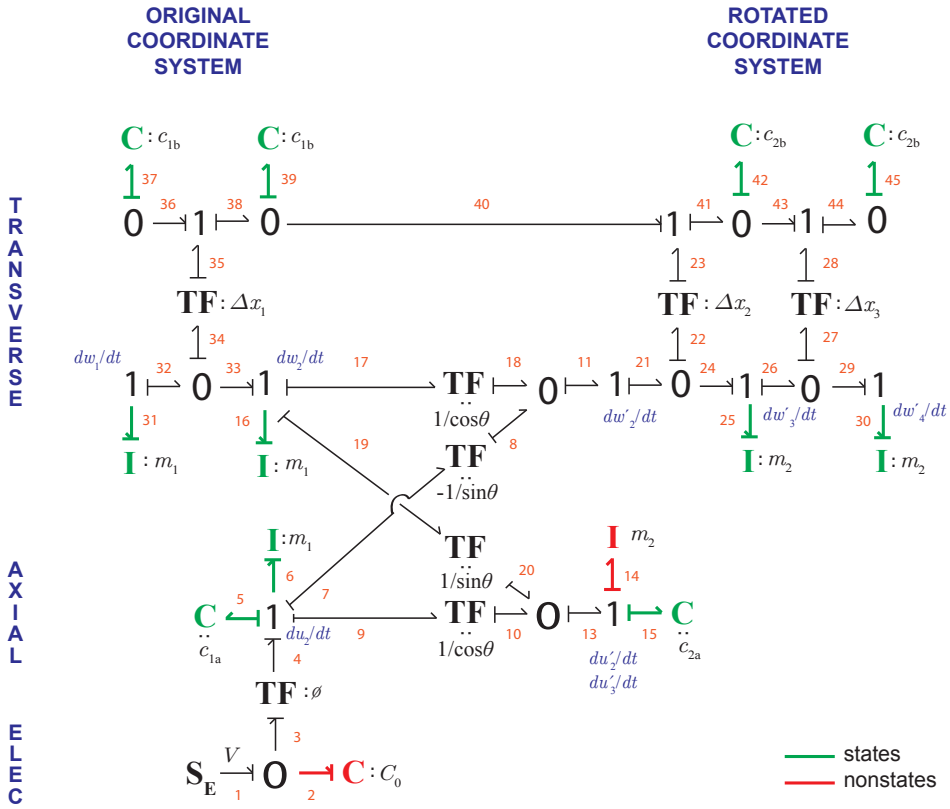

Figure 5.17: Model 3 bond graph.

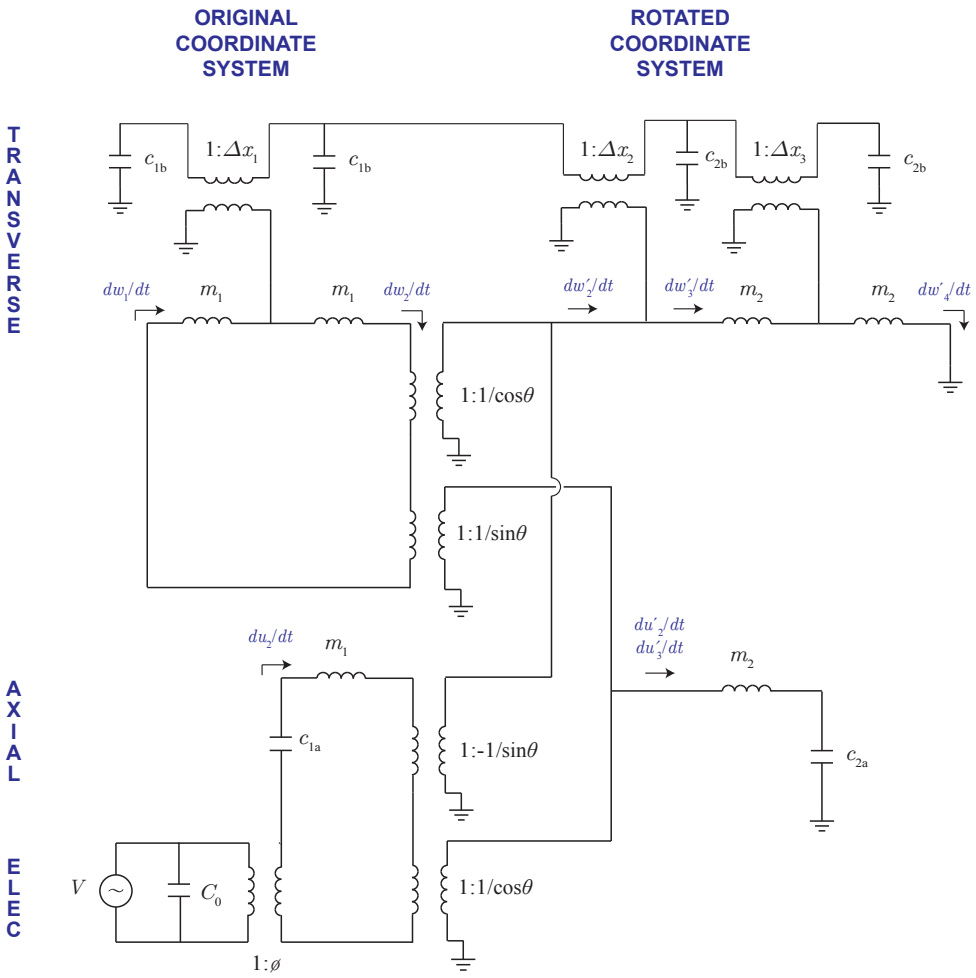

Figure 5.18: Model 3 equivalent circuit.

The bond graph shown in Fig. 5.13 can be augmented to account for bending as shown in Fig. 5.17. This represents the full multi-degree-of-freedom model for our ring transducer system, referred to here as "Model 3". Power bonds to elements representing states of the system are shown in green while those that are not are shown in red. Fig. 5.18 depicts the equivalent circuit for Model 3.

For convenience, the inertial and compliance parameters, as well as the transformer turns ratios, are listed in Table 5.1. The three Δx transformer

Table 5.1: Model 3 Parameters

$m_1 = \rho_1 A_1 \Delta x$	$c_{1a} = \frac{l_1}{E_1 A_1}$	$c_{1b} = \frac{\Delta x_1}{E_1 I_1}$	$\Delta x_1 = \frac{l_1}{2}$
$m_2 = \rho_2 A_2 \Delta x$	$c_{2a} = \frac{l_2}{E_2 A_2}$	$c_{2b} = \frac{\Delta x_2}{E_2 I_2}$	$\Delta x_2 = \frac{l_2}{2}$
$\phi = \frac{2\pi H d_{31}}{s_{11}^E}$	$C_0 = \frac{2\pi a H \epsilon_{33}^S}{t}$	$\theta = \frac{2\pi}{N}$	$\Delta x_3 = \frac{\Delta x_1 + \Delta x_2}{2}$

turns ratios are distinguished by subscripts to allow for different lengths of active and inactive elements. In the following analysis, it is assumed for the sake of simplicity that $\Delta x_1 = \Delta x_2 = \Delta x_3 = \Delta x$, that is, the active and inactive elements are equal in length. While each of the element halves in the reduced model (active and inactive) are lumped into two degrees of freedom each for modeling the axial and transverse motion, the bond graph shown in Fig. 5.17 can easily be modified to include as many degrees of freedom for axial and/or transverse motion as necessary for the desired frequency range. The model shown here is the simplest possible that still captures the desired

phenomena.

The dependent causality (at bond 14 and bond 2) complicates the state equations and suggests the adoption of constants similar to those defined in Eqs. (5.13) through (5.16):

$$\gamma_1 = 1 + \frac{m_2}{m_1}\cos^2\theta, \tag{5.40}$$

$$\gamma_2 = 1 + \frac{m_2}{m_1}\sin^2\theta, \tag{5.41}$$

$$\gamma_3 = \frac{m_2}{m_1}\sin\theta\cos\theta, \text{and}$$

$$\Gamma = 1 - \frac{\gamma_1^3}{\gamma_1\gamma_2}. \tag{5.42}$$

It can be seen from the bond graph that the system has 11 states. In

writing the state equations, it is useful to define the matrices

$$\mathbf{x} = \begin{Bmatrix} q_5 \\ q_{15} \\ q_{37} \\ q_{39} \\ p_{31} \\ q_{42} \\ q_{45} \\ p_{30} \\ p_{25} \\ p_6 \\ p_{16} \end{Bmatrix}, \tag{5.43}$$

$$\mathbf{d} = \begin{Bmatrix} 0 \\ 0 \\ 0 \\ 0 \\ 0 \\ 0 \\ 0 \\ 0 \\ 0 \\ \frac{1}{\gamma_1 \Gamma}\phi \\ \frac{\gamma_3}{\gamma_1 \gamma_2 \Gamma}\phi \end{Bmatrix} V, \tag{5.44}$$

and matrix $\mathbf{A}$, an 11×11 matrix of zeros, except for the following entries:

$$
\begin{aligned}
\mathbf{A}(1,10) &= \frac{1}{m_1} & \mathbf{A}(7,9) &= \frac{1}{\Delta x m_2} \\
\mathbf{A}(2,10) &= \frac{\cos\theta}{m_1} & \mathbf{A}(8,6) &= \frac{-1}{\Delta x c_{2\mathrm{b}}} \\
\mathbf{A}(2,11) &= \frac{\sin\theta}{m_1} & \mathbf{A}(8,7) &= \frac{1}{\Delta x c_{2\mathrm{b}}} \\
\mathbf{A}(3,5) &= \frac{-1}{\Delta x m_1} & \mathbf{A}(9,4) &= \frac{-1}{\Delta x c_{1\mathrm{b}}} \\
\mathbf{A}(3,11) &= \frac{1}{\Delta x m_1} & \mathbf{A}(9,6) &= \frac{2}{\Delta x c_{2\mathrm{b}}} \\
\mathbf{A}(4,5) &= \frac{1}{\Delta x m_1} & \mathbf{A}(9,7) &= \frac{-1}{\Delta x c_{2\mathrm{b}}} \\
\mathbf{A}(4,9) &= \frac{1}{\Delta x m_2} & \mathbf{A}(10,1) &= \frac{-1}{\gamma_1 \Gamma c_{1\mathrm{a}}} \\
\mathbf{A}(4,10) &= \frac{\sin\theta}{\Delta x m_1} & \mathbf{A}(10,2) &= \frac{-1}{\gamma_1 \Gamma c_{2\mathrm{a}}} \left(\cos\theta + \frac{\gamma_3}{\gamma_2}\sin\theta\right) \\
\mathbf{A}(4,11) &= \frac{1-\cos\theta}{\Delta x m_1} & \mathbf{A}(10,3) &= \frac{-\gamma_3}{\gamma_1\gamma_2\Gamma\Delta x c_{1\mathrm{b}}} \\
\mathbf{A}(5,3) &= \frac{1}{\Delta x c_{1\mathrm{b}}} & \mathbf{A}(10,4) &= \frac{-1}{\gamma_1\Gamma\Delta x c_{1\mathrm{b}}} \left(\sin\theta - \frac{\gamma_3}{\gamma_2}(\cos\theta + 1)\right) \\
\mathbf{A}(5,4) &= \frac{-1}{\Delta x c_{1\mathrm{b}}} & \mathbf{A}(10,6) &= \frac{1}{\gamma_1\Gamma\Delta x c_{2\mathrm{b}}} \left(\sin\theta - \frac{\gamma_3}{\gamma_2}\cos\theta\right) \\
\mathbf{A}(6,8) &= \frac{1}{\Delta x m_2} & \mathbf{A}(11,1) &= \frac{-\gamma_3}{\gamma_1\gamma_2\Gamma c_{1\mathrm{a}}} \\
\mathbf{A}(6,9) &= \frac{-2}{\Delta x m_2} & \mathbf{A}(11,2) &= \frac{-1}{\gamma_2\Gamma c_{2\mathrm{a}}} \left(\sin\theta - \frac{\gamma_3}{\gamma_1}\cos\theta\right) \\
\mathbf{A}(6,10) &= \frac{-\sin\theta}{\Delta x m_1} & \mathbf{A}(11,3) &= \frac{-1}{\gamma_2\Gamma\Delta x c_{1\mathrm{b}}} \\
\mathbf{A}(6,11) &= \frac{\cos\theta}{\Delta x m_1} & \mathbf{A}(11,4) &= \frac{1}{\gamma_2\Gamma\Delta x c_{1\mathrm{b}}} \left(\cos\theta + 1 - \frac{\gamma_3}{\gamma_1}\sin\theta\right) \\
\mathbf{A}(7,8) &= \frac{-1}{\Delta x m_2} & \mathbf{A}(11,6) &= \frac{-1}{\gamma_2\Gamma\Delta x c_{2\mathrm{b}}} \left(\cos\theta - \frac{\gamma_3}{\gamma_1}\sin\theta\right).
\end{aligned}
\tag{5.45}
$$

The equations of state can then be written using Eq. (5.20) and each state can

be obtained using Eq. (5.22) and the method described in Section 5.3.2.

5.3.3.1 Input Admittance

The input electrical admittance predicted by this model is given by Eq. (5.3.2) after the values of the states are obtained using the process described in Section 5.3.2.1. A plot of the input admittance for Model 3, using material properties given by Appendix A, along with the same given by the one-degree-of-freedom model described in Section 3.1 and the finite-element model described in Section 4.2, is shown in Fig. 5.19. It can be seen from the figure that Model 3 is in better agreement with the finite-element model (which is itself in good agreement with experimental data, as discussed in Chapter 6) than the one-degree-of-freedom Model 1. Like Model 2, Model 3 more accurately captures the anti-resonance (and thus the transduction efficiency) of the transducer. Moreover, the secondary parasitic resonance/anti-resonance due to bending is captured by Model 3, though it appears significantly sharper and at a lower frequency. This is thought to be the result of the slightly different geometries used in Model 3 and the FEM model, as seen by a comparison of Figs. 5.9 and 4.7. In the process of designing a transducer, undesired resonances are often pushed out of the operating band and into higher frequencies, thus the conservative estimate of the frequency of the bending resonance provided by this model may be useful as a design tool.

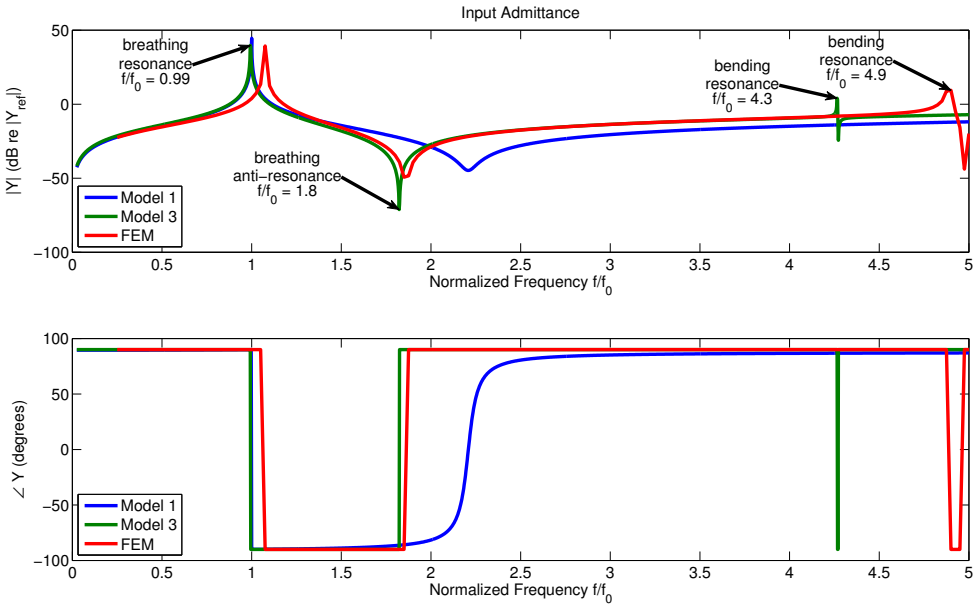

Figure 5.19: Input admittance as given by Model 3, with results from Model 1 and the FEM COMSOL model.

5.3.3.2 Average Radial Velocity

The average radial velocity is found using Eqs. (5.26) through (5.29) and (5.39) as before, however the transverse and axial displacements for Model

3 are given by the following:

$$\dot{w_1} = \frac{1}{m_1} p_{31}, \tag{5.46}$$

$$\dot{u_2} = \frac{1}{m_1} p_6, \tag{5.47}$$

$$\dot{w_2} = \frac{1}{m_1} p_{16}, \tag{5.48}$$

$$\dot{u_3'} = \frac{1}{m_2} p_{15}, \tag{5.49}$$

$$\dot{w_3'} = \frac{1}{m_2} p_{25}, \tag{5.50}$$

and

$$\dot{w_4'} = \frac{1}{m_2} p_{30}. \tag{5.51}$$

Fig. 5.20 compares the average radial velocity predicted by Model 3 using material properties values given by Appendix A, along with the same from the one-degree-of-freedom model described in Section 3.1 and results from the finite-element model discussed in Section 4.2. It can be seen that Model 3 is in good agreement with Model 1 around the primary breathing resonance, occurring at the peak of the radial velocity curve. As designed, Model 3 captures the higher frequency bending resonance that is also seen in the FEM data, though, as in the admittance results, it appears sharper and occurs at a lower frequency.

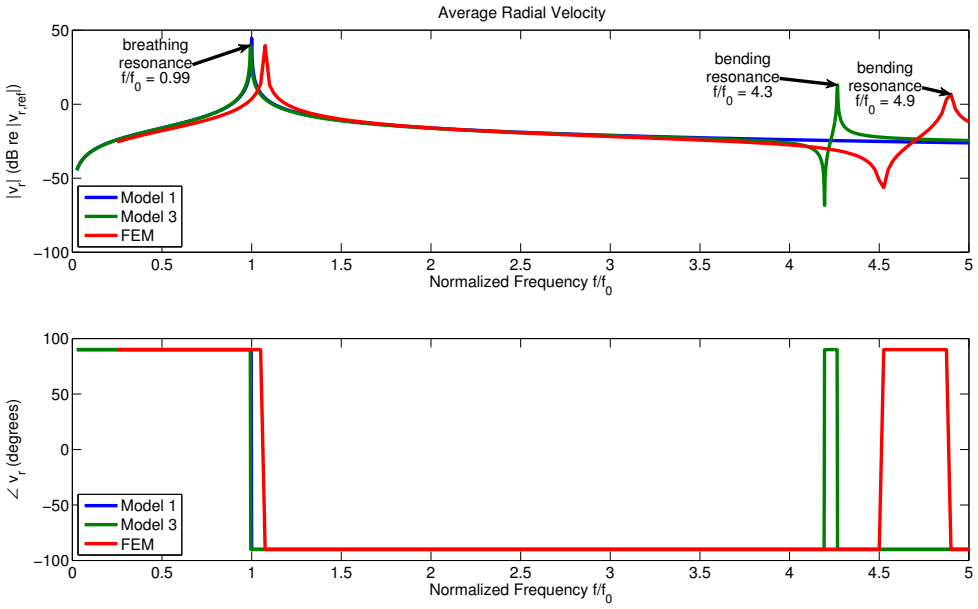

Figure 5.20: Average radial velocity as given by Model 3, with results from Model 1 and the FEM COMSOL model.

5.4 Modifications to Model

As discussed in Section 3.3, the construction of physical transducers of the type discussed here can require significant departures from the idealized models presented above. Some of these modifications, such as filament winding encircling the ring, an internal volume inside the ring, and radiation loading from the external medium, were incorporated into Model 1 in Section 3.3. This section is an attempt to incorporate the same modifications into Model 3. Section 5.4.1 describes a method for including the effects of filament winding around the transducer through an alteration of the material properties used in the model. This approach can be used for any such modification whose

primary effect is to add mass, stiffness, and a small change of geometry to the model. Section 5.4.2 describes a method for including the effects of an internal oil volume and radiation loading. Any such complex impedance operating on specific degrees of freedom of the model can be incorporated in a similar fashion.

5.4.1 Filament Winding Effects

The effects of the filament winding, as discussed in 3.3.1, can be incorporated in this model by altering the Young's modulus, mass, and area moment of inertia of each element. Consider the element stave with winding

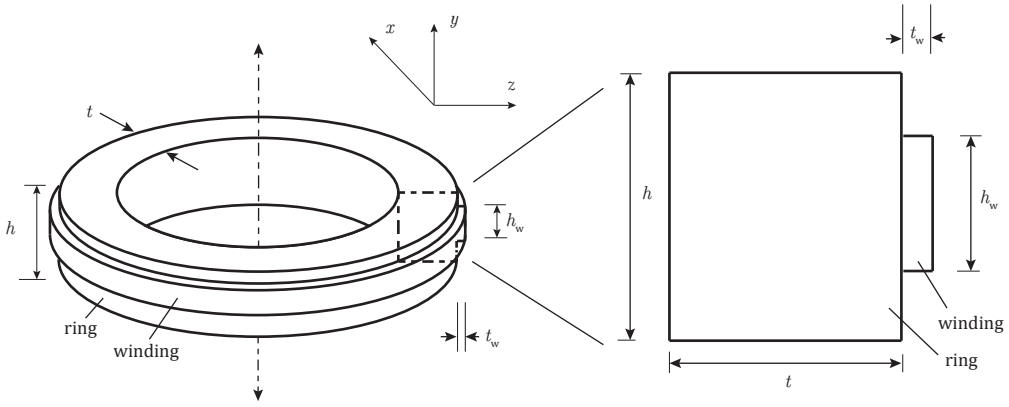

Figure 5.21: Stave with winding.

as shown in Fig. 5.21. As in Section 3.3.1, all winding properties are here subscripted with "w". The effective density ρ^{eff} of such an element is given by the ratio of its total mass to its total volume, that is, $\rho^{\text{eff}} = M_{\text{tot}}/V_{\text{tot}}$. Defining cross-sectional areas for the element and the winding as $A = ht$ and

$A_{\mathrm{w}} = h_{\mathrm{w}} t_{\mathrm{w}}$ respectively, and the total area as $A_{\mathrm{tot}} = A + A_{\mathrm{w}}$, we may write

$$\rho^{\mathrm{eff}} = \frac{\rho_{\mathrm{w}} A_{\mathrm{w}} L + \rho A L}{A_{\mathrm{tot}}}. \tag{5.52}$$

Defining for convenience a winding area fraction $\phi_{\mathrm{w}} = A_{\mathrm{w}}/A_{\mathrm{tot}}$ the effective density may be written as

$$\rho^{\mathrm{eff}} = \phi_{\mathrm{w}} \rho_{\mathrm{w}} + (1 - \phi_{\mathrm{w}}) \rho. \tag{5.53}$$

The effective Young's modulus E^{eff} for the element and winding can be found by considering an applied force F in the x direction on a section of the element and winding. This force will change the total element and winding length L by an amount δL, producing a strain given by $S = \delta L/L$. The total force F is the sum of the products of the stress and cross-sectional area of the element and the winding, that is

$$F = T A_{\mathrm{w}} + T A, \tag{5.54}$$

where T_{w} and T are the stress in the winding and element along the x direction, respectively. These stresses can be written as the product of the appropriate Young's modulus and strain according to Hooke's law, that is,

$$T = E S \tag{5.55}$$

and $T_{\mathrm{w}} = E_{\mathrm{w}} S$, where E denotes a Young's modulus. Using the above, Eq. (5.54) can be written as

$$F = \left(E_{\mathrm{w}} A_{\mathrm{w}} + E A \right) S. \tag{5.56}$$

Dividing both sides of Eq. (5.57) by the total area A_{tot} yields an area averaged stress, that is

$$T^{\text{eff}} = \frac{F}{A_{\text{tot}}} = \left(E_{\text{w}}\phi_{\text{w}} + (1-\phi_{\text{w}})E\right) S. \tag{5.57}$$

A comparison of Eqs. (5.55) and (5.57) indicates that the factor in parenthesis on the right hand side of the equation is an effective Young's modulus for the combined element and winding, that is,

$$E^{\text{eff}} = E_{\text{w}}\phi_{\text{w}} + (1-\phi_{\text{w}})E. \tag{5.58}$$

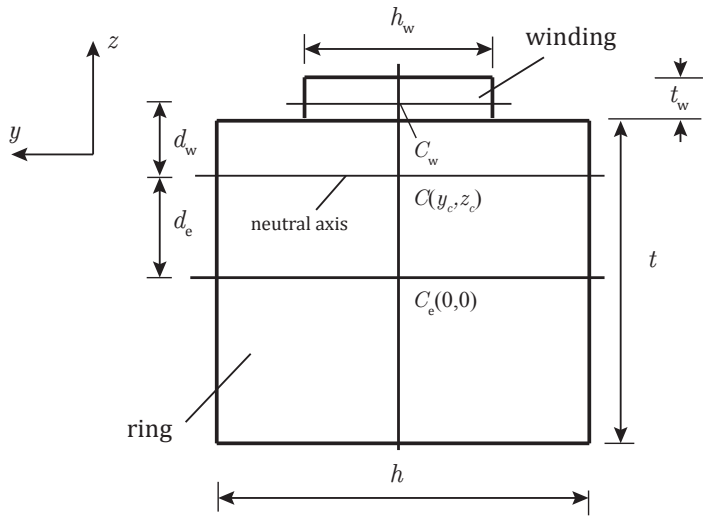

Figure 5.22: Cross section of stave with winding.

Additionally, the added winding will alter the area moment of inertia for the cross section of the element about its neutral axis. By definition, the neutral axis of a beam passes through the centroid of its cross section.

Figure 5.22 depicts a cross section of the element and winding. In order to find the area moment of inertia, the positions of the centroids must be determined. For convenience, the origin C_e of the coordinate system is placed at the centroid of the element, thus its coordinates are given by $y_\mathrm{e} = 0$ and $z_\mathrm{e} = 0$. The centroid C_w of the winding area alone has coordinates $y_\mathrm{w} = 0$ and $z_\mathrm{w} = \frac{1}{2}(t_\mathrm{w} + t)$. Point C with coordinates $(y_\mathrm{c}, z_\mathrm{c})$ is placed at the centroid of the combined beam and winding.

Inspection of the symmetry reveals that $y_\mathrm{c} = 0$. The centroid of a region composed of multiple subregions is the area average of the centroid coordinates for each subregion. Applying this definition to the region shown in Fig. 5.22 yields

$$z_\mathrm{c} = z_\mathrm{w}\frac{A_\mathrm{w}}{A_\mathrm{tot}} + z_\mathrm{e}\frac{A}{A_\mathrm{tot}} = \frac{1}{2}(t_\mathrm{w} + t)\frac{A_\mathrm{w}}{A_\mathrm{tot}} = \frac{1}{2}(t_\mathrm{w} + t)\phi_\mathrm{w}. \tag{5.59}$$

The total area moment of inertia about the neutral axis is given by the sum of the area moments of inertia for the element and winding individually about the neutral axis. These moments of inertia can be found using the parallel axis theorem, which relates the area moment of inertia I (about an axis parallel with the axis passing through the centroid) with I_0, that passes through the centroid. Specifically,

$$I = I_0 + d^2 A, \tag{5.60}$$

where d is the distance between the centroid and the parallel axis and S is the area in question. The distance is given for the element as

$$d_\mathrm{e} = \frac{1}{2}(t_\mathrm{w} + t)\phi_\mathrm{w}, \tag{5.61}$$

and for the winding as

$$d_{\mathrm{w}} = \frac{1}{2}(t_{\mathrm{w}} + t) - \left(\frac{1}{2}(t_{\mathrm{w}} + t)\phi_{\mathrm{w}}\right) = \frac{1}{2}(t_{\mathrm{w}} + t)(1 - \phi_{\mathrm{w}}). \tag{5.62}$$

The area moments of inertia of the element and the winding areas individually about their centroids are given by $I_{0,\mathrm{e}} = \frac{1}{12}ht^3$ and $I_{0,\mathrm{w}} = \frac{1}{12}h_{\mathrm{w}}t_{\mathrm{w}}^3$, respectively. The total effective area moment of inertia for the element and winding is therefore given by

$$\begin{aligned} I^{\mathrm{eff}} &= \frac{1}{12}ht^3 + (\frac{1}{2}(t_{\mathrm{w}} + t)\phi_{\mathrm{w}})^2 ht + \frac{1}{12}h_{\mathrm{w}}t_{\mathrm{w}}^3 + d_{\mathrm{w}}^2 h_{\mathrm{w}}t_{\mathrm{w}} \\ &= \frac{1}{12}ht^3 + (\frac{1}{2}(t_{\mathrm{w}} + t)\phi_{\mathrm{w}})^2 ht + \frac{1}{12}h_{\mathrm{w}}t_{\mathrm{w}}^3 + (\frac{1}{2}(t_{\mathrm{w}} + t)(1 - \phi_{\mathrm{w}}))^2 h_{\mathrm{w}}t_{\mathrm{w}}. \end{aligned} \tag{5.63}$$

The effects of the winding can now be accounted for in Model 3 by replacing ρ, E, and I with ρ^{eff}, E^{eff}, and I^{eff} (with appropriate subscripting for elements 1 and 2) for the parameters given in Table 5.1, respectively.

Plots of the admittance and average radial velocity for Model 3 with winding, using typical winding material properties and thickness (given in Appendix A), are shown in Figs. 5.23 and 5.24 respectively, along with results from Model 1. Additionally, results from a FEM COMSOL model similar to that discussed in Section 4.2 are shown, though this FEM model has a slightly different geometry for the interstitial elements that has the effect of stiffening the system and increasing the frequency at which the resonances occur. For this reason, the bending resonance does not appear in the FEM data in this frequency band. Model 3 slightly underpredicts the frequency at which the

breathing resonance occurs, though overall it can be seen that Model 3 is in significantly better agreement with the FEM data than Model 1.

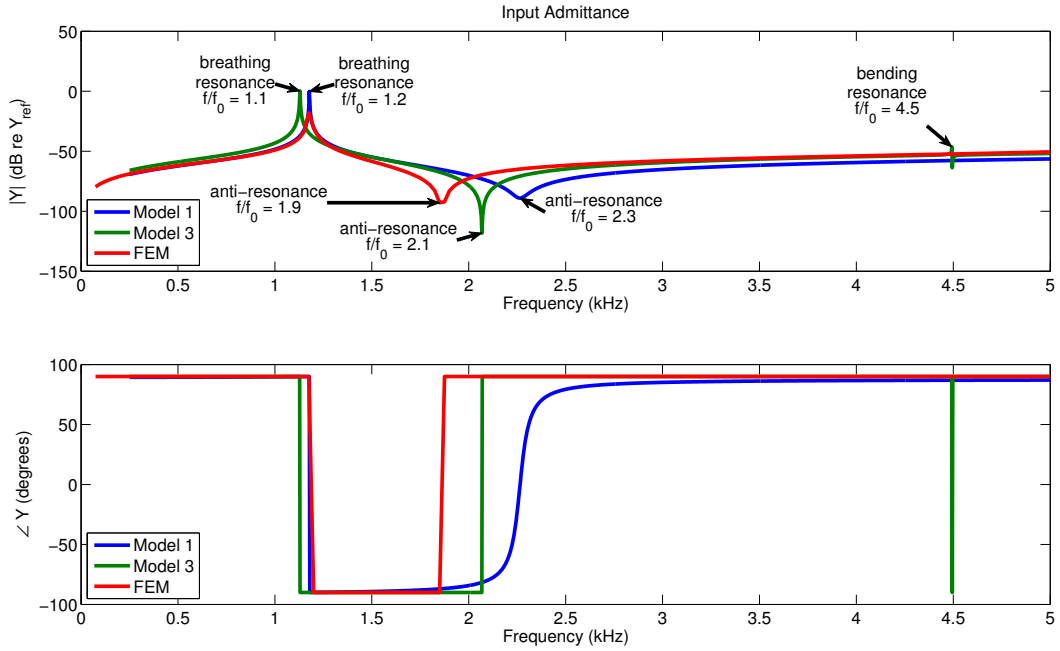

Figure 5.23: Input admittance as given by Model 3 with winding, with results from Model 1 and the FEM COMSOL model.

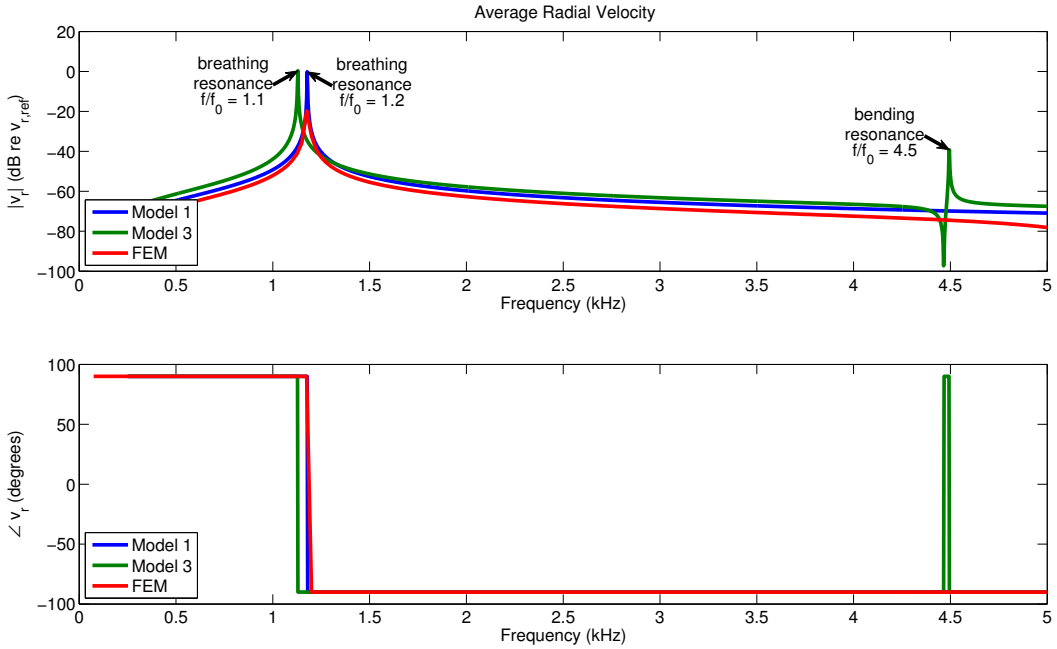

Figure 5.24: Average radial velocity as given by Model 3 with winding, with results from Model 1 and the FEM COMSOL model.

5.4.2 Internal Oil Volume and Radiation Impedance Effects

The impedances due to acoustic radiation and an internal volume, as discussed in Sections 3.3.2 through 3.3.3, are impedances to radial motion, and thus can be placed in line with displacements ξ_1, ξ_2, ξ_3, and ξ_4 as given by Eqs. (5.26) through (5.29) and shown in Fig. 5.15. The transform depicted by Eqs. 5.27 and 5.28 could be represented by a transformer in the bond graph and the equivalent circuit, though for small α and β the sines are approximately zero and the cosines are approximately unity, thus all radial displacements can be approximated by transverse displacements w. Specifically, $\xi_2 \approx w_2$ and $\xi_3 \approx w_3'$. The effects of the radiation impedance and internal oil volume can

then be accounted for by placing a complex, frequency dependent impedance **Z** element on the bonds that represent the flows associated with these displacements, that is, at bonds 31, 16, 25, and 30 in the bond graph representation of Model 3 shown in Fig. 5.17. Figure 5.25 is a partial bond graph of the system augmented with these **Z** elements (shown in blue for clarity).

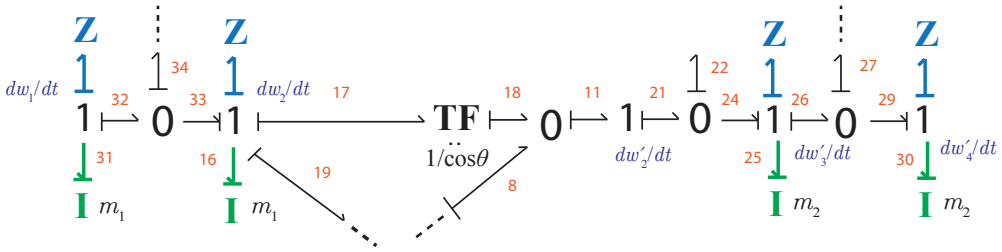

Figure 5.25: Partial bond graph of system with added impedances **Z** due to radiation loading or internal oil volume.

The impedances placed at each of these bonds is given by

$$Z = z_{\text{rad}} + z_{\text{vol}}, \tag{5.64}$$

where z_{rad} and z_{vol} are scaled versions of the impedances discussed in Sections 3.3.2 through 3.3.3, as their effects are distributed amongst the N unit cells and the 4 degrees of freedom within each unit cell. Specifically,

$$z_{\text{vol}} = \frac{Z_{\text{vol}}}{4N}, \tag{5.65}$$

and

$$z_{\text{rad}} = \frac{Z_{\text{rad}}}{4N}, \tag{5.66}$$

where Z_{vol} is given by either Eq. (3.52) or (3.58) and Z_{rad} is given by either Eq. (3.41) or (3.43).

The matrix $\mathbf{A}$ defined in Eq. (5.45) for use in the state equations of the system can be modified to account for these elements as follows:

$$\mathbf{A}(5,5) = \frac{-1}{m_1}(z_{\text{vol}} + z_{\text{rad}}), \tag{5.67}$$

$$\mathbf{A}(8,8) = \frac{-1}{m_2}(z_{\text{vol}} + z_{\text{rad}}), \tag{5.68}$$

$$\mathbf{A}(9,9) = \frac{-1}{m_2}(z_{\text{vol}} + z_{\text{rad}}), \tag{5.69}$$

$$\mathbf{A}(10,11) = \frac{-\gamma_3}{\gamma_1\gamma_2\Gamma m_1}(z_{\text{vol}} + z_{\text{rad}}), \tag{5.70}$$

and

$$\mathbf{A}(11,11) = \frac{-1}{\gamma_2\Gamma m_1}(z_{\text{vol}} + z_{\text{rad}}). \tag{5.71}$$

Sections 5.4.2.1 and 5.4.2.2 present the results of Model 3 when the acoustic domains of the internal oil volume and water medium have been accounted for in the manner described in this section. In all cases, the results of Model 3, using material properties values given by Appendix A, are shown together with the same from Model 1 and the FEM COMSOL model results discussed in Section 4.2.

5.4.2.1 Response of Transducer with Internal Oil Volume

Figs. 5.26 and 5.27 show the admittance and average radial velocity for Model 3, with an internal oil volume impedance obtained using the standing wave model given by Eq. (3.58). It can be seen from the admittance of the

transducer in oil, shown in Fig. 5.26, that Model 3 agrees as well with the FEM data as Model 1 at the primary resonance, and significantly better than Model 1 at the primary anti-resonance, as was observed in the in-air case. Additionally, Model 3 is in better agreement with the FEM results as far as the overall level of the admittance magnitude is concerned. Curiously, the bending resonance does not appear in the admittance given by Model 3, though it is seen clearly in the FEM results. However, it does appear in the radial velocity plot given by Model 3, shown in Fig. 5.27, but at a significantly lower frequency than given by the FEM results. Additionally, the bending resonance appears heavily damped in the results of Model 3 due to the loading from the internal oil volume and as such it is best observed in the phase of the radial velocity.

The difference in the characteristics of the bending resonance exhibited by Model 3 and the FEM model can perhaps be attributed to approximations made in the standing wave impedance model used in Model 3 and given in Section 3.3.3.2. The standing wave impedance model assumes that the motion of the ring has no angle dependance. Near the bending resonance, however, elements along the perimeter of the ring are moving out of phase with one another, thus their motion is dependent on angle position. Model 3, unlike the FEM model, does not account for the resulting change in the impedance of the internal oil volume.

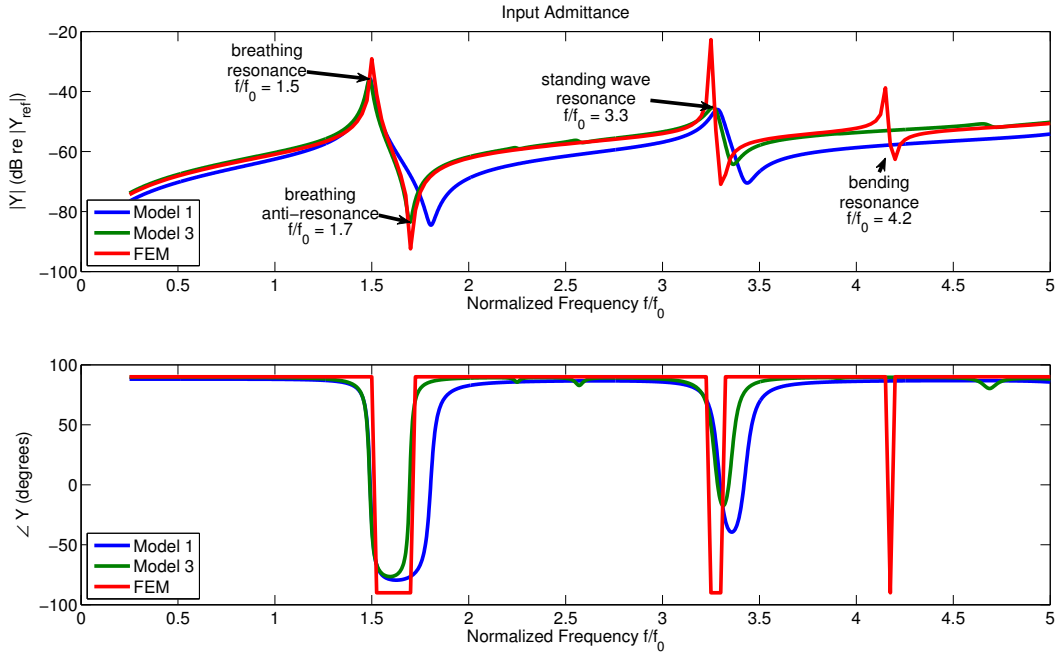

Figure 5.26: Input admittance as given by Model 3 with internal oil volume, with results from Model 1 and the FEM COMSOL model.

5.4.2.2 Response of Transducer with Internal Oil Volume and Radiation Loading

The admittance and average radial velocity as given by Model 3, with an internal oil volume (using the standing wave model given by Eq. (3.58)) and radiation loading (using the finite cylinder model given by Eq. (3.43)), are presented in Figs. 5.28 and 5.29 respectively. The FEM results have been modified to represent the response of a transducer ring subject to the radiation impedance of a finite cylinder, as described in Appendix D. Model 3 and the FEM model are in good agreement at the primary breathing resonance (at $f/f_0 = 1.3$) and the standing wave resonance (at $f/f_0 = 3$). Additionally,

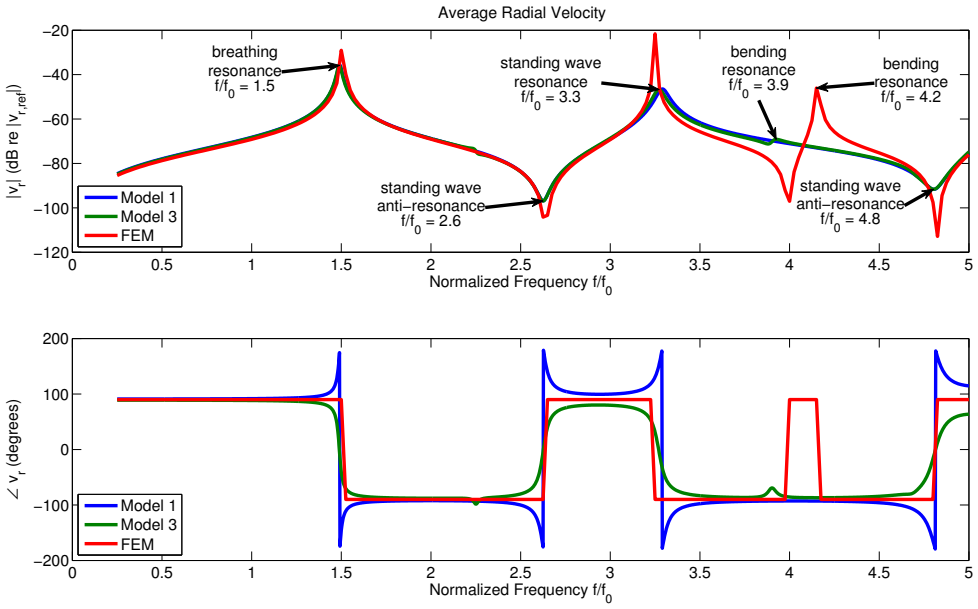

Figure 5.27: Average radial velocity as given by Model 3 with internal oil volume, with results from Model 1 and the FEM COMSOL model.

the level of the admittance magnitude is consistent between them. Model 3, however, does exhibit a spurious resonance at $f/f_0 = 2.6$ that is thought to be a numerical artifact rather than an indication of something physical. Curiously, the bending resonance given by the FEM model appears at a lower frequency, $f/f_0 = 3.6$, than that given by Model 3, at $f/f_0 = 4.7$. This can perhaps be attributed to the approximation in the radiation impedance model given in Section 3.3.2.2. As implemented, this model assumes that the ring is radiating uniformly along its perimeter. Near the bending resonance, the elements are moving out of phase with one another and the perimeter of the ring is no longer circular. In the finite element model, the radiation impedance is allowed to change to reflect this phenomenon, and as a result becomes more

mass-like near the bending resonance where the element staves are sloshing water around between them.

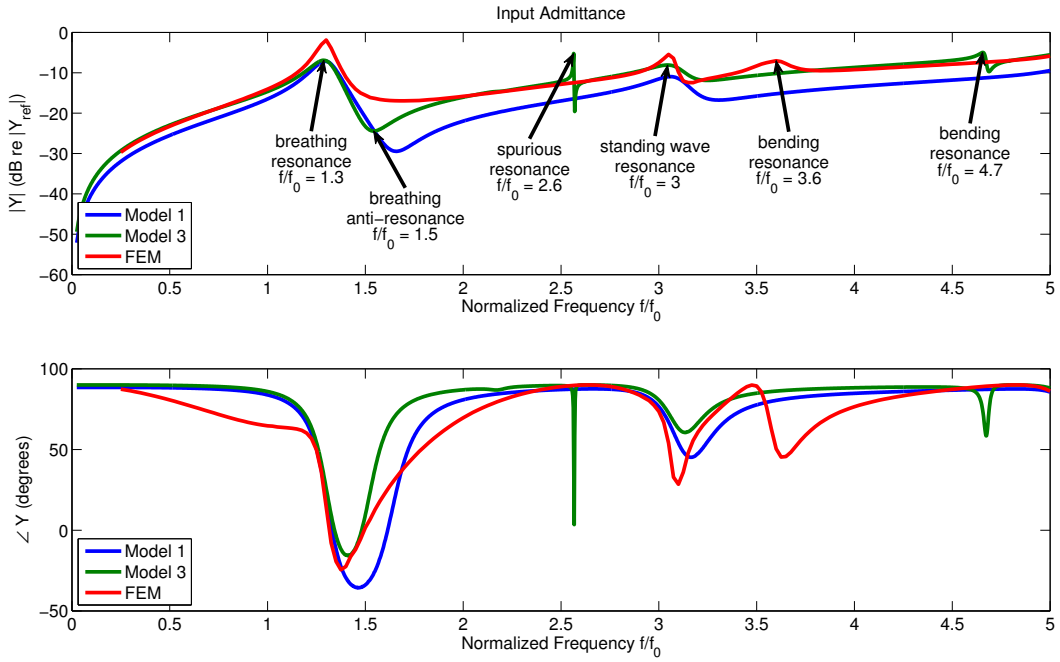

Figure 5.28: Input admittance as given by Model 3 with internal oil volume and radiation loading, with results from Model 1 and the FEM COMSOL model.

The average radial velocity given by Model 3 is nearly identical to that given by Model 1, as shown in Fig. 5.29. This suggests that the radiation impedance is dominating over other effects that distinguish the models. The key distinction between the models is the bending resonance exhibited by Model 3, at around $f/f_0 = 4.7$, though it appears significantly damped. The radial velocity from the FEM model follows the curves of Model 1 and Model 3, with the exception that the bending resonance appears significantly stronger

and at a lower frequency than that given by Model 3. This is thought to be due to the nature of the radiation impedance model as described above.

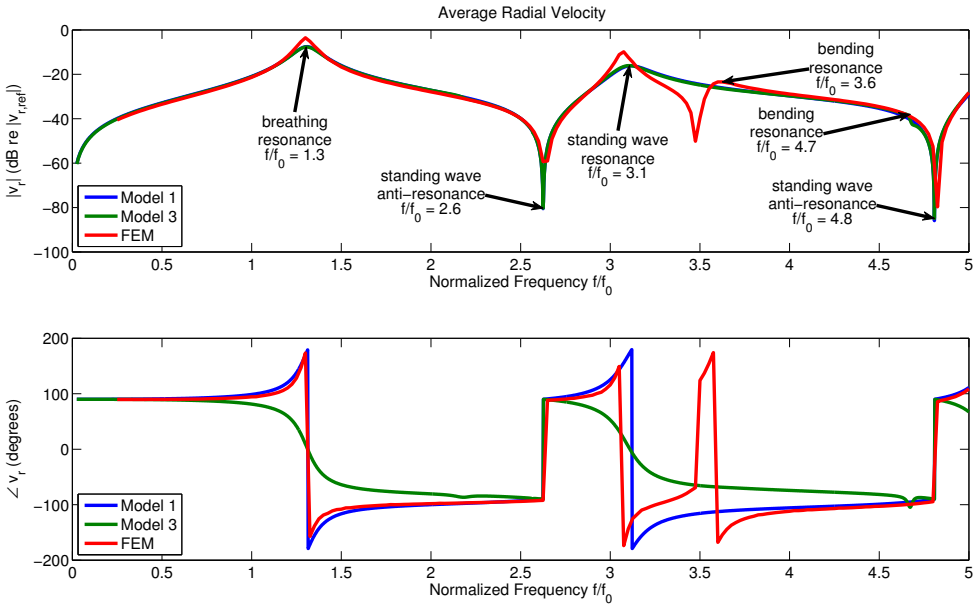

Figure 5.29: Average radial velocity as given by Model 3 with internal oil volume and radiation loading, with results from Model 1 and the FEM COMSOL model.

5.4.2.3 Transmit Voltage Response

As described in Section 2.4.3, the transmit voltage response (TVR) of a transducer is the pressure-to-voltage transfer function, scaled at a distance of 1 meter, when the transducer is deployed underwater. If the transducer is modeled as a simple source, the average radial velocity can be used to determine the TVR using Eqs. (2.34) through (2.36). Using this method, the TVR given by Model 3 is plotted in Fig. 5.30, along with that of Model 1 and the FEM model. An internal oil volume and radiation impedance due to water loading is accounted for in each model. As the TVR of a simple source is a frequency weighted, scaled version of the average radial velocity, all of the analysis given for Fig. 5.29 applies.

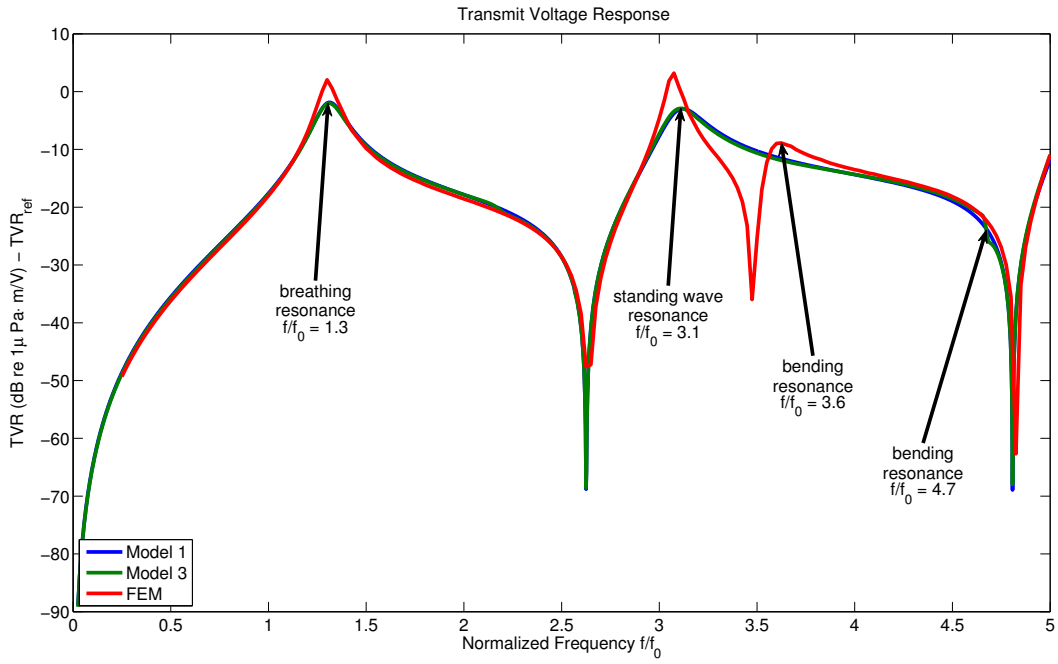

Figure 5.30: Transmit voltage response as given by Model 3 with internal oil volume and radiation loading, with results from Model 1 and FEM.

5.4.3 Summary of Modification Effects

A summary of the effects of modifications to Model 3 are presented in Table 5.2. The primary breathing resonance, breathing anti-resonance, standing wave resonance, and bending resonance frequencies are presented for each case indicated.

Table 5.2: Effect of Modifications to Model 3 on Resonances of Interest

	Breathing Resonance f/f_0	Breathing Anti-Resonance f/f_0	Standing Wave Resonance f/f_0	Bending Resonance f/f_0
In-Air	0.99	1.8	-	4.3
Winding (5 Layers)	1.1	2.1	-	4.5
Oil Volume	1.5	1.7	3.3	4.2
Oil Volume and Radiation Loading	1.3	1.5	3	4.7

5.5 Nonlinear Effects

If the transducer is driven by a sufficiently large voltage, the stave elements can undergo deformations with amplitudes high enough for nonlinear effects to be observed. One such nonlinearity is observed in the experimentally measured total harmonic distortion data described in Section 6.5. The harmonic distortion increases with applied voltage around the bending resonance frequency, indicating that the nonlinearity has origins in the bending mechanism.

This nonlinearity can be accounted for in Model 3 by using the method described in Appendix B.2.2. Specifically, the nonlinearity is accounted for by modifying the compliances of the $\mathbf{C}$ elements on bonds 37, 39, 42, and 45 in Fig. 5.17 as follows:

$$\text{bond 37: } c_{1\text{b}} \rightarrow c_{1\text{b1}} = \frac{c_{1\text{b}}}{1 + \frac{1}{3}q_{37}^2} \tag{5.72}$$

$$\text{bond 39: } c_{1\text{b}} \rightarrow c_{1\text{b2}} = \frac{c_{1\text{b}}}{1 + \frac{1}{3}q_{39}^2} \tag{5.73}$$

$$\text{bond 42: } c_{2\text{b}} \rightarrow c_{2\text{b1}} = \frac{c_{2\text{b}}}{1 + \frac{1}{3}q_{42}^2} \tag{5.74}$$

$$\text{bond 45: } c_{2\text{b}} \rightarrow c_{2\text{b2}} = \frac{c_{2\text{b}}}{1 + \frac{1}{3}q_{45}^2}. \tag{5.75}$$

A simulation of nonlinear effects in Model 3 is outside the scope of this thesis and is suggested as future work.

5.6 Conclusions

A lumped parameter, MDOF model for a segmented 31-mode ring transducer has been developed that captures important effects neglected by a 1-DOF model of the same. In particular, a resonance due to bending in the elemental staves is captured by the MDOF model, though at a lower frequency than is seen in an FEM model. As this resonance is parasitic, it is desirable to capture it in a relatively simple lumped parameter model. Additionally, the MDOF model provides an estimation of the electromechanical efficiency of the transducer that is more consistent with the FEM model than the 1-DOF model is. It has been shown that the MDOF model may be modified

to include effects due to filament winding, internal oil volume, and radiation loading, though the results can differ from that given by the FEM model as a result of the different assumptions made by each for these conditions. The following chapter presents experimental results which will be used to compare the efficacy of the 1-DOF, MDOF, and FEM models in describing the performance of the transducer.

Chapter 6

Measurement of Performance Metrics

The results of the previous chapters regarding the performance of the piezoelectric 31-mode segmented ring transducer are here compared with experimental data taken from tests on constructed ring transducers, with dimensions and material properties as given in Appendix A. The metrics considered here are the electrical impedance, the average radial velocity, and the transmit voltage response (TVR), discussed in Sections 6.2, 6.3, and 6.4, respectively. Additionally, the total harmonic distortion (THD), resulting when the applied voltage is high enough to introduce distortion into the signal, is discussed in Section 6.5. With the exception of THD, the results are compared with lumped parameter models Model 1 and Model 3, described in Chapters 3 and 5 respectively, and the finite element method (FEM) model, described in Section 4.2, in order to evaluate their effectiveness in describing the performance of the transducer. Due to concerns of the project sponsor, all results have been normalized according to the scheme described in Appendix A.

6.1 Transducer Implementation

Ring transducers are typically potted with a urethane overmold in order to increase their durability and stability. Traditionally, the urethane is chosen to have an impedance similar to that of water in order to minimize reflections from the urethane-water boundary when the transducer is submerged underwater. In these experiments, the commercial polyurethane rubber DeSoto PR1547 was used for the overmold, the acoustic and mechanical properties of which have been well-documented [19]. At frequencies where the dimensions of the urethane overmold are much smaller than the wavelength of acoustic waves generated by the transducer, the principle effect of this overmold on the transducer's performance is to add damping and mass to the transducer system. Additionally, the transducer is tested underwater in an assembly that allows it to attach to structures that move it in and out of the water for experimental testing. Like the urethane overmolding, the assembly can influence the performance of the transducer. A schematic of a cross section of the ring with urethane overmold, inside an assembly with oil volume and placed underwater, is shown in Fig. 6.1.

In order to concentrate on the fundamental aspects of the transducer system, the effect of the urethane and assembly are neglected in the lumped parameter models developed in previous chapters. However, when the transducer is tested underwater, it is either in an assembly, overmolded, or both. For this reason, some experimentally derived metrics are expected to deviate from the results of the lumped parameter models that don't account for the ef-

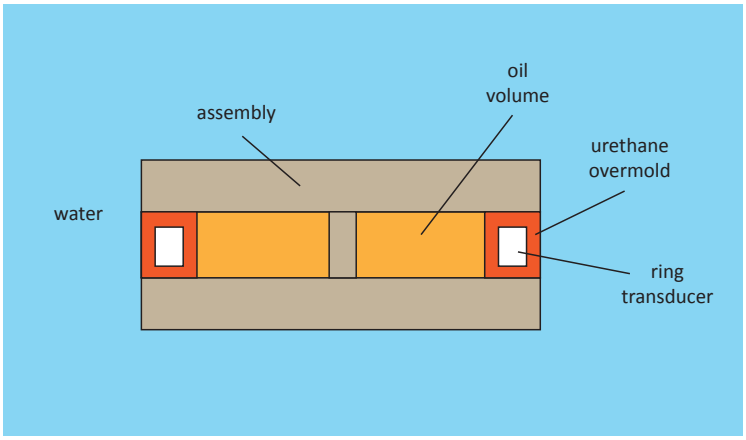

Figure 6.1: Schematic of a cross section of the overmolded ring, inside the assembly, with oil volume, and submerged underwater.

fects of the urethane overmolding or the assembly. A test case for the effects of the overmold is provided by a comparison of the admittance of the transducer ring in air, with and without overmold, presented in the next section.

6.2 Electrical Admittance

The electrical admittance of the transducer is tested with an impedance analyzer that applies a voltage V to the transducer electrodes at frequencies in the band of interest and measures the magnitude and phase (relative to the applied voltage) of the resulting current i. The admittance is then given by $Y = i/V$ and is complex valued to retain magnitude and phase information. In these experiments, a Hewlett-Packard 4192A impedance analyzer was used. Figure 6.2 shows the experimentally captured electrical admittance of the ring transducer under various conditions, defined as follows:

- "In Air": bare (without overmold) transducer, in air.
- "In Air, Assembly": bare (without overmold) transducer within assembly, in air.
- "In Air, OM": overmolded transducer, in air.
- "In Air, Assembly, OM": overmolded transducer within assembly, in air.
- "In Water, Assembly, OM": overmolded transducer within assembly, in water.
- "In Air, Assembly, OM, Oil": overmolded transducer within assembly with internal oil volume, in air.
- "In Water, Assembly, OM, Oil": overmolded transducer within assembly with internal oil volume, in water.

Comparing the results from Fig. 6.2, it can be seen that the electrical response of the transducer is significantly affected by the presence of the urethane molding, internal oil volume, and assembly. The in-air response of the transducer most nearly approximates free (zero force) boundary conditions around the ring with no radiation loading, and thus exhibits sharper primary and secondary resonances. When the transducer is placed inside of the assembly, without any oil, there is no great effect on the response. This is because most of the effects of the assembly are felt through coupling with the oil volume. The urethane overmold dampens both primary and secondary resonances

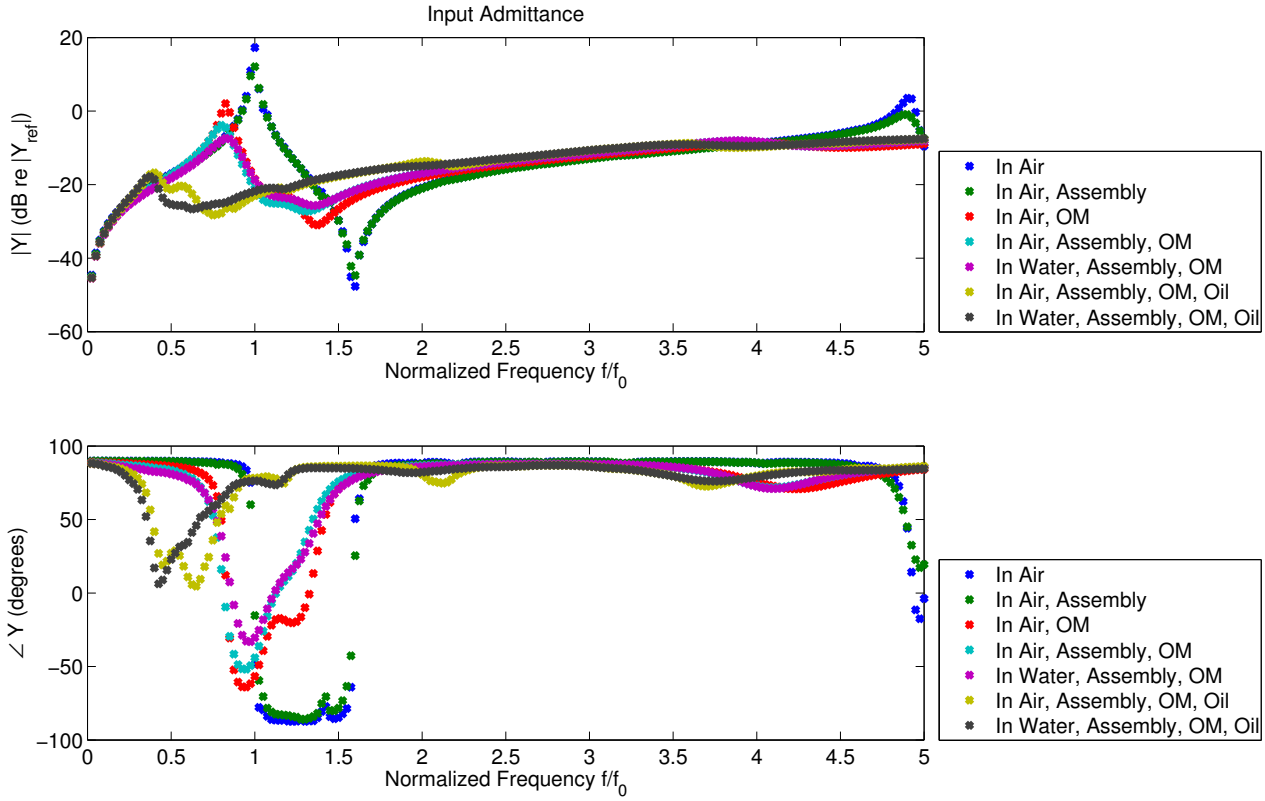

Figure 6.2: Experimentally captured electrical admittance of transducer for various cases.

and decreases the frequencies at which they occur. When the transducer is placed inside the assembly and the internal volume is filled with oil, the transducer is coupled to the assembly in such a way that reduces the resonance frequencies and makes them less pronounced. These results indicate that both the overmolding and the assembly with oil primarily add mass and resistance to the transducer system. Comparing the response of the transducer in air and in water, it can be seen that the radiation loading on the transducer from the water slightly lowers the primary resonance frequency, due to the mass-like ef-

fect of the radiation impedance at low frequencies. Table 6.1 summarizes these results, comparing the primary resonance, bending resonance frequencies, and maximum admittances for each case.

Table 6.1: Comparison of Admittance Data from Experimental Results for Various Cases

	Breathing Resonance f/f_0	Bending Resonance f/f_0	Maximum Admittance $\lvert Y\rvert/\lvert Y_{\text{ref}}\rvert$
"In Air"	1	4.9	17.3
"In Air, Assembly"	1	4.9	17.3
"In Air, OM"	0.83	4.0	2.0
"In Air, Assembly, OM"	0.8	3.9	-3.9
"In Water, Assembly, OM"	0.83	3.9	-7.3
"In Air, Assembly, OM, Oil"	0.4	3.6	-16.8
"In Water, Assembly, OM, Oil"	0.38	3.6	-17.8

The response of the non-overmolded transducer outside of the assembly and without any oil volume is the best case to compare with the lumped parameter models, as neither involve the effects of the urethane overmolding or assembly. Fig. 6.3 compares the admittance of the bare transducer in air with results of the lumped parameter models for the same case. All models capture the fundamental breathing resonance at around $f/f_0 = 1$, in agreement with the experimental data. Model 3, however, provides a better estimate of the anti-resonance of the transducer than Model 1, and thus provides a more realistic estimate of the electromechanical efficiency of the transducer. Model 3 still overpredicts this anti-resonance in comparison to the experimental data, indicating that there are causes of inefficiency in the built transducer that are

not being accounted for in the model. These are likely geometrical, due to misalignment of the elements, and or due to additional compliances in the real system provided by glue joints. It can be seen that the bending resonance appears in the experimental data at $f/f_0 = 4.9$, in good agreement with the FEM model. Model 3 captures this resonance but under predicts the frequency at which it occurs by about 12%. Additionally, the resonance appears significantly more narrow band in Model 3 than it does in the experimental data. It seems reasonable consider this to be primarily a geometric effect, as the geometry of the interstitial elements in the actual constructed device is closer to that of the COMSOL FEM model (shown in Fig. 4.7) than that of Model 3 (shown in Fig. 4.4). These results are summarized in Table 6.2.

Table 6.2: Comparison of in-air admittance data from experimental results and models.

	Breathing Resonance f/f_0	Breathing Anti-Resonance f/f_0	Electro-mechanical Coupling Coefficient k^2	Bending Resonance f/f_0
Model 1	1	2.2	0.79	-
Model 3	1	1.8	0.69	4.3
FEM	1	1.9	0.66	4.9
Experimental	1	1.8	0.61	4.9

The effects of the urethane overmolding on the experimentally measured admittance of the transducer in air are shown in Fig. 6.4. As a demonstration of how the effects of the urethane overmold may be included in the

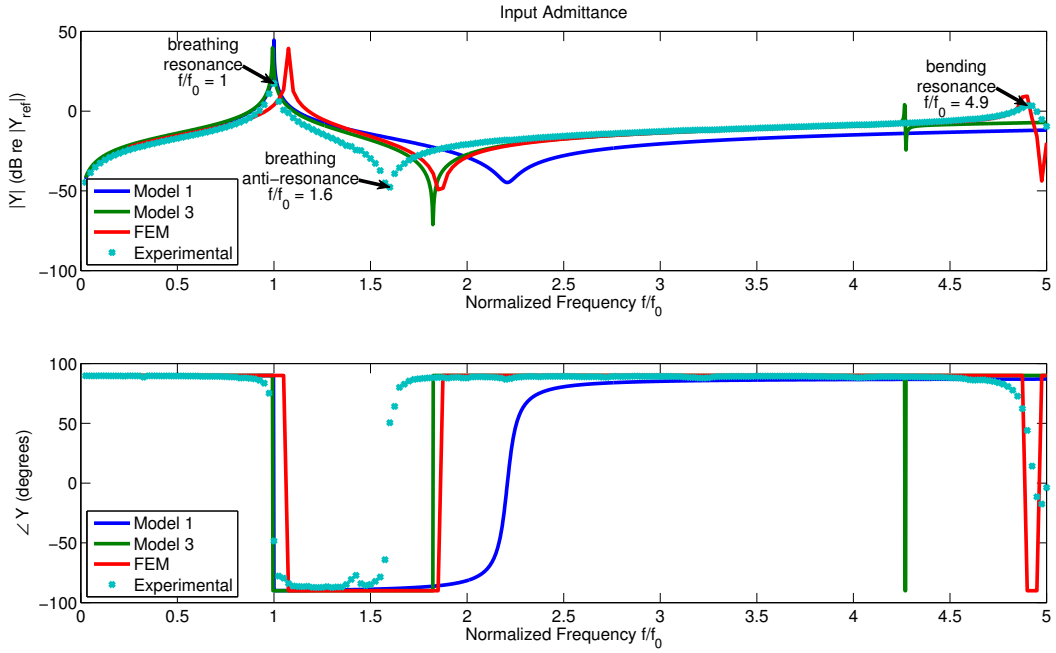

Figure 6.3: Experimentally captured input admittance of transducer in air, compared with lumped element models.

lumped parameter models, the experimental result is compared with that of Model 1 and Model 3, where the urethane overmolding is modeled as a mass M_{ur} equal to 75% of the mass of the transducer ring (roughly consistent with the built transducer) and mechanical resistance $R_{\text{m}} = 850\ \text{N}\cdot\text{s/m}$ is added to based on the material properties of the urethane. Model 1 includes this extra mass and resistance by adding them to M and R_{m} in the circuit model shown in Fig. 3.4. Model 3 includes them by adding the impedance

$$z_{\text{ur}} = \frac{R_{\text{m}} + j\omega M_{\text{ur}}}{4N} \tag{6.1}$$

to the impedance Z given in Eq. (5.64). The response of Model 3 is more closely aligned with the experimental data than Model 1 is, though the pri-

mary resonance exhibited in the experimental data is considerably sharper. Additionally, the mechanical resistance added to Model 3 to account for the urethane damps out the bending resonance, though it can still be seen in the experimental data. A resonance due to urethane overmolding effects not accounted for in Model 1 or Model 3 occurs in the experimental results at around $f/f_0 = 1.2$.

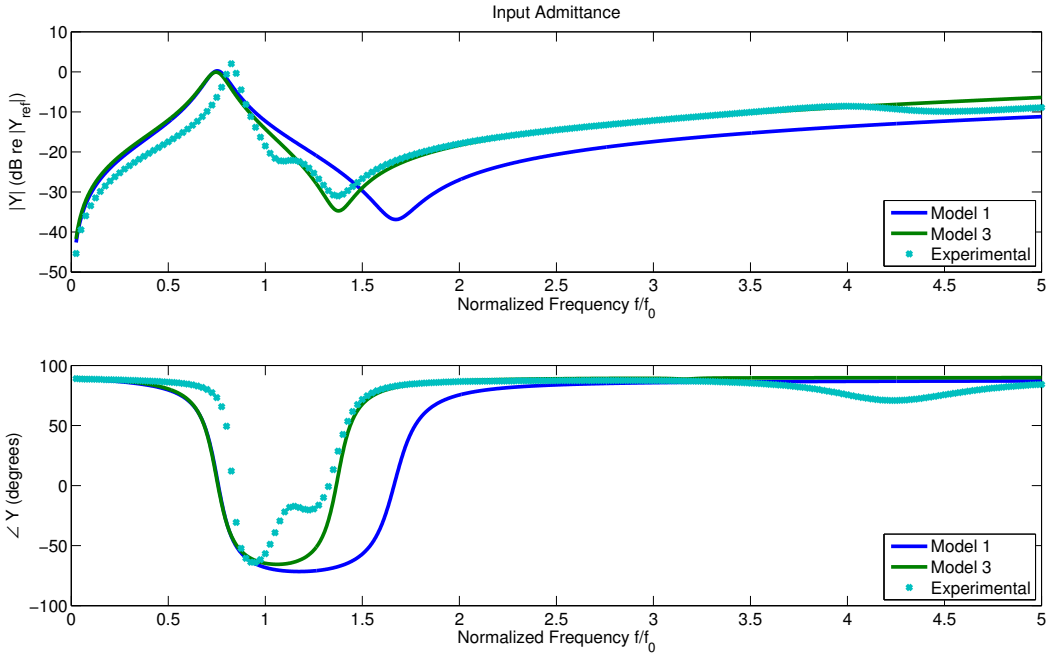

Figure 6.4: Experimentally captured electrical admittance of overmolded transducer in air, compared with lumped element models.

6.3 Average Radial Velocity

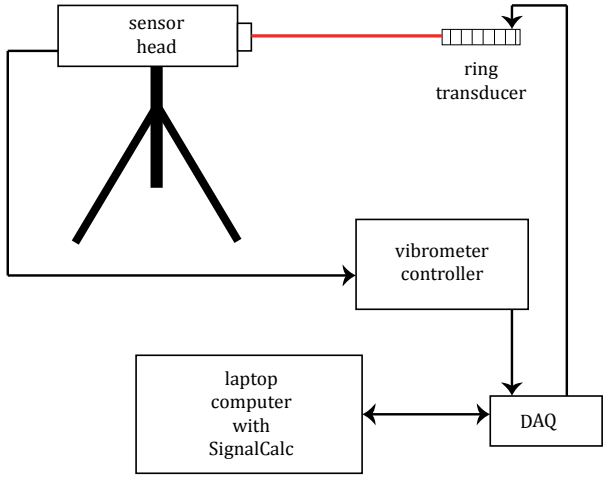

Figure 6.5: LDV test setup.

The average radial velocity of the transducer is found using a laser Doppler vibrometer (LDV). As its name suggests, this device targets an object with a continuous waveform laser signal and tracks the Doppler shift in the returned signal to directly measure the velocity of the target spot. This experiment was conducted with a Polytec OFV-505 sensor head connected to a Polytec OFV-5000 vibrometer controller. Additionally, a DataPhysics Quattro data acquisition system (DAQ) and laptop computer with SignalCalc software were used to obtain and process the resulting data. This test setup is shown schematically in Fig. 6.5. The LDV's laser was focused on the center of a ring element's outer face, and the ring was excited with a voltage signal chirp over

the frequency range of interest, created with SignalCalc and routed through the DAQ. The resulting velocity and input voltage information were captured by the LDV and routed to a laptop computer through the Quattro DAQ. This data was then processed through SignalCalc to produce a voltage-to-velocity transfer function, from which the radial velocity of the element can be determined for an input voltage of a given amplitude (which is here assumed to be 1 Volt). The process was repeated for each active and inactive element in the ring, and these results were combined to produce the average radial velocity. As described in Section 2.4.3, the average radial velocity is closely related to the transmit voltage response of the transducer. The LDV allows for a direct measurement of this quantity on the transducer itself and thus has the potential to provide more insight into the response of the transducer than the TVR which, by definition, is a measurement taken at some distance from the transducer itself and includes effects of radiation impedance and constructive and destructive interference resulting from in-phase and out-of-phase surface motion.

Figure 6.6 depicts the experimental data of the average radial velocity for the bare ring, the ring with filament winding, and the ring with winding and overmold. The primary breathing resonance around $f/f_0 = 1$ is clearly observed in these plots, though it is shifted up in frequency by the winding and shifted down in frequency and dampened by the overmold. Additionally, the effects of the bending resonance are clearly observed at the higher frequencies, around $f/f_0 = 4.5$, though this resonance is significantly damped when the

ring is overmolded.

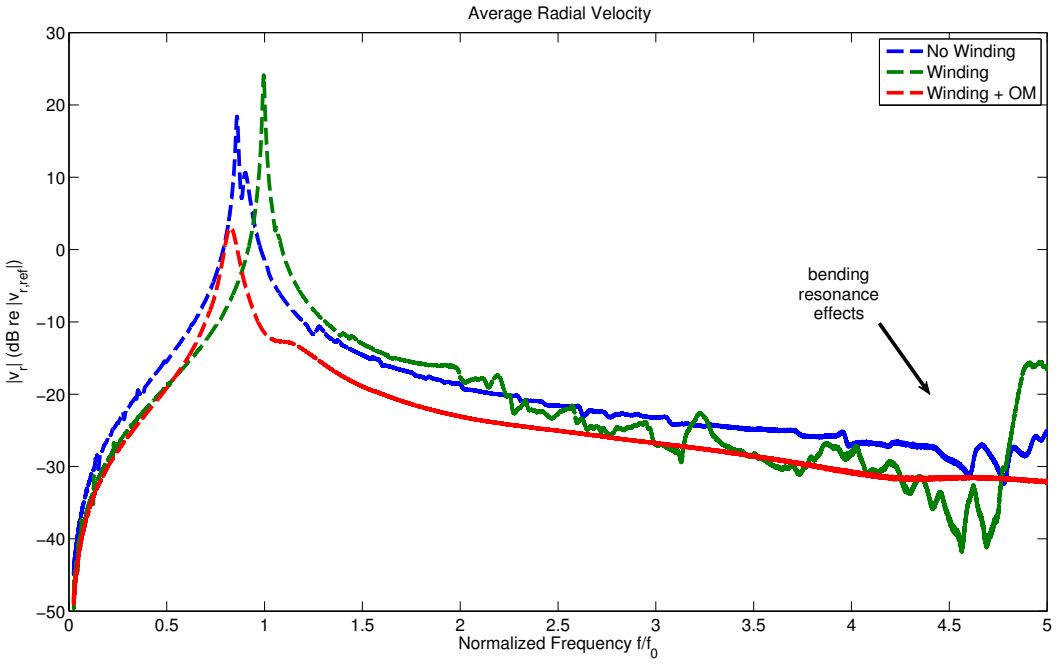

Figure 6.6: Average radial velocity of transducer ring with no winding, ring with winding, and ring with winding and overmold (OM), from LDV data.

Figures 6.7 and 6.8 and compare the average radial velocity of the transducer given by the LDV tests with that given by the lumped and finite element models, for the ring with and without winding respectively. It can be seen that the primary resonance of the transducer as shown in the LDV data is lower than that given by the models. This is probably due to some deviation in the construction of the ring from the assumptions of each model as discussed previously in Section 6.2. In the results of the ring without winding, shown in Fig. 6.7, the bending resonance can be observed in the LDV data, around the same frequency as predicted by the FEM model, though much

smaller in amplitude. Model 3 displays this resonance but at a slightly lower frequency, for reasons discussed in Section 5.3.3.1. This resonance is more prominently displayed in the LDV data for the ring with winding, as can be seen in Fig. 6.8. The frequency at which this bending resonance occurs in the LDV data is in good agreement with the same in Model 3, though the resonance has been pushed out of the operating band in the FEM data. This is primarily due to the geometry of the interstitial elements used in the FEM as discussed in Section 5.4.1. The data indicates that the models provide an acceptable approximation of the average radial velocity of the built transducer and provide good evidence that the bending resonance is physically occurring.

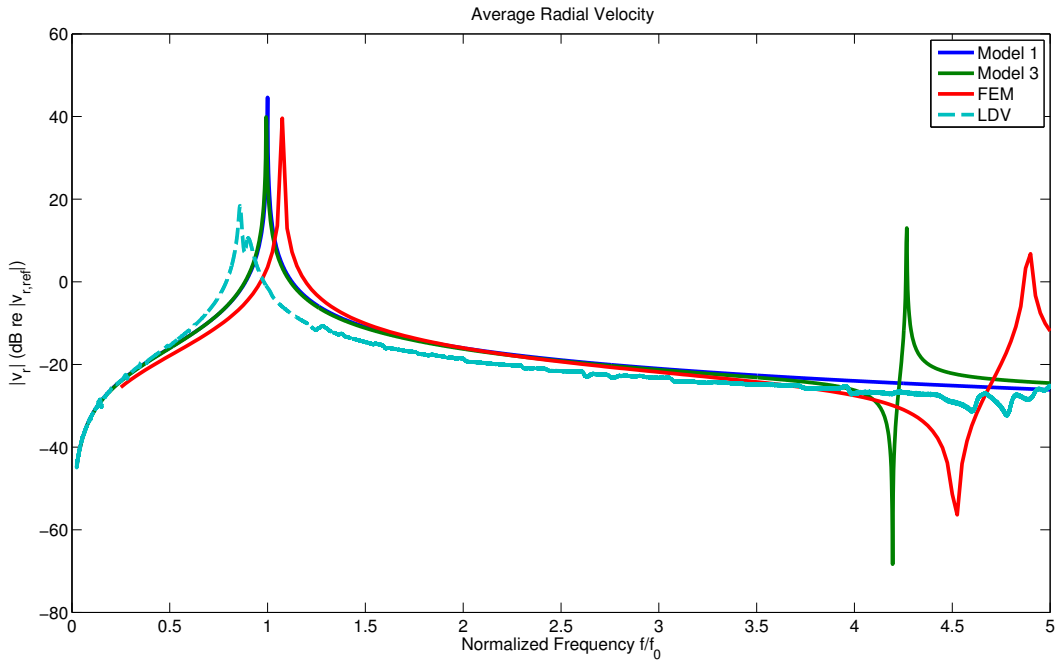

Figure 6.7: Average radial velocity of bare transducer ring, from various models and LDV data.

6.4 Transmit Voltage Response

As described in Section 2.4.3, the transmit voltage response (TVR) of a transducer is the pressure-to-voltage transfer function, or transmit sensitivity, scaled at a distance of 1 meter, when the transducer is deployed underwater. For a pressure p measured at a distance r in the far field of the transducer, the TVR is given by

$$\text{TVR (dB re 1 } \mu\text{Pa/V at 1 m)} = 20\log_{10}\left(\frac{pr/V}{M_{\text{ref}}}\right), \tag{6.2}$$

where V is the applied voltage at the transducer and the reference sensitivity M_{ref} is given by $M_{\text{ref}} = 1\mu\text{Pa}\cdot\text{m/V}$. The TVR can be found experimentally

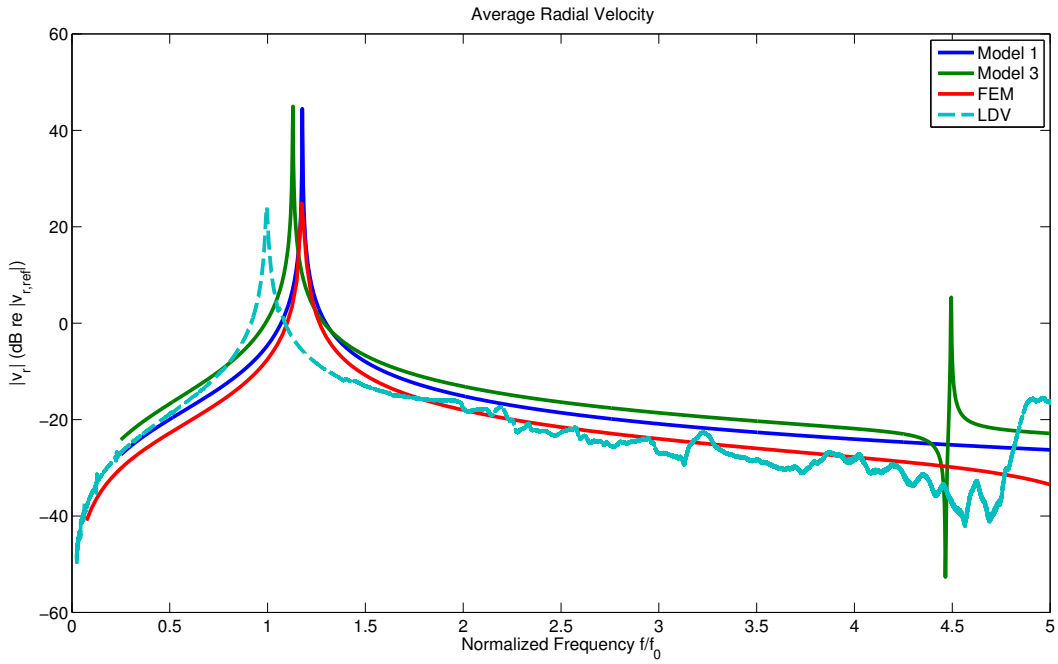

Figure 6.8: Average radial velocity of transducer ring with winding, from various models and LDV data.

by placing the transducer in a tank of water, exciting it at various frequencies, and measuring the signal at a hydrophone with a calibrated receive sensitivity in the far field of the transducer. This set up is shown schematically in Fig. 6.9. It is worth noting that when conducting measurements in a tank, care must be taken to avoid interference with the desired signal from wall, floor, and surface reflections so that free field conditions may be approximated. In this experiment, the transducer and hydrophone were placed to avoid reflections, and their positions in the schematic are not to scale. Additional equipment required includes a signal generator used to produce the excitation signal being sent to the transducer, an oscilloscope used to digitize the received signal

from the hydrophone and save the data, and a computer to store and process the data. Optional equipment used here includes a hydrophone preamplifier circuit and a high-pass filter used to eliminate low-frequency noise from the hydrophone signal. Equipment used in this experiment includes a Tektronix AFG3021B function generator, Tektronix TDS5104B digital oscilloscope, and a Krohn-Hite 3202 filter. The experiment was run by sending shaded tone bursts at frequencies in the band of interest to the transducer from the signal generator. The received signal from the hydrophone was then compared with that sent by the signal generator at each frequency to produce a voltage-to-pressure transfer function. This is scaled back from the transducer-hydrophone distance to a distance of 1 meter, assuming spherical spreading, and given as the TVR.

For the lumped element and finite element models presented in Chapters 4 and 5, the TVR is found by approximating the pressure produced by the transducer at 1 m as that of a simple source, as described in Section 6.4. With this approximation, the TVR can be found directly from the average radial velocity according to Eq. 2.37. This allows the models to be simplified, but does not account for three-dimensional radiation effects that can influence the performance of the built transducer. Additionally, the lumped element and finite element models do not account for the effects of the assembly, though it can be seen from the admittance data in Fig. 6.2 that the internal oil volume couples into the assembly structure in such a way that the performance of the transducer in noticeably affected. To account for these effects, the results of

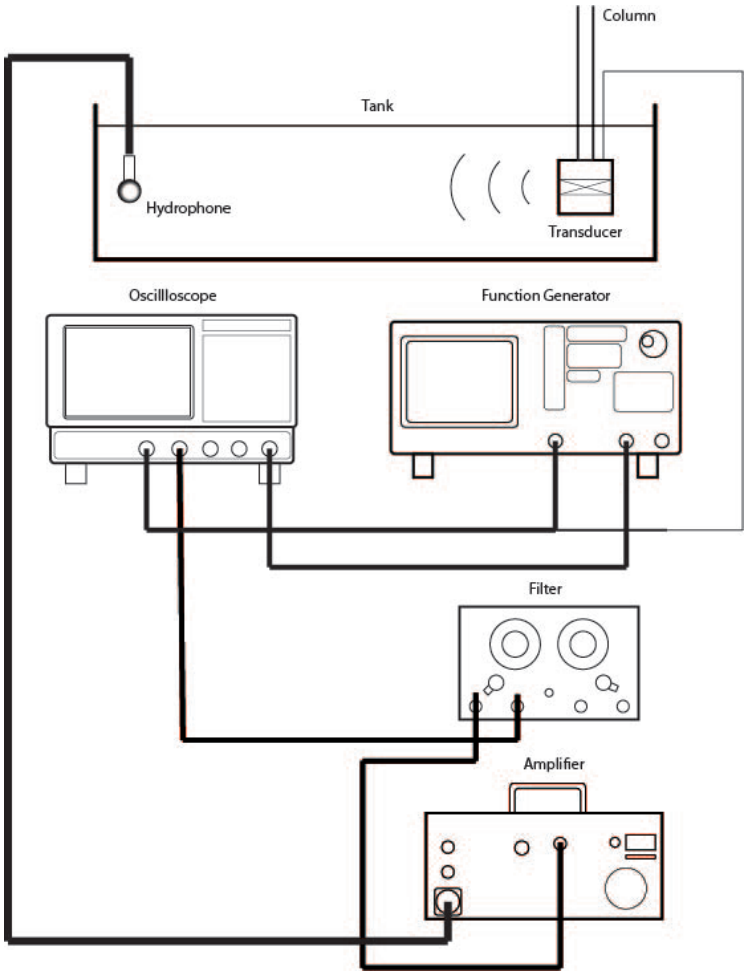

Figure 6.9: Schematic of TVR tank testing set up. Tank not to scale.

a second FEM model ("FEM 2") are presented here in which the assembly and other aspects of the actual transducer structure are included, making it a more realistic basis of comparison for the performance of the built device. Additionally, this second model uses a far-field pressure as determined by the full Kirchhoff-Helmholtz integral equation to determine the TVR rather than using the average radial velocity, thereby accounting for the effect of the as-

sembly geometry on the radiation impedance.

Figure 6.10 compares the experimentally measured TVR (for the transducer in the assembly with oil, with and without urethane overmold) with that of the lumped and finite element models. The results shown as FEM 1 have been modified to represent the response of a transducer ring subject to the radiation impedance of a finite cylinder, as described in Appendix D. The experimental results share key features with Model 1, Model 3, and FEM 1, though appear at a significantly lower level. This is due to the approximations made by those models in calculating the TVR, as described above, in addition to the effects of the urethane and assembly not accounted for. By contrast, FEM 2 provides a more realistic estimation of the performance of the transducer, both in terms of level and in displaying some of the resonances due to the structure of the assembly. For example, there seems to be a null introduced in the experimental results around the frequency at which Model 1, Model 3, and FEM 1 exhibit the primary resonance. The results of FEM 2 exhibit this null as well, albeit at a slightly lower frequency, indicating that this is primarily an effect of the packaging. However, FEM 2 is a considerably more complicated model than Model 1 or Model 3, and requires a significant amount of computation time and power.

Many of the salient features of the transducer's performance exhibited in the experimental data are apparent in Model 3. The anti-resonance at around $f/f_0 = 2.5$, due to standing waves in the internal oil volume, appears clearly in Model 3 and the experimental results. The effect of the bending

resonance, occurring around $f/f_0 = 3.5$, can be seen in the experimental results as a drop in the TVR level. The same bending resonance appears in Model 3, though considerably weaker and at a higher frequency. Additionally, Model 3 is in fairly good agreement with FEM 1, aside from the strength and location of the bending resonance, indicating that the much of the basic physics of the transducer itself are captured by it. The standing wave anti-resonance at $f/f_0 = 4.8$ shown in the models does not appear in the experimental results, and may have pushed beyond the operating band by the assembly.

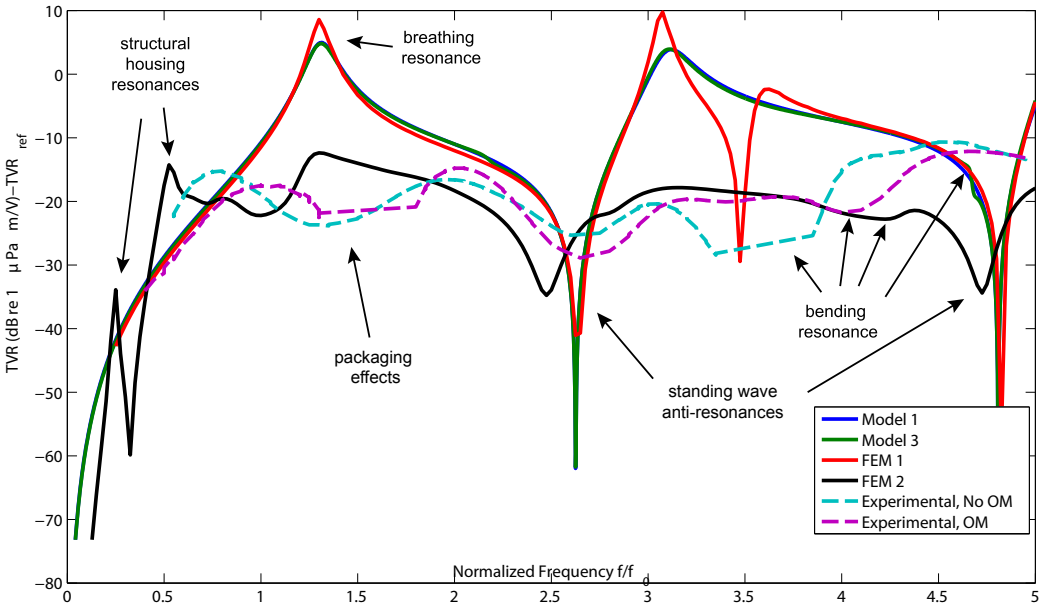

Figure 6.10: Experimentally captured TVR, with and without urethane overmold (OM) as indicated. Results are compared with lumped element models.

6.5 Total Harmonic Distortion

The total harmonic distortion(THD), defined in Section 2.4.4, can be investigated by exciting the transducer with a relatively pure tone sine wave and analyzing the frequency content of the output to determine the relative amplitudes of the harmonics generated. This is done for a range of frequencies to determine the THD as a function of frequency for a given drive level. In this experiment, the THD was found for the segmented ring transducer at various driving voltage levels. An example of the experimental data shown in Fig. 6.11. A signal with normalized frequency $f/f_0 = 3.5$ was used to excite the transducer underwater at amplitudes ranging from 25 to 200 V, and the resulting acoustic signal was measured by a hydrophone. Harmonics of the fundamental frequency can be seen as peaks in the frequency domain plot of the received voltage signal, which have been circled for emphasis. It can be seen that the 200 V input has the highest harmonic peaks and thus the most distortion.

The same analysis is done for every frequency at each voltage and the total harmonic distortion, as described in Section 2.4.4, is calculated according to Eq. 2.38. The resulting plot of the THD generated by the segmented ring transducer as a function of frequency for various voltages is shown in Fig. 6.12. The early peaks, occurring for $f/f_0 < 1$, result from signal processing artifacts, or leakage, as a finite pulse was used as required by a smaller than desired measurement volume. Disregarding these early peaks, most of the harmonic distortion occurs at the higher frequencies, around the bending resonance,

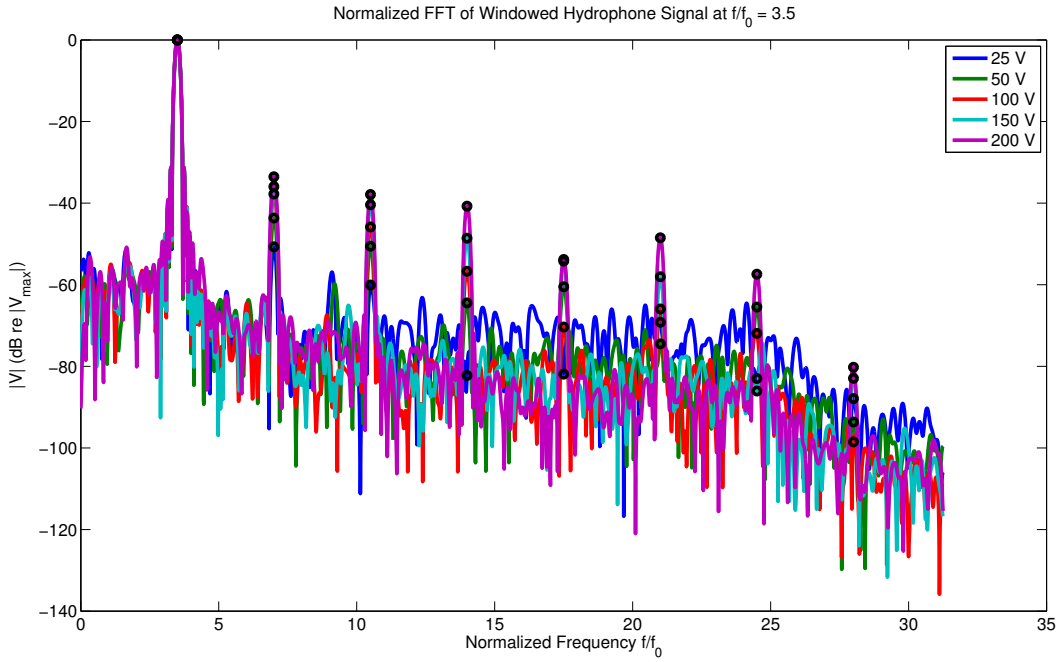

Figure 6.11: Normalized frequency domain of hydrophone signal at $f/f_0 = 3.5$. Voltage amplitude $|V|$ is normalized by the maximum value $|V_{\max}|$.

and increases with increasing voltage levels. Since the transducer needs to operate with minimal distortion at a range of drive levels, the influence of the bending resonance on distortion generation is a further indication that it should be eliminated from the transducer behavior. The mechanism for this nonlinearity is described in Appendix B and a description of how it may be included in Model 3 is given in Section 5.5.

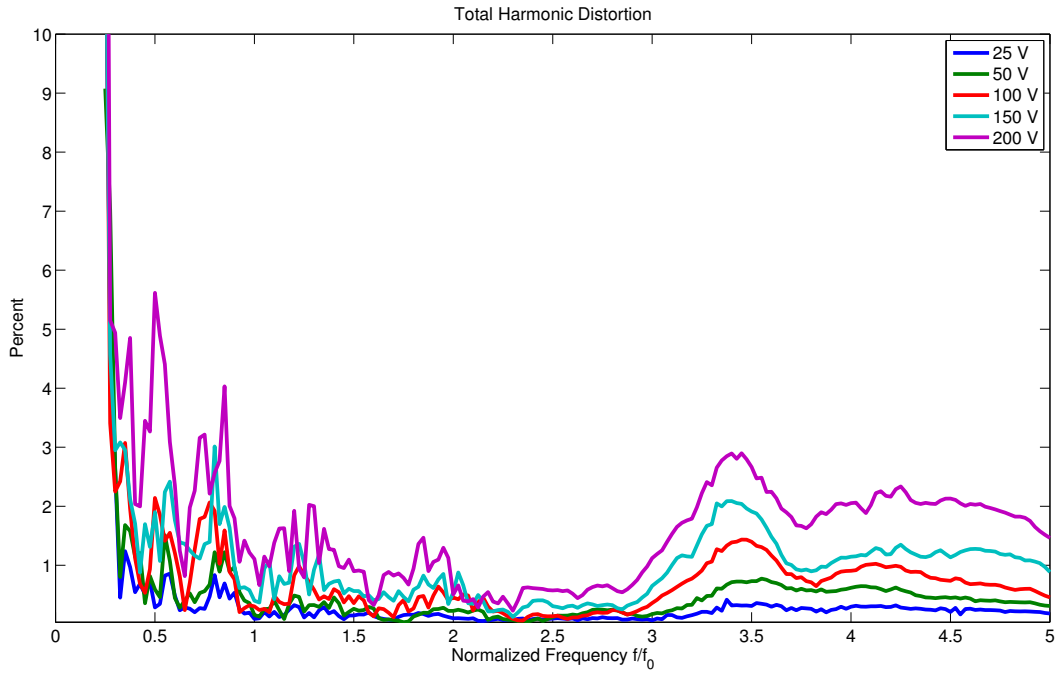

Figure 6.12: Total harmonic distortion of transducer driven at various voltages.

Chapter 7

Conclusions and Future Work

A multi-degree-of-freedom (MDOF) lumped parameter model for a segmented ring transducer has been presented that captures important characteristics of the transducer's performance. Specifically, as compared with the lumped parameter models with a single degree of freedom that have been previously used to model ring transducers, this new model captures a secondary bending mode and offers a better estimate of the electromechanical efficiency of the transducer. As this bending mode is often parasitic, the MDOF model can be used as a design tool to prevent the mode from appearing in the operating band of interest. Additionally, the MDOF model offers ways in which common modifications to the basic segmented ring—such as filament winding, internal oil volume, and radiation impedance—can be accounted for. Experimental results indicate that the model provides a better description of the performance of the transducer than the one-degree-of-freedom lumped parameter model. Compared with similar finite element models, the MDOF model provides a good description of the transducer without requiring significant computational time or power.

There are, however, some limitations to the MDOF model, some of

which may be investigated for future work. The MDOF captures the bending resonance, but at a lower frequency than seen in the experimental and finite element data. This is thought to be due to geometrical approximations made in the MDOF model, though that remains to be confirmed. If it is a geometrical effect, allowing for it in the MDOF model would increase its accuracy and effectiveness as a design tool. Likewise, approximations are made in the MDOF model regarding radiation impedance due to water loading and the effects of the internal oil volume. Both of these effects are incorporated into the model with the assumption that the ring is undergoing purely radial motion. Once bending is allowed for, the perimeter of the ring is no longer circular, and the boundary conditions deviate from what is assumed in the radiation and internal oil volume impedance models. An impedance model for either might be developed that accounts for the this change. Additionally, a method for incorporating geometrical nonlinearities in the MDOF model was described in this thesis but a simulation of nonlinear distortion was not performed. Finally, the experimental data indicates that effects not accounted for in the MDOF model can have a significant effect on the performance of the transducer. In particular, the MDOF model does not account for the effects related to the transducer coupling into the transducer assembly, or the acoustic radiation effects from the actual three-dimensional geometry of the transducer. These effects are outside the scope of a simple lumped parameter model, though the MDOF model could be improved by a better understanding of them.

Appendices

Appendix A

Materials and Dimensions

The material properties and dimensions used in this project for the 31-mode segmented ring transducer are given in the tables below. Because concerns of the project sponsor prevent a full disclosure of all relevant dimensions, the dimensions here have been given in terms of ratios to the piezoelectric element length L_1, which is itself withheld. Likewise, all plots are normalized as follows. Values are plotted in the frequency domain as a function of the ratio f/f_0, where f is the frequency and f_0 is the frequency of maximum admittance given by Model 1 for the in-air case. The amplitudes of impedance, admittance, radial velocity, and TVR plots are normalized by reference values Z_{ref}, Y_{ref}, $v_{\text{r,ref}}$, and TVR_{ref}, which represent the maximum values of the respective quantities given by Model 1 for the in-water case.

Table A.1: Active Element Properties and Dimensions
Single Crystal PIN24%-PMN-PT (HC Materials)

Density [kg/m^3]	$\rho_1 = 8122$
Short-Circuit Compliance [10^{-12} 1/Pa]	$\mathrm{s}_{11}^E = 59.11$
Young's Modulus [Pa]	$\mathrm{E}_1 = 1/s_{11}^E$
Piezoelectric Coupling Coefficient [10^{-12} C/N]	$d_{31} = -1196$
Stress-Free Dielectric Constant [10^{-8} F/m]	$\epsilon_{33}^T = 31.99$
Clamped Dielectric Constant [10^{-10} F/m]	$\epsilon_{33}^S = 58.97$
Height-Length Ratio	$\mathrm{h}/\mathrm{L}_1 = 0.9556$
Thickness-Length Ratio	$\mathrm{t}/\mathrm{L}_1 = 0.1411$
Cross-Sectional Area	$A_1 = h \cdot t$
Generalized Poisson's Ratios	$\nu_{12} = 0.4123$, $\nu_{21} = 1.5572$
Number of Elements	$N_1 = 16$

Table A.2: Inactive Element Properties and Dimensions
96% Alumina (CoorsTek)

Density [kg/m^3]	$\rho_2 = 3890$
Young's Modulus [10^9 Pa]	$E_2 = 300$
Length-Length Ratio	$\mathrm{L}_1/L_1 = 1$
Cross-Sectional Area	$A_2 = h \cdot t$
Number of Elements	$N_2 = 16$

Table A.3: Ring Dimensions

Radius [m]	$\rho_2 = 3890$
Height-Length Ratio	$h/L_1 = 0.9556$
Thickness-Length Ratio Ratio	$t/L_1 = 1$
Cross-Sectional Area	$A = A_1 = A_2 = h \cdot t$
Total Number of Elements	$N = N_1 + N_2 = 32$
Unit Cell Angle	$\theta = 2\pi/N$

Table A.4: Filament Properties and Dimensions

Density [kg/m^3]	$\rho_{\mathrm{w}} = 640$
Compliance [10^{-12} 1/Pa]	$s_{11}^{\mathrm{w}} = 23.81$
Young's Modulus [10^9 Pa]	$E_{\mathrm{w}} = 42$
Height	$h_{\mathrm{w}} = 0.85 \cdot h$
Thickness [m]	$t_{\mathrm{w}} = 0.001$

Table A.5: Internal Oil Volume Properties

Density [kg/m^3]	$\rho_{\mathrm{vol}} = 640$
Sound Speed [m/s]	$c_{\mathrm{vol}} = 1540$

Table A.6: Water Properties

Density [kg/m^3]	$\rho_0 = 1000$
Sound Speed [m/s]	$c_0 = 1500$

Appendix B

Beam Modeling

The elements used in the construction of the ring are subject to transverse motion and can be modeled in this regard as bending beams. This appendix reviews beam models that are implemented in the construction of Model 3 in Section 5.3.3.

B.1 Basic Beam Model

A uniform beam with cross-section area A, density ρ, Young's modulus E, area of inertia I, and length L is shown in Fig. B.1, where $w(x,t)$ is the transverse displacement of the beam at position x and time t. A finite element slice of this beam is shown in Fig. B.2, where V is the shear force, M is the moment, angle θ is the rotation of the neutral axis of the beam with respect to a horizontal reference, and angle ϕ is the rotation of a plane cross-section with respect to a vertical reference. A Bernoulli-Euler beam approximation is one in which plane cross-sections remain perpendicular to the neutral axis (shown as a dotted line in Fig. B.2) of the beam during bending, i.e. the shear modulus of the slice is effectively infinite. For such a beam, $\theta = \phi$. A Bernoulli-Euler model is sufficient for the purposes of the model presented

in the body of this thesis, though a Timoshenko beam model is presented in Section B.2.3 for completeness.

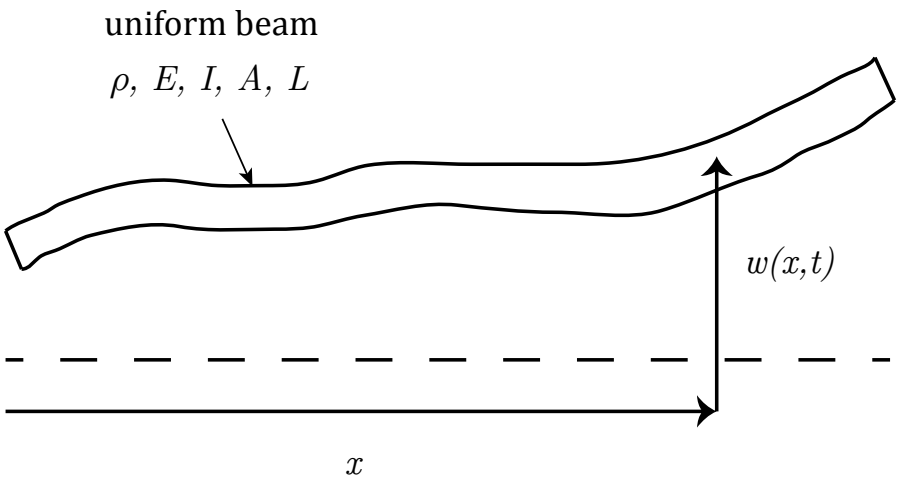

Figure B.1: Uniform Beam, adapted from Karnopp and Margolis [18].

Using Newton's 2nd law, the vertical equation of motion for the beam slice shown in Fig. B.2 is given by

$$V(x+\Delta x) - V(x) = \rho A \Delta x \frac{\partial^2 w}{\partial^2 t}. \tag{B.1}$$

Rotary inertia is neglected in the Bernoulli-Euler beam model, thus the sum of the torques about the slice is zero:

$$M(x+\Delta x) - M(x) + V(x+\Delta x)\Delta x = 0. \tag{B.2}$$

The relationship between bending moment and bending deformation is given by

$$M(x) = \frac{EI}{\Delta x}\left(\theta(x+\Delta x) - \theta(x)\right), \tag{B.3}$$

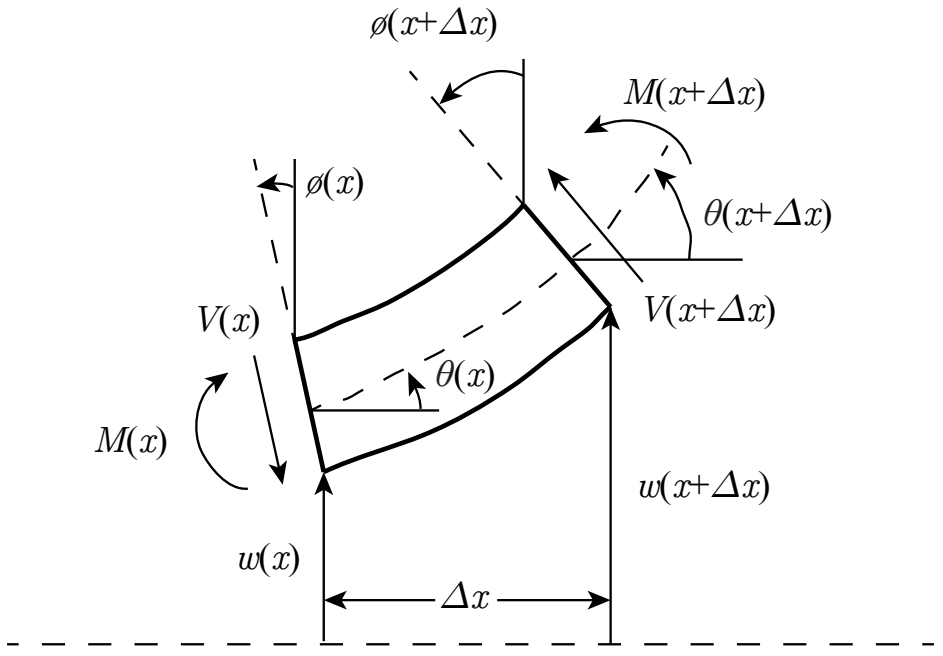

Figure B.2: Uniform Beam, from Karnopp and Margolis [18].

and it can be seen from Fig. B.2 that

$$\theta(x) = \frac{w(x + \Delta x) - w(x)}{\Delta x}. \tag{B.4}$$

Karnopp and Margolis [18] present a bond graph for the lumped parameter model for a Bernoulli-Euler beam that is consistent with the above equations and is reproduced in Fig. B.3. The beam may be divided into however many lumps is necessary, and Δx will simply be the beam length L divided by the number of lumps. From the figure it can be seen that the lumped mass

is given by

$$m = \rho A \Delta x, \tag{B.5}$$

and the lumped bending stiffness is given by

$$k_{\mathrm{b}} = \frac{EI}{\Delta x}, \tag{B.6}$$

or alternatively, as a lumped bending compliance

$$c_{\mathrm{b}} = \frac{\Delta x}{EI}. \tag{B.7}$$

The corresponding equivalent circuit is shown in Fig. B.4.

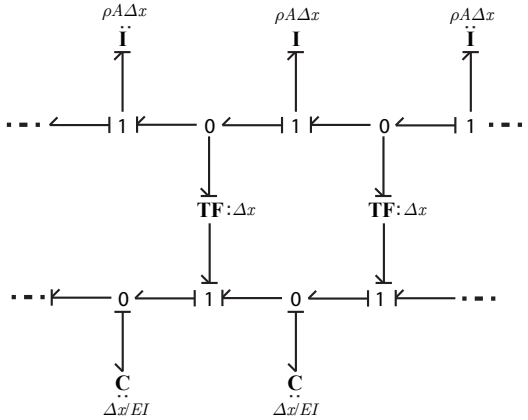

Figure B.3: Bond Graph for Uniform Beam, from Karnopp and Margolis [18].

Eqs. (B.3) through (B.4) may be written in differential form by letting

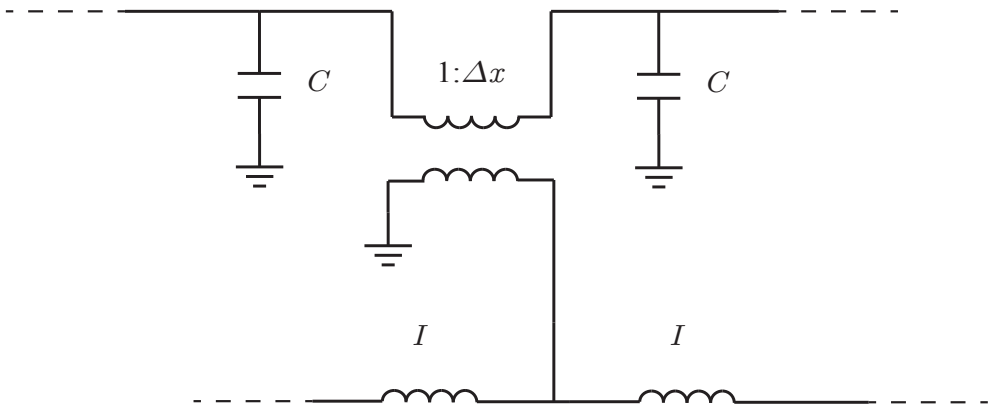

Figure B.4: Circuit Model for Uniform Beam, from Karnopp and Margolis [18].

$\Delta x \to 0$. After rearranging they become:

$$\frac{\partial V}{\partial x} = \rho A \frac{\partial^2 w}{\partial^2 t} \tag{B.8}$$

$$V = -\frac{\partial M}{\partial x} \tag{B.9}$$

$$M = EI \frac{\partial \theta}{\partial x} \tag{B.10}$$

$$\theta = \frac{\partial w}{\partial x}. \tag{B.11}$$

Combining equations B.8 - B.11 yields the equation governing the (free) motion of the beam:

$$EI \frac{\partial^4 w}{\partial^4 x} + \rho A \frac{\partial^2 w}{\partial^2 t} = 0. \tag{B.12}$$

B.2 Modifications

As the dimensions of a beam deviate from the long and slender ideal, or if it is driven to significantly large transverse displacement amplitudes, its behavior will deviate from the theory presented in Section B.1. The bond graph shown in Fig. B.3 can be modified to account for some of these effects, as presented in Sections B.2.1 through B.2.3.

B.2.1 Plate Model

The analysis presented above is appropriate for beams, that is, structural elements whose length is much larger than transverse or width dimension. In this case the stress is assumed to be uniaxial, acting only along the length of the beam. However, if the width dimension is sufficiently large such that a free condition along that dimension is no longer appropriate, a plane stress is imposed and the beam is more accurately modeled as a plate.

Classical theory gives the (lateral) bending stiffness of a isotropic beam as

$$D = EI, \tag{B.13}$$

while that of a plate is given by

$$D = \frac{EI}{1-\nu^2}. \tag{B.14}$$

where ν is Poisson's ratio. The factor $\frac{1}{1-\nu^2}$ appears in the plate stiffness as a result of the plane strain assumption.

If the plate is orthotropic, that is, if its properties differ along the length (x) and width (y) direction, the bending stiffness along the length of the beam is given by

$$D = \frac{E_x I}{1 - \nu_{xy}\nu_{yx}}. \tag{B.15}$$

where E is the Young's modulus along the direction indicated by the subscript and ν_{xy} and ν_{yx} are generalized Poisson's ratios related by $\nu_{xy}E_y = \nu_{yx}E_x$.

In terms of entries of the 6 x 6 compliance matrix $\mathbf{s}$ of an orthotropic material, such as that discussed for a piezoleectric material in Chapter 2,

$$E_x = 1/s_{11} \tag{B.16}$$

$$E_y = 1/s_{22} \tag{B.17}$$

$$\nu_{xy} = -s_{12}E_x \tag{B.18}$$

$$\nu_{yx} = -s_{12}E_y. \tag{B.19}$$

The bond graph shown in Fig. B.3 may be used to model an isotropic or orthotropic plate by replacing the EI factor in the bending stiffness (Eq. B.7) with Eq. B.14 or B.15 respectively.

B.2.2 Nonlinear Beam

A bending beam may demonstrate nonlinear effects if the deformations are significantly large. The equation for the bending moment given by Eq. B.3 represents an approximation for small angles. For larger deformations, it is more accurately represented by

$$M(x) = \frac{EI}{\Delta x} \tan\left(\theta(x + \Delta x) - \theta(x)\right). \tag{B.20}$$

The function $\tan x$ may be series expanded as

$$\tan x \approx x + \frac{1}{3}x^3 + O(x^5). \tag{B.21}$$

Using this tangent expansion with terms of order x^3 in Eq. B.20 produces

$$M(x) = \frac{EI}{\Delta x}\left(\theta(x+\Delta x) - \theta(x)\right)\left[1 + \frac{1}{3}\left(\theta(x+\Delta x) - \theta(x)\right)^2\right] \tag{B.22}$$

The bending stiffness given in Eq. B.6 can be modified in light of Eq. B.22 to represent a nonlinear stiffness as

$$k_{b,\mathrm{nl}} = \frac{EI}{\Delta x}\left[1 + \frac{1}{3}\left(\theta(x+\Delta x) - \theta(x)\right)^2\right], \tag{B.23}$$

or as a nonlinear compliance

$$c_{b,\mathrm{nl}} = \frac{\Delta x}{EI}\frac{1}{\left[1 + \frac{1}{3}\left(\theta(x+\Delta x) - \theta(x)\right)^2\right]} = \frac{c_{\mathrm{b}}}{\left[1 + \frac{1}{3}\left(\theta(x+\Delta x) - \theta(x)\right)^2\right]}, \tag{B.24}$$

and used in the bond graph presented in Figs. B.3 or B.5.

B.2.3 Timoshenko Beam

The Timoshenko model of a beam can be used to describe beams that are relatively short and sturdy, that is, beams with relatively large cross-sectional dimensions. In the Timoshenko model, plane cross-sections no longer remain perpendicular to the neutral axis during bending and a finite shear stiffness as well as rotary inertia must be accounted for. These additional mechanisms effectively lower the stiffness of the beam and thus lower its resonant frequencies. Karnopp and Margolis [18] present a lumped parameter

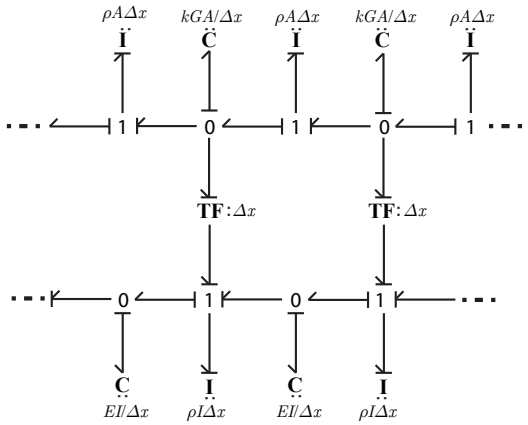

Figure B.5: Uniform Beam, from Karnopp and Margolis [18].

model for a Timoshenko beam that is reproduced in Fig. B.5. Notice the similarity with the Bernoulli-Euler beam in Fig. B.3, though in this case additional **C** and **I** elements are added to account for the shear stiffness and rotary inertia respectively. This Timoshenko beam model may be used in place of the Bernoulli-Euler model used in the bond graph for Model 3 presented in Section 5.3.3 if the dimensions of the elements are such that significant Timoshenko effects are occurring.

Appendix C

MATLAB Code for Finite Element Method Modeling

The following is the MATLAB code used in this thesis for the custom-made finite element model described in Section 4.1. Becuase concerns of the project sponsor prevent a full disclosure of all relevant dimensions, the dimensions here have been given in terms of ratios to the piezoelectric element length L_1, which is itself withheld (and shown in the code as "XXX").

```
%% Material Properties and Dimensions
p = 20; % number of finite elements
N = 32; % total number of elements (active and inactive)
theta = 2*pi/N; % central angle for unit cell
% active element properties (active = 1)
rho1 = 8122; % density of active element [kg/m^3]
L1 = XXX; % length [m]
l1 = .5*L1; % length of half element [m]
W1 = 0.9956*L1; % width [m]
T1 =  0.1411*L1;% thickness [m]
A1 = W1*T1; % cross-sectional area of active element [m^2]
s11E1 = 59.11e-12; % short-circuit mech compliance of active ...
    element [1/Pa]
s12 = -24.37*1e-12; % compliance of active element for strain ...
    in 1 direction from stress in 2 direction
s22 = 15.65*1e-12; % compliance of active element for strain ...
    in 2 direction from stress in 2 direction
nu21 = -s12/s22; % Poisson's ratio for strain in 1 direction ...
    from stress in 2 direction
```

```
nu12 = -s12/s11E1; % Poisson's ratio for strain in 2 direction ...
    from stress in 1 direction
E1 = 1/s11E1; % Young's modulus for active element [Pa]
E1b = 1/s11E1*(1/(1-nu21*nu12)); % Young's modulus for active ...
    element (for bending) [Pa]
I1 = (W1*T1^3)/12; % cross-sectional moment of inertia [m^4]
V1 = 0.5*L1*W1*T1; % volume of half of an element [m^3]
m1 = rho1*V1/l1; % mass per unit length of active element [kg/m]
% inactive element properties (inactive = 2)
A2 = A1; l2 = l1; W2 = W1; L2 = L1; T2 = T1;
rho2 = 3890; % density of inactive element [kg/m^3]
s11E2 = 1/300e9; % mechanical compliance of inactive element ...
    [1/Pa]
nu2 = .21; % Poisson's ratio of alumina
E2 = 1/s11E2; % Young's modulus for inactive element [Pa]
E2b = 1/s11E2*(1/(1-nu2^2)); % Young's modulus for inactive ...
    element (for bending) [Pa]
I2 = (W2*T2^3)/12; % cross-sectional moment of inertia [m^4]
V2 = 0.5*L2*W2*T2; % volume of half of an element [m^3]
m2 = rho2*V2/l2; % mass per unit length of active element [kg/m]

% Create Matrices for Parameters
l = zeros(1,p); m = zeros(1,p); E = zeros(1,p); Eb = ...
    zeros(1,p); I = zeros(1,p); A = zeros(1,p);
for i = 1:p/2;
    l(i) = l1/(p/2);
    l(i+p/2) = l2/(p/2);
    m(i) = m1;
    m(i+p/2) = m2;
    E(i) = E1;
    Eb(i) = E1b;
    E(i+p/2) = E2;
    Eb(i+p/2) = E2b;
    I(i) = I1;
    I(i+p/2) = I2;
    A(i) = A1;
    A(i+p/2) = A2;
end
r = sqrt(I./A); %radius of gyration

%% Mass and Stiffness Matrics
DOF = 3*p+3; % Degrees of Freedom for FREE problem
Mbar = zeros(DOF,DOF); Kbar = zeros(DOF,DOF);
for s = 1:p; % element number
```

```
% element-level mass coefficients
ms = zeros(6,6); ks = zeros(6,6);
ms(1,1) = 140;
ms(1,4) = 70; ms(4,1) = 70;
ms(2,2) = 156;
ms(2,3) = 22*l(s); ms(3,2) = 22*l(s);
ms(2,5) = 54; ms(5,2) = 54;
ms(2,6) = -13*l(s); ms(6,2) = -13*l(s);
ms(3,6) = -3*l(s)^2; ms(6,3) = -3*l(s)^2;
ms(3,3) = 4*l(s)^2;
ms(3,5) = 13*l(s); ms(5,3) = 13*l(s);
ms(4,4) = 140;
ms(5,5) = 156;
ms(5,6) = -22*l(s); ms(6,5) = -22*l(s);
ms(6,6) = 4*l(s)^2;
ms = m(s)*l(s)/(420)*ms;

% element-level stiffness coefficients
ks(1,1) = (l(s)/r(s))^2; ks(4,4) = (l(s)/r(s))^2;
ks(1,4) = -(l(s)/r(s))^2; ks(4,1) = -(l(s)/r(s))^2;
ks(2,2) = 12;
ks(2,3) = 6*l(s); ks(3,2) = 6*l(s);
ks(2,5) = -12; ks(5,2) = -12;
ks(2,6) = 6*l(s); ks(6,2) = 6*l(s);
ks(3,3) = 4*l(s)^2;
ks(3,5) = -6*l(s); ks(5,3) = -6*l(s);
ks(3,6) = 2*l(s)^2; ks(6,3) = 2*l(s)^2;
ks(5,5) = 12;
ks(5,6) = -6*l(s); ks(6,5) = -6*l(s);
ks(6,6) = 4*l(s)^2;
% axial (use 'E')
ks(1,1) = (E(s)*I(s)/l(s)^3)*ks(1,1);
ks(1,4) = (E(s)*I(s)/l(s)^3)*ks(1,4);
ks(4,1) = (E(s)*I(s)/l(s)^3)*ks(4,1);
ks(4,4) = (E(s)*I(s)/l(s)^3)*ks(4,4);
% bending (Use 'Eb')
ks(2,2) = (Eb(s)*I(s)/l(s)^3)*ks(2,2);
ks(2,3) = (Eb(s)*I(s)/l(s)^3)*ks(2,3);
ks(3,2) = (Eb(s)*I(s)/l(s)^3)*ks(3,2);
ks(2,5) = (Eb(s)*I(s)/l(s)^3)*ks(2,5);
ks(5,2) = (Eb(s)*I(s)/l(s)^3)*ks(5,2);
ks(2,6) = (Eb(s)*I(s)/l(s)^3)*ks(2,6);
ks(6,2) = (Eb(s)*I(s)/l(s)^3)*ks(6,2);
ks(3,3) = (Eb(s)*I(s)/l(s)^3)*ks(3,3);
ks(3,5) = (Eb(s)*I(s)/l(s)^3)*ks(3,5);
```

```
    ks(5,3) = (Eb(s)*I(s)/l(s)^3)*ks(5,3);
    ks(3,6) = (Eb(s)*I(s)/l(s)^3)*ks(3,6);
    ks(6,3) = (Eb(s)*I(s)/l(s)^3)*ks(6,3);
    ks(5,5) = (Eb(s)*I(s)/l(s)^3)*ks(5,5);
    ks(5,6) = (Eb(s)*I(s)/l(s)^3)*ks(5,6);
    ks(6,5) = (Eb(s)*I(s)/l(s)^3)*ks(6,5);
    ks(6,6) = (Eb(s)*I(s)/l(s)^3)*ks(6,6);

    %Local to Global Coordinate Transform
    L = eye(6);
    if s > p/2
        L(1,1) = cos(theta);
        L(1,2) = sin(theta);
        L(2,1) = -sin(theta);
        L(2,2) = cos(theta);
        L(4,4) = cos(theta);
        L(4,5) = sin(theta);
        L(5,4) = -sin(theta);
        L(5,5) = cos(theta);
    end
    mbars = L'*ms*L;
    kbars = L'*ks*L;
    % connectivity matrix for element 's'
    As = zeros(6,DOF);
    As(:,3*s-2:3*s+3) = eye(6);
    % mass matrix in terms of generalized coordinates for ...
       complete system
    Mbars = As'*mbars*As;
    % stiffness matrix in terms of generalized coordinates for ...
       complete system
    Kbars = As'*kbars*As;
    % sum matrices for complete structure
    Mbar = Mbar + Mbars;
    Kbar = Kbar + Kbars;
end

%% Solve Eigenvalue Problem for Free Case
[V_free D_free] = eig(Kbar,Mbar);
fn_free = sort(sqrt(diag(D_free))/(2*pi)); % natural ...
   frequencies for free case

%% Apply Roller-Roller Boundary Condition
% Ubar1 = 0; Ubar3 = 0;
Mbar(3,:) = []; % remove row 3
Mbar(:,3) = []; % remove column 3
```

```
Mbar(1,:) = []; % remove row 1
Mbar(:,1) = []; % remove column 1
Kbar(3,:) = []; % remove row 3
Kbar(:,3) = []; % remove column 3
Kbar(1,:) = []; % remove row 1
Kbar(:,1) = []; % remove column 1
L(3,:) = []; % remove row 3
L(:,3) = []; % remove column 3
L(1,:) = []; % remove row 1
L(:,1) = []; % remove column 1
% rotate coordinate system by theta
% Rotate M and K
Mstar = L'*Mbar*L;
Kstar = L'*Kbar*L;
% apply boundary condition to far end
% Ubar_end = 0; Ubar_end-2 = 0;
Mstar(end-2,:) = []; % remove row end-2
Mstar(:,end-2) = []; % remove column end-2
Mstar(end,:) = []; % remove row end
Mstar(:,end) = []; % remove column end
Kstar(end-2,:) = []; % remove row end-2
Kstar(:,end-2) = []; % remove column end-2
Kstar(end,:) = []; % remove row end
Kstar(:,end) = []; % remove column end
L(end-2,:) = []; % remove row end-2
L(:,end-2) = []; % remove column end-2
L(end,:) = [];  % remove row end
L(:,end) = []; % remove column end
M = L'*Mstar*L;
K = L'*Kstar*L;

%% Solve Eigenvalue Problem for Roller-Roller Case
[Vrr Drr] = eig(K,M);
fn_rr = sort(sqrt(diag(Drr))/(2*pi)); % natural frequencies ...
   for roller-roller case
```

Appendix D

Infinite Cylinder Correction

This appendix refers to an electromechanical piezoelectric transducer with cylindrical ring geometry, of height h, radius a, and ring thickness t, as shown in Fig. D.1, subject to loading resulting from acoustic radiation into water. When finite element modeling software such as COMSOL Multiphysics is used to model a transducer of this type, symmetry is often invoked in order to reduce the ring and water system to the smallest unit cell possible, so that the domains can be meshed fine enough for accurate results without being computationally prohibitive. A reduced model for the transducer ring in water is described in greater detail in Section 4.2.1 shown here in Fig. D.2. The acoustically hard boundary condition on the top and bottom walls of the wedge (perpendicular to x_2) in the water domain have the effect of imposing the equivalent radiation impedance of a cylindrical ring of infinite height. This radiation impedance is much greater in magnitude than that of a cylinder of finite height and can cause the performance of the transducer as given by the finite element simulation to be significantly different from that exhibited by the actual finite cylinder transducer. This section describes a process for converting the results of a simulation for a ring transducer as a cylinder of infinite height into that of a simulation for a ring transducer as a cylinder

of finite height. In this way a more accurate simulation of the transducer may be obtained without sacrificing the benefits of a reduced model. Due to concerns of the project sponsor, all results have been normalized according to the scheme described in Appendix A.

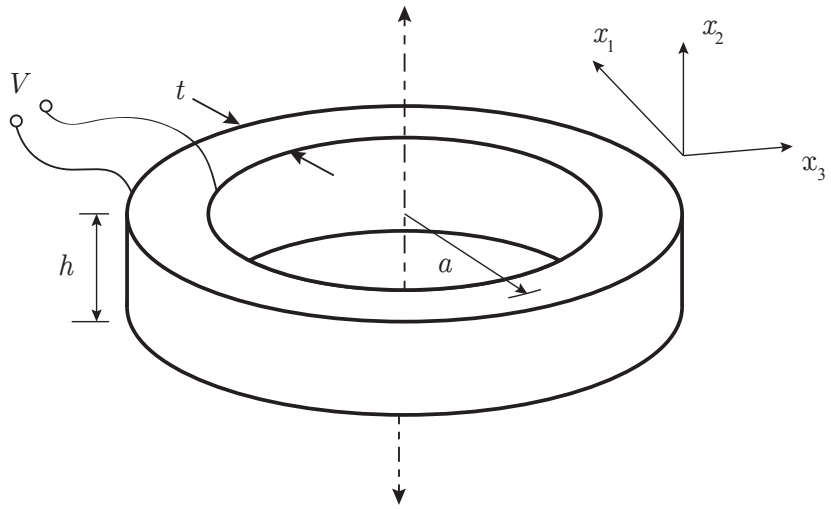

Figure D.1: Cylindrical piezoelectric ring with height h, thickness t, and mean radius a.

The lumped parameter equivalent circuit for the ring subject to radiation loading is shown in Fig. D.3. G_0 and C_0 are the electrical loss conductance and capacitance of the ring, ϕ is the electromechanical turns ratio, and C^E, M, and R_{m} are the mechanical compliance, mass, and resistance of the ring respectively. Z_{vol} is the impedance due to the internal oil volume and Z_{rad} is

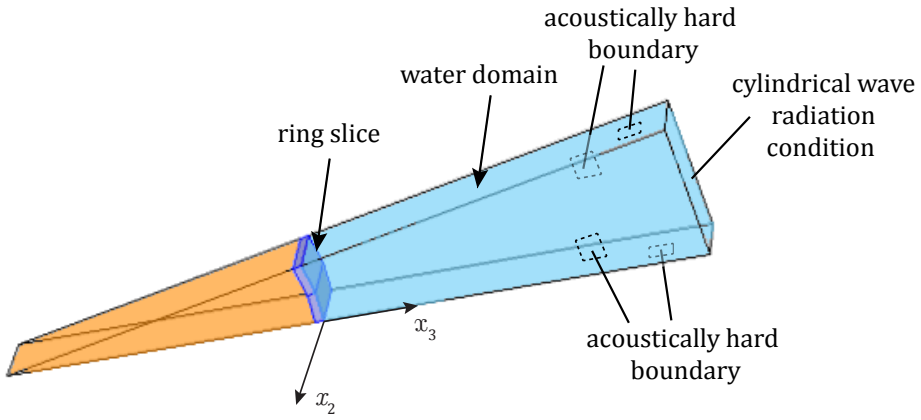

Figure D.2: Reduced ring model with water domains.

the (mechanical) radiation impedance of the cylinder, in this case one of infinite height. See Chapter 3 for a more detailed explanation of this model. Note that the boundary conditions imposed are equivalent to a cylinder of infinite height only as far as the radiation impedance is concerned. When calculating values for other lumped parameters, the finite height h of the modeled cylinder is used.

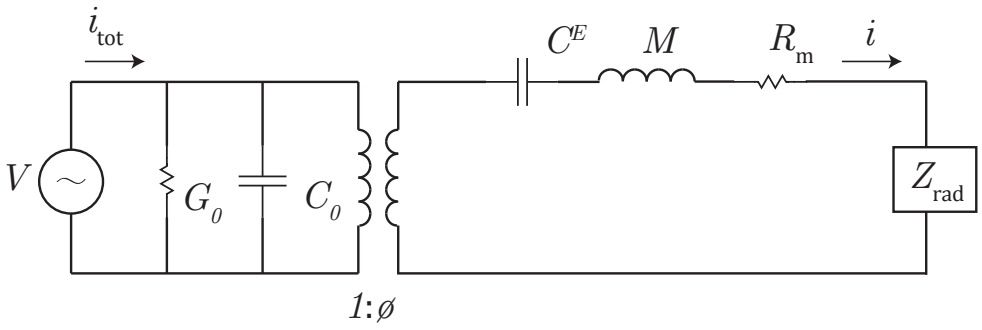

Figure D.3: Lumped element circuit model for transducer ring.

To simplify the circuit, G_0 and C_0 may be combined as $Z_{1,\mathrm{e}}$, where the subscript "e" denotes an electrical impedance. Likewise, C^E, M, and R_{m} may be combined as Z_2. The simplified circuit is shown in Fig. D.4 Further, the

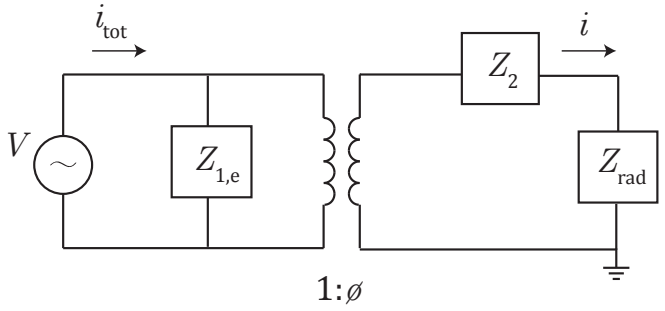

Figure D.4: Lumped parameter circuit model for cylindrical transducer ring with block impedances.

mechanical impedances Z_2 and Z_{rad} can be brought across the transformer with electromechanical turns ratio ϕ so that they may be written as electrical impedances $Z_{2,\mathrm{e}} = Z_2/\phi^2$ and $Z_{\mathrm{rad,e}} = Z_{\mathrm{rad}}/\phi^2$, as shown in Fig. D.5.

For a time-harmonic applied voltage V with angular frequency ω, the radiation impedance Z_{rad} for an infinite cylinder is given analytically by [12]

$$Z_{\mathrm{rad}} = \frac{2\pi a h}{\phi^2}\left(j\rho_0 c_0 \frac{H_0^{(2)}(ka)}{H_0^{(2)}(ka)}\right), \tag{D.1}$$

where $k = \omega/c$ is the wave number and ρ_0 and c_0 are the density and sound speed of water.

$Z_{2,\mathrm{e}}$ is the electrical impedance due to the mechanical properties of the ring itself and is thus the same regardless of the boundary conditions imposed

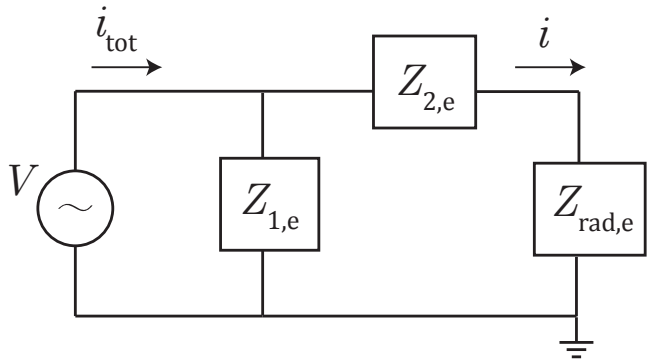

Figure D.5: Lumped parameter circuit model for cylindrical transducer ring with all elements in electrical domain.

on the water domain. It may be found with the current i that represents the radial velocity v of the ring in the mechanical domain and runs through $Z_{2,\text{e}}$ and $Z_{\text{rad,e}}$. The radial velocity v can be found from the finite element model and related to i through the turns ratio as $i = \phi v$. Using Ohm's law on the second branch of the circuit in Fig. D.5 yields $V = i\,(Z_{2,\text{e}} + Z_{\text{rad,e}})$, or

$$Z_{2,\text{e}} = V/i - Z_{\text{rad,e}}. \tag{D.2}$$

Likewise, $Z_{1,\text{e}}$ can be found with the current i_{tot} that is drawn on the electrodes of the transducer and can be measured in the finite element model. The total electrical impedance of the equivalent circuit shown in Fig. D.5 can be found through i_{tot} with the relation

$$Z_{\text{tot,e}} = \frac{V}{i_{\text{tot}}}. \tag{D.3}$$

Likewise, the total electrical admittance is given by

$$Y_{\text{tot,e}} = \frac{i_{\text{tot}}}{V}. \tag{D.4}$$

Additionally, $Z_{\text{tot,e}}$ can be found by combining $Z_{1,\text{e}}$ in parallel with the series sum of $Z_{1,\text{e}}$ and $Z_{rad,\text{e}}$:

$$Z_{\text{tot,e}} = \frac{Z_{1,\text{e}}\left(Z_{2,\text{e}} + Z_{\text{rad,e}}\right)}{Z_{1,\text{e}} + Z_{2,\text{e}} + Z_{\text{rad,e}}}. \tag{D.5}$$

Rearranging Eq. (D.5) gives an expression for $Z_{1,\text{e}}$ in terms of known quantities:

$$Z_{1,\text{e}} = -\frac{Z_{\text{tot,e}}\left(Z_{2,\text{e}} + Z_{\text{rad,e}}\right)}{Z_{\text{tot,e}} - \left(Z_{2,\text{e}} + Z_{\text{rad,e}}\right)}. \tag{D.6}$$

The equivalent circuit for a transducer ring subject to finite cylinder radiation loading is shown in Fig. D.6, where a prime ($'$) is used to distinguish quantities that have differ from the infinite cylinder case. As discussed in Section 3.3.2.2, the radiation impedance for a finite cylinder is given by

$$Z'_{\text{rad}} = \sum_{n=0}^{\infty} j\pi a H^2 \rho_0 \omega \delta_n \sum_{m=0}^{\infty} \epsilon_m \,\text{Sinc}^2\left(\frac{\alpha_m H}{2}\right) \frac{H_n(\beta_m a)}{\beta_m d H'_n(\beta_m a)} \tag{D.7}$$

where

$$\delta_n = \begin{cases} 2, & \text{if } n = 0; \\ 1, & \text{otherwise.}, \end{cases} \tag{D.8}$$

$$\epsilon_m = \begin{cases} 1, & \text{if } m = 0; \\ 2, & \text{otherwise.}, \end{cases} \tag{D.9}$$

H_n is the Hankel function of order n, $\alpha_m = m2\pi/d$, $\beta_m = k^2 - \alpha_m^2$, and d is a replication distance (taken to be as large as computationally possible) used for a Fourier series solution. The electrical impedance due to this radiation

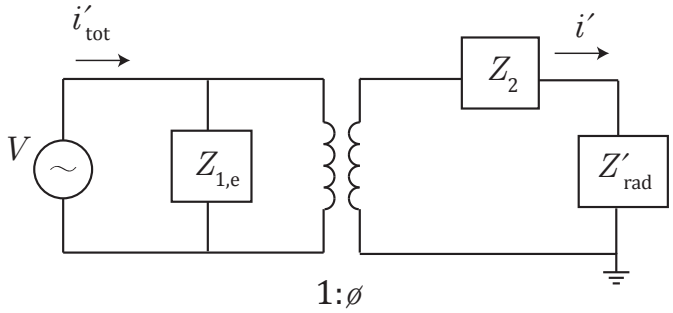

Figure D.6: Lumped parameter circuit model for cylindrical transducer ring subject to $Z'_{\mathrm{rad,e}}$, the (electrical) radiation impedance for a cylinder of finite height.

loading is then given by $Z'_{\mathrm{rad,e}} = Z'_{\mathrm{rad}}/\phi^2$. A MATLAB script used to determine Z'_{rad} is given in Section E. A comparison of the (mechanical) impedances due to radiation loading of a finite and infinite cylinder transducer in water, as given by Eqs. (D.7) and (D.1) respectively, is shown in Fig. D.7. Note that for low frequencies, the magnitude of the impedance for the infinite cylinder case is much higher than that of the finite cylinder, and that the impedance of the finite cylinder case approaches that of the infinite cylinder case as the frequency increases.

The total electrical impedance of the finite cylinder equivalent circuit is given by

$$Z'_{\mathrm{tot,e}} = \frac{Z_{1,\mathrm{e}}\left(Z_{2,\mathrm{e}} + Z'_{\mathrm{rad,e}}\right)}{Z_{1,\mathrm{e}} + Z_{2,\mathrm{e}} + Z'_{\mathrm{rad,e}}}, \tag{D.10}$$

and the total electrical admittance is given by

$$Y'_{\mathrm{tot,e}} = \frac{1}{Y'_{\mathrm{tot,e}}}. \tag{D.11}$$

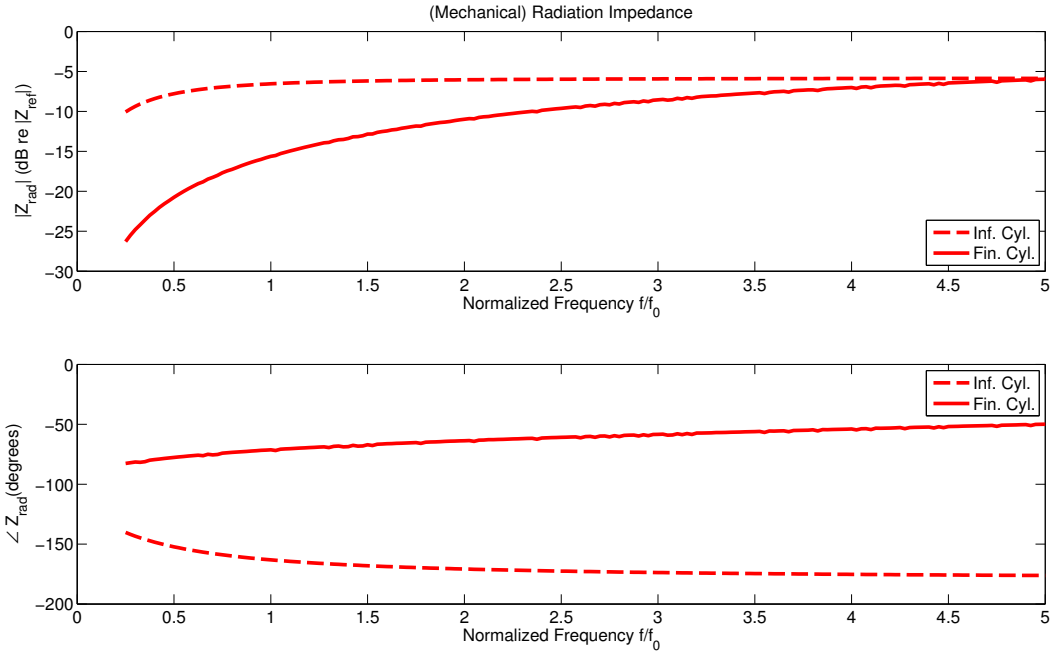

Figure D.7: Comparison of the (normalized) impedances due to radiation loading of a finite and infinite cylinder transducer in water.

Ohm's law gives the currents i' and i'_{tot} as

$$i' = \frac{V}{Z_{2,\text{e}} + Z'_{\text{rad,e}}} \tag{D.12}$$

and

$$i'_{\text{tot}} = \frac{V}{Z'_{\text{tot,e}}}. \tag{D.13}$$

This current i' can be converted to a velocity v' using $v' = \phi i'$ and used to calculate the transmit voltage response (TVR) for the cylinder ring of finite height using

$$\text{TVR (dB re 1 } \mu\text{Pa/V at 1 m)} = 20 \log_{10} \left(\frac{j\omega\rho_0 a h v'}{2V M_{\text{ref}}} \right), \tag{D.14}$$

where the reference sensitivity M_{ref} is given by $M_{\text{ref}} = 1\mu\text{Pa} \cdot \text{m/V}$.

The input admittance, average radial velocity, and transmit voltage response for a transducer with radiation impedance given by the finite and infinite cylinder case, using material properties values given by Appendix A, are compared in Figs. D.8, D.9, and D.10. The results for infinite cylinder case are taken directly from a finite element COMSOL model, which are then used to produce the results of the finite cylinder case as described above. For each metric, it can be seen that the response of the transducer around the primary resonance appears less damped and at a higher frequency than in the finite cylinder case. The bending resonance, occurring around $f/f_0 = 4$, is less affected by difference between the finite and infinite cylinder cases because the magnitude of their respective radiation impedances converge at higher frequencies, as seen in Fig. D.7.

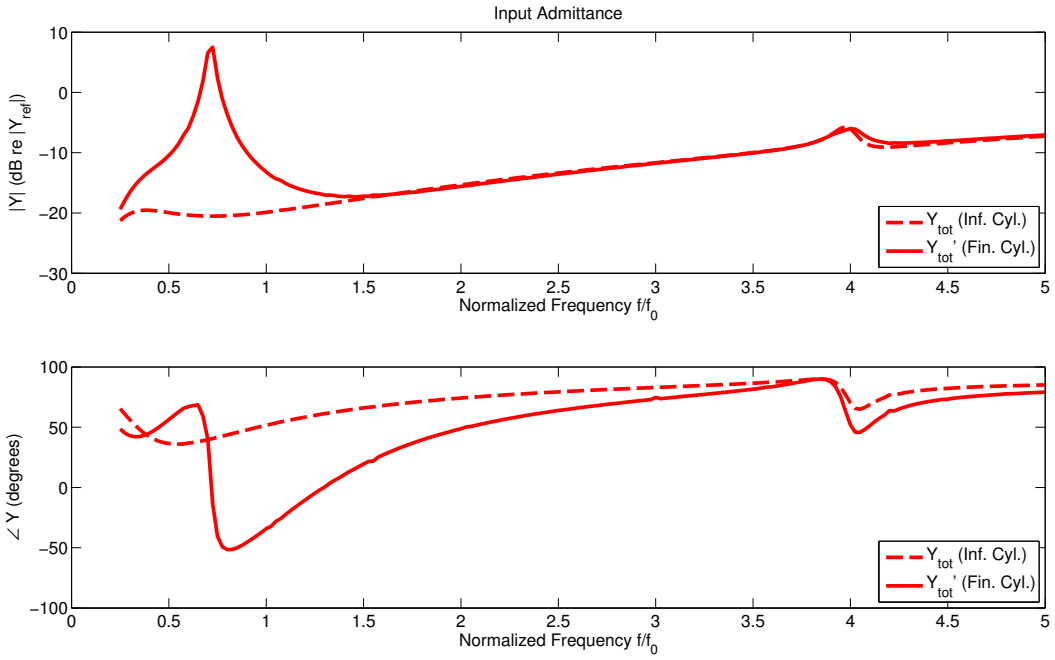

Figure D.8: Input admittance of the transducer with radiation impedance given by the finite and infinite cylinder case.

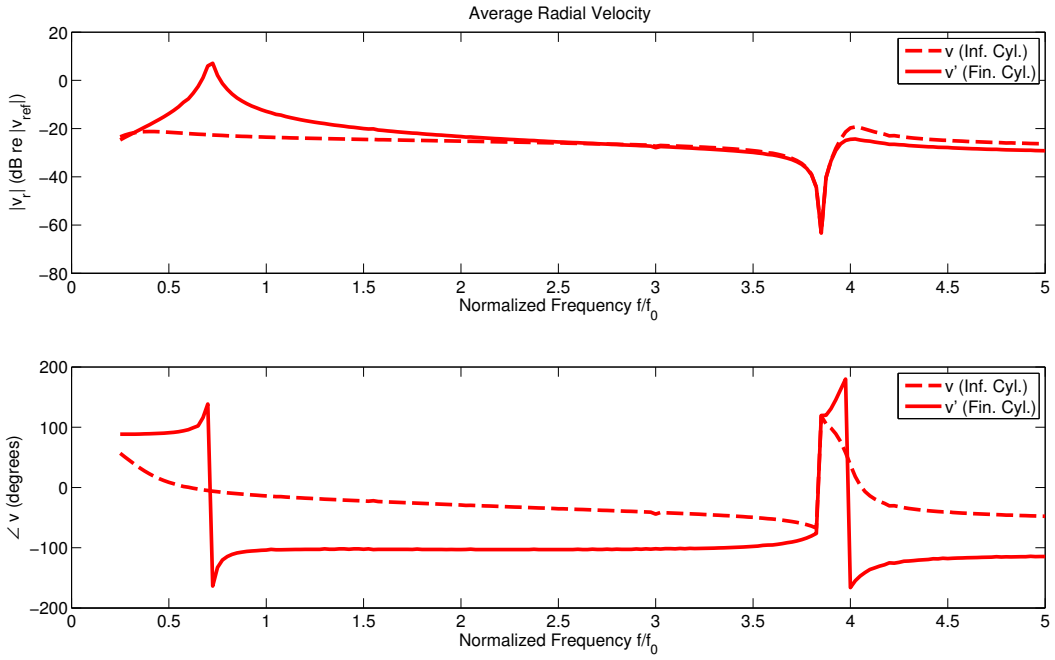

Figure D.9: Average radial velocity of the transducer with radiation impedance given by the finite and infinite cylinder case.

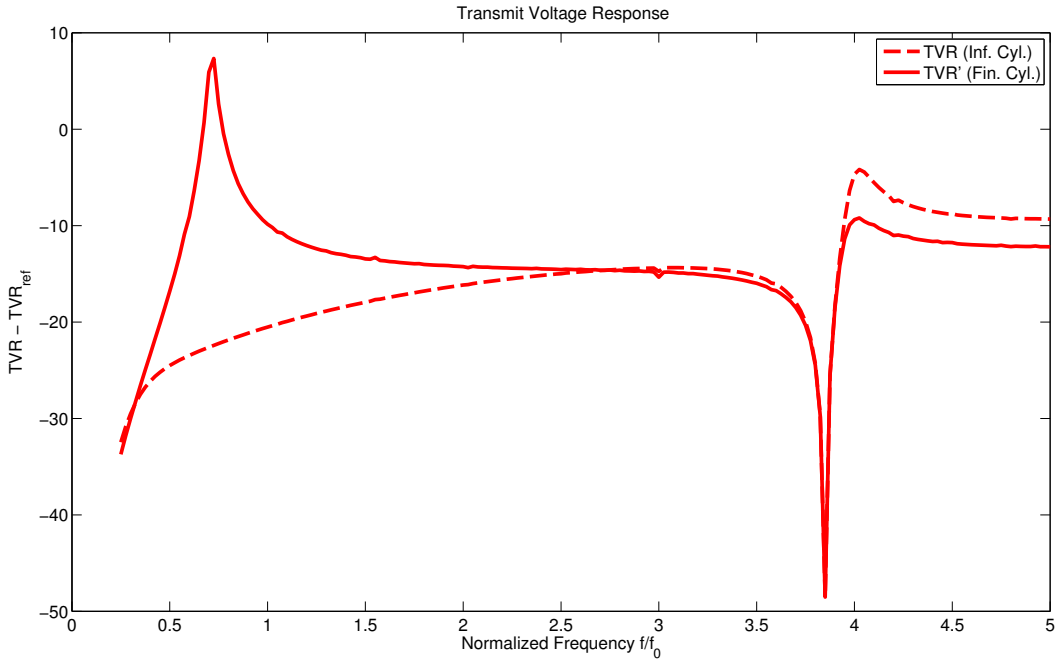

Figure D.10: Transmit voltage response of the transducer with radiation impedance given by the finite and infinite cylinder case.

Appendix E

MATLAB Code for Modeling the Radiation Impedance of a Finite Cylinder

The following is the MATLAB code used in this thesis to produce the radiation impedance of a finite cylinder, as given by Bulter. [14]

```
% This file calculates the radiation impedance for a
% finite cylinder mounted on a rigid cylinder.  It uses the
% relations given in Butler and Butler, JASA, 104(5), 1998.
%
% a ~ Radius of cylinder, [m]
% h ~ Height of cylinder, [m]
% d ~ Replication period, [m]
% n ~ Mode for rad impedance calc, []
% m ~ Number of terms in summation, []
% k ~ Wavenumer (or wavenumber range) in surrounding medium, [1/m]
% c ~ Speed of sound in fluid, [m/s]
% rho ~ Density of surrounding fluid, [kg/m^3]

function [Z]=Zrad_Cyl(a,h,d,n,m_max,k,rho,c) % ,HnPr_sum

% oooooooooooooooooooooooooooooooooooooooooooooooooooo
% Use loop for Fourier summation
% oooooooooooooooooooooooooooooooooooooooooooooooooooo

% ka=k*a;
w=k*c;                  % Radial frequency, [rad/s]
lam=2*pi./k;            % Wavelength, [m]
blk=ones(size(k));

% Set delta_n based on mode ------------------------
if n==0
```

```
    delta_n=2;
else
    delta_n=1;
end

% Evaluate for all k's for each Fourier component
S=zeros(size(k));           % zero the summation
for m_ind=1:m_max
    m=m_ind-1;
    if m==0
        eps_m=1;
    else
        eps_m=2;
    end
    M=d./lam;       % Replication distance in wavelengths
    m_ratio=m./M;
    Ar=blk-m_ratio.^2;

    % Replace zeros in Ar as they turn to poles in eval
    for J=1:length(k)
        if Ar(J)==0
            Ar(J)=eps;
        else
        end
    end

    beta_m=k.*sqrt(Ar);
    ba=beta_m*a;
    bd=beta_m*d;
    alpha_m=2*pi*m/d;
    ah=alpha_m*h;

    Hn=besselh(n,ba+eps);
    HnPr=0.5*(besselh(n-1,ba+eps)-besselh(n+1,ba+eps));
    A=(sinc(ah/(2*pi)))^2;
    S=eps_m*A*Hn./(bd.*HnPr)+S;
end

Z=i*pi*a*rho*delta_n*(h^2)*w.*S;
```

Bibliography

[1] A. Love, *Mathematical Theory of Elasticity* (Dover Publications, Mineola, NY) (1944).

[2] J. Haskins and J. Walsh, "Vibrations of ferroelectric cylindrical shells with transverse isotropy", The Journal of the Acoustical Society of America **29**, 729–734 (1956).

[3] D. C. D. Berlincourt and H. Jaffe, *Physical Acoustics, Vol. 1, Part A* (Academic Press, Inc., New York, NY) (1964).

[4] L. Camp, *Underwater Acoustics* (John Wiley & Sons, Inc., Hoboken, New Jersey) (1970).

[5] J. Butler, "Model for a ring transducer with inactive elements", The Journal of the Acoustical Society of America **59**, 480–482 (1976).

[6] O. B. Wilson, *Introduction to the Theory and Design of Sonar Transducers* (Peninsula Pub, Los Altos Hills, CA) (1989).

[7] C. Sherman and J. Butler, *Transducers and Arrays for Underwater Sound* (Springer Science+Business Media, LLC, New York, NY) (2007).

[8] A. International, *Piezoelectric Ceramics: Principles and Applications* (APC International, Ltd., Mackeyville, PA) (2002).

[9] S. Zhang and F. Li, "High performance ferroelectric relaxor-PbTiO3 single crystals: Status and perspective", Journal of Applied Physics **111**, 031301 (2012).

[10] L. Kinsler and A. Frey, *Fundamentals of Acoustics* (John Wiley & Sons, Inc., New York, NY) (2000).

[11] D. Stansfield, *Underwater Electroacoustic Transducers* (Peninsula Publishing, Los Altos Hills, CA) (1991).

[12] D. T. Blackstock, *Fundamentals of Physical Acoustics* (John Wiley & Sons, Inc., New York, NY) (2000).

[13] L. Beranek, *Acoustical Measurements* (American Institute of Physics, Cambridge, MA) (1988).

[14] J. Butler and A. Butler, "A Fourier series solution for the radiation impedance of a finite cylinder", The Journal of the Acoustical Society of America **104**, 2773–2778 (1998).

[15] M. Leach, *Introduction to Electroacoustics and Audio Amplifier Design* (Kendall Hunt, Dubuque, IA) (1998).

[16] L. Meirovitch, *Elements of Vibration Analysis* (McGraw-Hill, Inc., New York, NY) (1975).

[17] L. Beranek, *Acoustics* (American Institute of Physics, Cambridge, MA) (1954).

[18] D. M. D. Karnopp and R. Rosenberg, *System Dynamics: Modeling and Simulation of Mechatronic Systems* (John Wiley & Sons, Inc., Hoboken, NJ) (2006).

[19] C. R. P. Mott and R. Corsaro, "Acoustic and dynamic mechanical properties of a polyurethane rubber", The Journal of the Acoustical Society of America **111**, 1782–90 (2002).